High-Resolution Crystal Plasticity Simulations

Von der Fakultät für Georessourcen und Materialtechnik der
Rheinisch–Westfälischen Technischen Hochschule Aachen

zur Erlangung des akademischen Grades eines

Doktors der Ingenieurswissenschaften

genehmigte Dissertation

vorgelegt von

Dipl.-Ing. Martin Diehl

aus Siegen

Berichter: Prof. Dr.-Ing. Dierk Raabe
PD Dr. rer. nat. Franz Roters
Univ.-Prof. Dr. rer. nat. Robert Svendsen
Dr. Ricardo A. Lebensohn

Tag der mündlichen Prüfung: 22. Juni 2015

Bibliografische Information der Deutschen Nationalbibliothek
Die Deutsche Nationalbibliothek verzeichnet diese Publikation in der Deutschen Nationalbibliografie; detaillierte bibliografische Daten sind im Internet über http://dnb.ddb.de abrufbar.

Martin Diehl:

High-Resolution Crystal Plasticity Simulations

1. Auflage, 2016

Gedruckt auf holz- und säurefreiem Papier, 100% chlorfrei gebleicht.

Apprimus Verlag, Aachen, 2016
Wissenschaftsverlag des Instituts für Industriekommunikation und Fachmedien an der RWTH Aachen
Steinbachstr. 25, 52074 Aachen
Internet: www.apprimus-verlag.de, E-Mail: info@apprimus-verlag.de

Printed in Germany

ISBN 978-3-86359-392-6

D 82 (Diss. RWTH Aachen University, 2015)

Acknowledgements

This doctoral thesis was written during my stay at the department for Mikrostrukturphysik und Legierungsdesign of the Max-Planck-Institut für Eisenforschung GmbH (MPIE) under the supervision of Dierk Raabe. It would not have been possible to carry out my work without the academic and technical support of the MPIE staff and I want to thank all colleagues for the nice working atmosphere and the interesting scientific discussions.

Especially, I would like to thank Franz Roters for answering my various questions concerning all aspects of the constitutive modelling and the underlying physics. Conducting the simulations and writing this thesis would not have been possible without his support. I am also grateful for his comments and suggestions regarding the phrasing and for picking up a large amount of spelling errors.

I would like to express my special appreciation to Philip Eisenlohr. Many hours of fruitful discussions on scientific and technical questions and his hints in programming were an invaluable help regarding all aspects of the work.

Conduction the simulations using the improved spectral method would not have been possible without Pratheek Shanthraj. In addition to his help regarding the numerical challenges of his work, I also acknowledge his support in improving the technical aspects of the Düsseldorf advanced material simulation kit (DAMASK) and the discussions on modelling related questions.

For scientific and technical support I have to thank Piet Kok, Yuguo An, and Henk Vegter from Tata Steel RD&T in IJmuiden. I also gratefully acknowledge the financial sponsorship of Tata Steel Europe via the Materials Innovation Institute (M2i).

The experimental results presented in this thesis have been performed in collaboration with C. Cem Taşan, Dingshun Yan, Claudio Zambaldi, Steffi Sandlöbes, and Heidi Bögershausen. I'm grateful for the patient work in obtaining the experimental results needed for the comparison of experimental and theoretical work. The intense discussion on how to design coupled experiments and simulations and interpret their results enabled me to present a variety of results in this thesis.

I've also benefited from many fruitful discussions with Dierk Raabe, who was so kind to host me as main examiner in the Mikrostrukturphysik und Legierungs-

DESIGN department of the MPIE. I would like to thank him for these discussions and for encouraging me in doing my research and writing this thesis.

Finally, I'd like to thank my examiners DIERK RAABE, FRANZ ROTERS, BOB SVENDSEN, and RICARDO A. LEBENSOHN for reading and evaluating my thesis and examine me. Special thanks go to CHRISTINA SCHEU for hosting the defence here in Düsseldorf.

For any errors or inadequacies that may remain in this work, of course, the responsibility is entirely my own.

This research was carried out under project number M41.2.10410 in the framework of the Research Program of the Materials Innovation Institute (M2i) in the Netherlands (www.m2i.nl).

Contents

1 Introduction

In recent years, microstructures of advanced materials have become increasingly complex, incorporating typically more than one microstructural feature to adjust the material properties according to specific needs. This holds especially in the case when more than one phase is present. Usually, multiple phases are introduced to improve strength and ductility at the same time like, *e.g.*, in dual phase (DP) steels (Tasan et al., 2015). To simulate the behaviour of such complex materials, the underlying effects such as interaction of different phases, hardening of slip systems, twinning etc. have to be considered in order to produce applicable results.

In this context, crystal plasticity (CP) simulations have proven to be a powerful tool to determine the local and global mechanical response of metallic microstructures (Cailletaud et al., 2003; Roters et al., 2010a,b, 2013). Hence, a lot of effort has been spent in recent years on improving this technique by developing more accurate, physics based constitutive laws on the single grain level. However, these improvements made a major drawback of CP modelling even more visible: the high computational costs associated with these calculations.

The computation time needed to solve a CP problem on the continuum level can be categorised into

- the evaluation of the selected constitutive law, and
- the solution of the associated mechanical boundary value problem (BVP).

More complex material models increase the computational cost of the constitutive evaluation significantly, hence there is always a trade-off between simulation quality and computation time in the design of a material point model. However, using an improved BVP solver can reduce computation costs without sacrificing accuracy.

In this thesis, the capabilities of high-resolution CP simulations are presented and discussed. To enable the simulation of highly resolved microstructures, both above mentioned contributions to the runtime have to be kept small. This is done by (i) using rather simple—and therefore fast—constitutive models, and by (ii) using an effective spectral method employing fast Fourier transforms (FFTs) for solving the partial differential equations (PDEs) describing the mechanical behaviour. This alternative to the typically used finite element method (FEM) (see *e.g.* Bathe, 2002) for solving the system of partial differential equations resulting from strain compatibility and static equilibrium has been introduced by Moulinec et al. (1994, 1998) in the context of material mechanics. While the spectral method based solvers show exponential convergence due to the use of trigonometric polynomials as ansatz functions, their application is limited to volume elements (VEs) with periodic boundary conditions

(BCs) for the same reason. More specifically, the volume under consideration is copied repeatedly, expanding it to an infinite body. This approach does not only allow the study of local quantities in the VE, but also—if the selected microstructure is representative for the material—prediction of the global homogenised material response.

In this thesis, it is shown how high-resolution CP simulations can help to improve the knowledge about several investigated material systems, ultimately aiming at the development of structural materials with enhanced properties. As outlined on various examples, full-field numerical simulations of representative volume elements (RVEs) with high resolution are required for this task, as the local microstructural features determine the activation of the concurrent deformation mechanisms in a non-trivial way.

This thesis is structured as following: First, the computational framework used is given in chapter 2 "*Modelling Framework*". This chapter is further subdivided into the introduction of a mathematical framework for describing a body under load (section 2.1 "*Continuum Mechanics*"), the presentation of the constitutive models (section 2.2 "*Crystal Plasticity*"), and the outline of the aforementioned spectral solver in section 2.3). Secondly, the performed simulations including the results are presented in chapter 3 "*Simulations*". The simulations are classified into two categories: Real microstructures and artificial microstructures, presented in section 3.1 "*Real Microstructures*" and section 3.2 "*Artificial Microstructures*", respectively. Finally, in chapter 4 "*Summary and Outlook*" a summary and the conclusions drawn from the presented work are given.

2 Modelling Framework

The simulations presented in this work were performed using the Düsseldorf advanced material simulation kit (DAMASK) by Roters (2011) and Roters et al. (2012). DAMASK is a software package that provides various constitutive models and homogenisation schemes for crystal plasticity (CP) simulations at different length scales. DAMASK is open source software, developed here at the Max-Planck-Institut für Eisenforschung GmbH (MPIE). It provides a flexible interface that allows employing easily various solvers for the mechanical boundary value problem (BVP). Currently, the commercial finite element method (FEM) solvers Abaqus (via the user subroutines Umat/Vumat) and MSC.Marc (via the user subroutine Hypela2) as well as an integrated spectral method based solver are supported. In order to allow high-resolution simulations, several parts of DAMASK have been optimised in the framework of this Ph.D. project to reduce memory consumption and computation time. The performance of DAMASK for a simple model geometry is shown in appendix B.

As usual, the CP models are formulated in a continuum mechanics framework to describe the mechanical behaviour of a body under consideration. In section 2.1 "*Continuum Mechanics*", a mathematical notation is introduced that allows modelling an arbitrary body under external loads. Equipped with this vocabulary, the constitutive models used in this work are introduced in section 2.2 "*Crystal Plasticity*". What follows is an outline of the solver used to find a physically legitimate solution of the modelled problem in section 2.3 "*Spectral Solver*".

2.1 Continuum Mechanics

In continuum mechanics, the macroscopic behaviour of a body is described using a hypothetical continuous medium. According to this assumption, any object completely fills the space it occupies. This allows describing the behaviour of the material with continuous mathematical functions.

In the context of continuum mechanics, the following set of equations has to be fulfilled for a legitimate solution:

1. compatibility of deformation
2. mechanical equilibrium
3. constitutive law

To enable a framework, in which these equations can be solved, in this section

first the different configurations of a body under load are shown in subsection 2.1.1 "*Configurations*". From the configurations, strain and stress measures are derived in subsection 2.1.2 "*Strain Measures*" and subsection 2.1.3 "*Stress Measures*", respectively. The condition for compatibility is related to the deformation and, hence, outlined in section 2.1.2. Similarly, the equilibrium condition is discussed in section 2.1.3. The details of the constitutive laws used are presented in section 2.2 "*Crystal Plasticity*". The fundamentals here are referring to Diehl (2010), most of the concepts can also be found in, *e.g.* McGinty (2015).

2.1.1 Configurations

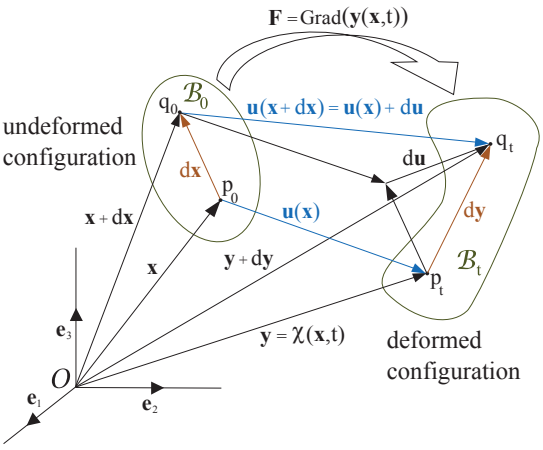

Figure 2.1: Continuum body shown in the undeformed and a deformed configuration.

Let $\mathcal{B}$ be a body that is assumed to be a composition of an infinite number of material points. In the time-independent undeformed or reference configuration it occupies the region $\mathcal{B}_0$. In the time-dependent deformed or current configuration, the region $\mathcal{B}_t$ is filled by $\mathcal{B}$. The location of the material points in the undeformed state is given by the vectors $\boldsymbol{x}, \boldsymbol{x} \in \mathcal{B}_0$ and in a deformed state by the vectors $\boldsymbol{y}, \boldsymbol{y} \in \mathcal{B}_t$. This situation is illustrated for an example configuration in fig. 2.1. In general, for each configuration a different basis with corresponding unit vectors exists. However, in this work, the same CARTESIAN coordinate system is used in both configurations which allows skipping the explicit notation of their unit vectors.

Any deformation of the body can be described in both, the reference and the current configuration. In the material or LAGRANGIAN description, each particle belongs to its current spatial location. In EULERIAN or spatial description, the location belongs to the particle. In other words, the LAGRANGIAN description is based on the question "At which location is the particle?", while the EULERIAN description answers the question "Which particle is at the location?". This work—as common for solid mechanics—uses a LAGRANGIAN description. Hence, a deformation map $\boldsymbol{\chi}(\boldsymbol{x}) : \boldsymbol{x} \in \mathcal{B}_0 \rightarrow \boldsymbol{y} \in \mathcal{B}_t$ is introduced that maps points $\boldsymbol{x}$ in the reference configuration to points $\boldsymbol{y}$ in the current configuration.

The displacement $\boldsymbol{u}$ of a material point is the difference vector from a point in reference configuration $\mathcal{B}_0$ to the deformed configuration $\mathcal{B}_t$:

$$\boldsymbol{u}(\boldsymbol{x},t) = \boldsymbol{\chi}(\boldsymbol{x},t) - \boldsymbol{x} \tag{2.1}$$

with $\boldsymbol{u}$ being a continuous function. Focussing at a given time, *i.e.* a fixed deformation state, allows simplifying the notation to $\boldsymbol{u}(\boldsymbol{x}) = \boldsymbol{\chi}(\boldsymbol{x}) - \boldsymbol{x}$ which is also used in fig. 2.1.

A line segment $\mathrm{d}\,\boldsymbol{x}$ in an infinitesimal neighbourhood of a material point $\boldsymbol{x}$ in the reference configuration (see fig. 2.1) is pushed forward into the current configuration by:

$$\boldsymbol{y} + \mathrm{d}\,\boldsymbol{y} = \boldsymbol{y} + \frac{\partial \boldsymbol{y}}{\partial \boldsymbol{x}} \cdot \mathrm{d}\,\boldsymbol{x} + \mathcal{O}(\mathrm{d}\,\boldsymbol{x}^2) \tag{2.2}$$

Neglecting terms of higher order, $\mathrm{d}\,\boldsymbol{y}$ can be expressed as:

$$\begin{aligned} \mathrm{d}\,\boldsymbol{y} &= \frac{\partial \boldsymbol{y}}{\partial \boldsymbol{x}} \cdot \mathrm{d}\,\boldsymbol{x} \\ &= \frac{\partial \boldsymbol{\chi}(\boldsymbol{x})}{\partial \boldsymbol{x}} \cdot \mathrm{d}\,\boldsymbol{x} \\ &= \nabla \boldsymbol{\chi} \cdot \mathrm{d}\,\boldsymbol{x} \\ &= \underbrace{\mathrm{Grad}\,\boldsymbol{\chi}}_{=:\boldsymbol{F}(\boldsymbol{x})} \cdot \mathrm{d}\,\boldsymbol{x}, \end{aligned} \tag{2.3}$$

where $\boldsymbol{F}(\boldsymbol{x})$ is a 2nd order tensor called the deformation gradient and $\boldsymbol{\nabla}$ is the "del" operator (Schey, 1973). To simplify the notation, in the following, the argument $\boldsymbol{x}$ is dropped whenever it is possible, *i.e.* $\boldsymbol{F}(\boldsymbol{x})$ is denoted as $\boldsymbol{F}$ only. The deformation gradient maps the vector $\mathrm{d}\,\boldsymbol{x}$ at $\boldsymbol{x}$ in the reference configuration to the vector $\mathrm{d}\,\boldsymbol{y}$ at $\boldsymbol{y}$ in the current configuration. The deformation tensor has one basis in the reference configuration and one in the current configuration, it is therefore called a 2-point tensor. The inverse of the deformation gradient, $\boldsymbol{F}^{-1}$, maps an element from the current to the reference configuration. It is sometimes called the spatial deformation gradient in contrast to the the material deformation gradient $\boldsymbol{F}$. The spatial line segment $\mathrm{d}\,\boldsymbol{y}$ is called the "push forward" of the material line segment $\mathrm{d}\,\boldsymbol{x}$, which in turn can be called the "pull back" (performed by $\boldsymbol{F}^{-1}$) of $\mathrm{d}\,\boldsymbol{y}$.

For a moving body, the position of the material points varies with time. The material velocity field is defined as:

$$\begin{aligned} \boldsymbol{v} &= \frac{\mathrm{d}\,\boldsymbol{u}(\boldsymbol{x})}{\mathrm{d}\,t} \\ &= \dot{\boldsymbol{u}} \\ &= \dot{\boldsymbol{\chi}}. \end{aligned} \tag{2.4}$$

$\dot{\boldsymbol{u}} = \dot{\boldsymbol{\chi}}$ holds because the points in the reference configuration do not change their position, *i.e.* $\mathrm{d}\,\boldsymbol{x}/\,\mathrm{d}\,t = \boldsymbol{0}$. The spatial gradient of the velocity field is:

$$\boldsymbol{L} = \frac{\partial \boldsymbol{v}}{\partial \boldsymbol{y}}, \tag{2.5}$$

where $\boldsymbol{L}$ is called the velocity gradient. Using the chain rule, it can be expressed as

$$\boldsymbol{L} = \dot{\boldsymbol{F}} \cdot \boldsymbol{F}^{-1}. \tag{2.6}$$

Because the velocity gradient is an EULERIAN quantity (McGinty, 2015), the loading of a body with a constant velocity gradient will result in the same rate of deformation independently of the shape in the current configuration. Equation (2.6) allows expressing it conveniently as 2-point quantities.

2.1.2 Strain Measures

In the general case, $\boldsymbol{F}$ contains a rotation and a stretch. Being an invertible tensor, a unique decomposition called "polar decomposition" exists for $\boldsymbol{F}$:

$$\begin{aligned} \boldsymbol{F} &= \boldsymbol{V} \cdot \boldsymbol{R} \\ &= \quad \boldsymbol{R} \cdot \boldsymbol{U}, \end{aligned} \tag{2.7}$$

where $\boldsymbol{R}$ is the rotation tensor, $\boldsymbol{V}$ is called the left stretch tensor and $\boldsymbol{U}$ the right stretch tensor. $\boldsymbol{F}$, $\boldsymbol{U}$, and $\boldsymbol{V}$ have the same determinant, called the JACOBIAN (J):

$$J = \det(\boldsymbol{F}) = \det(\boldsymbol{U}) = \det(\boldsymbol{V}). \tag{2.8}$$

A pure rotation does not change the shape of the body and should therefore result in zero strain. Hence, any strain measure should depend on $\boldsymbol{V}$ or $\boldsymbol{U}$ only. In other words, any strain measure is valid that quantifies a distance between a given deformation gradient and its rotational part.

Inserting eq. (2.1) into eq. (2.3) allows expressing the deformation gradient as:

$$\begin{aligned} \boldsymbol{F} &= \frac{\partial(\boldsymbol{x} + \boldsymbol{u})}{\partial \boldsymbol{x}} \\ &= \boldsymbol{I} + \frac{\partial \boldsymbol{u}}{\partial \boldsymbol{x}}. \end{aligned} \tag{2.9}$$

$\boldsymbol{H}_0 := \frac{\partial \boldsymbol{u}}{\partial \boldsymbol{x}}$ is called the displacement gradient. The tensor $\boldsymbol{I}$ is the identity tensor, also called the unit matrix.

Displacement and deformation gradient are means of describing the deformation of a body. In the same way as $\boldsymbol{F}$ is called the material deformation gradient, $\boldsymbol{H}_0$ is called the material displacement gradient. The spatial displacement gradient is defined as $\boldsymbol{I} - \boldsymbol{F}^{-1}$ and denoted here as as $\boldsymbol{H}_\mathrm{t}$.

Deformation gradient, displacement gradient and their respective inverses are 2-point tensors. However, the deformation can be expressed in the reference configuration only

as:

$$\begin{aligned} \mathrm{d}\,\boldsymbol{y} \cdot \mathrm{d}\,\boldsymbol{y} &= (\boldsymbol{F} \cdot \mathrm{d}\,\boldsymbol{x}) \cdot (\boldsymbol{F} \cdot \mathrm{d}\,\boldsymbol{x}) \\ &= \mathrm{d}\,\boldsymbol{x} \cdot \underbrace{(\boldsymbol{F}^T \cdot \boldsymbol{F})}_{=:\boldsymbol{C}} \cdot \mathrm{d}\,\boldsymbol{x}. \end{aligned} \tag{2.10}$$

$\boldsymbol{C} = \boldsymbol{U}^2$ is called the right Cauchy–Green deformation tensor. It is a symmetric tensor completely in the material configuration.

The change of length (*i.e.* a strain) can be written as:

$$\begin{aligned} \mathrm{d}\,\boldsymbol{y} \cdot \mathrm{d}\,\boldsymbol{y} - \mathrm{d}\,\boldsymbol{x} \cdot \mathrm{d}\,\boldsymbol{x} &= \mathrm{d}\,\boldsymbol{x} \cdot \boldsymbol{C} \cdot \mathrm{d}\,\boldsymbol{x} - \mathrm{d}\,\boldsymbol{x} \cdot \mathrm{d}\,\boldsymbol{x} \\ &= \mathrm{d}\,\boldsymbol{x} \cdot \underbrace{(\boldsymbol{C} - \boldsymbol{I})}_{=:\boldsymbol{E}_0 \cdot 2} \cdot \mathrm{d}\,\boldsymbol{x}. \end{aligned} \tag{2.11}$$

$\boldsymbol{E}_0 := \frac{1}{2}(\boldsymbol{C} - \boldsymbol{I}) = \frac{1}{2}(\boldsymbol{F}^T \cdot \boldsymbol{F} - \boldsymbol{I})$ is called the Green–Lagrange strain tensor. It depends only on the right Cauchy–Green deformation tensor and is, therefore, a valid strain measure written in the reference configuration.

A similar transformation as in eq. (2.10) can express the deformation in the current configuration:

$$\begin{aligned} \mathrm{d}\,\boldsymbol{x} \cdot \mathrm{d}\,\boldsymbol{x} &= (\boldsymbol{F}^{-1} \cdot \mathrm{d}\,\boldsymbol{y}) \cdot (\boldsymbol{F}^{-1} \cdot \mathrm{d}\,\boldsymbol{y}) \\ &= \mathrm{d}\,\boldsymbol{y} \cdot \underbrace{(\boldsymbol{F}^{-T} \cdot \boldsymbol{F}^{-1})}_{=:\boldsymbol{B}^{-1}} \cdot \mathrm{d}\,\boldsymbol{y}. \end{aligned} \tag{2.12}$$

$\boldsymbol{B}^{-1} := \boldsymbol{F}^{-T} \cdot \boldsymbol{F}^{-1}$ implies $\boldsymbol{B} = \boldsymbol{F} \cdot \boldsymbol{F}^T$. The tensor $\boldsymbol{B} = \boldsymbol{V}^2$ is called the left Cauchy–Green deformation tensor. It is a symmetric tensor completely in the current configuration.

The change of length under a deformation can be expressed as:

$$\begin{aligned} \mathrm{d}\,\boldsymbol{y} \cdot \mathrm{d}\,\boldsymbol{y} - \mathrm{d}\,\boldsymbol{x} \cdot \mathrm{d}\,\boldsymbol{x} &= \mathrm{d}\,\boldsymbol{y} \cdot \mathrm{d}\,\boldsymbol{y} - \mathrm{d}\,\boldsymbol{y} \cdot \boldsymbol{B}^{-1} \cdot \mathrm{d}\,\boldsymbol{y} \\ &= \mathrm{d}\,\boldsymbol{y} \cdot \underbrace{(\boldsymbol{I} - \boldsymbol{B}^{-1})}_{=:\boldsymbol{E}_t \cdot 2} \cdot \mathrm{d}\,\boldsymbol{y}. \end{aligned} \tag{2.13}$$

$\boldsymbol{E}_\mathrm{t} := \frac{1}{2}(\boldsymbol{I} - \boldsymbol{B}^{-1}) = \frac{1}{2}(\boldsymbol{I} - \boldsymbol{F}^{-T} \cdot \boldsymbol{F}^{-1})$ is called the Euler–Almansi strain tensor. As a function only of the left Cauchy–Green deformation tensor it is completely in the current configuration and a valid strain measure.

The push forward and pull back are also defined for the deformation measures. The push forward of the Green–Lagrange stretch tensor is the Euler–Almansi stretch tensor and, consequently, the pull back performs the inverse operation:

$$\boldsymbol{E}_\mathrm{t} = \boldsymbol{F}^{-T} \cdot \boldsymbol{E}_0 \cdot \boldsymbol{F}^{-1} \Leftrightarrow \boldsymbol{E}_0 = \boldsymbol{F}^T \cdot \boldsymbol{E}_\mathrm{t} \cdot \boldsymbol{F}. \tag{2.14}$$

For small strains, *i.e.* $\boldsymbol{y} - \boldsymbol{x} \approx \boldsymbol{0}$, the linearisation of the Euler–Almansi strain

tensor and the Green–Lagrange strain results in the same strain tensor. It is called the Cauchy strain tensor $\boldsymbol{\varepsilon}$:

$$\begin{aligned} \varepsilon_{ij} &= \frac{1}{2}(u_{i,j} + u_{j,i}) \\ &\approx E_{0,ij} \\ &\approx E_{\mathrm{t},ij}, \end{aligned} \tag{2.15}$$

when using index notation and Einstein convention. According to Einstein notation or Einstein summation, it is implicitly summed over an index variable that appears twice in a product. Hence, in vector notation it reads as:

$$\boldsymbol{\varepsilon} = \frac{1}{2}(\boldsymbol{\nabla u} + (\boldsymbol{\nabla u})^{\mathrm{T}}). \tag{2.16}$$

With $\boldsymbol{\omega} := \frac{1}{2}(\boldsymbol{\nabla u} - (\boldsymbol{\nabla u})^{\mathrm{T}})$ denoting the rotation tensor, the displacement gradient can be written in the infinitesimal strain framework as:

$$\boldsymbol{\nabla u} = \boldsymbol{\varepsilon} + \boldsymbol{\omega}. \tag{2.17}$$

It can be shown that this small strain formulation (infinitesimal strain formulation) is not rotation-invariant for large rotations, and, hence, is a valid approximation for small deformations only.

To ensure that gaps or overlaps do not develop within the continuum body, *i.e.* not to violate the basic assumption of a continuous medium, certain mathematical conditions have to be satisfied. A body that deforms without developing any gaps/overlaps is called a compatible body; hence a compatibility condition can be used to determine whether a particular deformation is permissible.

For infinitesimal strains, the displacements of a compatible body must be obtainable from integrating the strains. This is possible for

$$e_{ikr}\ e_{jls}\ \varepsilon_{ij,kl} = 0. \tag{2.18}$$

where e_{ijk} is the permutation symbol.

In the finite strain formulation, the strain field of a compatible body originates from a curl free deformation gradient field:

$$\begin{aligned} \mathbf{0} &= \operatorname{Curl} \boldsymbol{F} \\ &= \boldsymbol{\nabla} \times \boldsymbol{F}. \end{aligned} \tag{2.19}$$

Strain measures in one dimension

Strain measures are much simpler to compare in the one-dimensional case due to the absence of any rotations. In one dimension, any deformation can be

described by two parameters: The length in the current configuration l_t and the length in the reference configuration l_0. By defining the stretch ratio as $\lambda := l_\mathrm{t}/l_0$, the three presented strain measures and the limits for infinite tension and infinite compression read as:

Table 2.1: Definition of strain measures and behaviour for tension and compression.

strain measure	definition	compression	tension
Green–Lagrange	$\frac{1}{2}(\lambda^2 - 1)$	$\lim_{\lambda\to 0} = -\frac{1}{2}$	$\lim_{\lambda\to\infty} = \infty$
Euler–Almansi	$\frac{1}{2}(1 - \frac{1}{\lambda^2})$	$\lim_{\lambda\to 0} = -\infty$	$\lim_{\lambda\to\infty} = \frac{1}{2}$
Cauchy	$\lambda - 1$	$\lim_{\lambda\to 0} = -1$	$\lim_{\lambda\to\infty} = \infty$

From table 2.1 it can be seen that the measures are not symmetrical and reach different limits for infinite tension and infinite compression. A measure that overcomes these inconsistencies is the logarithmic strain $\boldsymbol{\varepsilon}_{log} := \ln(\lambda)$. Tension or compression applied at the same rate (see eq. (2.4) for the tensorial case) for a given time will result in a logarithmic strain which differs only in the algebraic sign.

Moreover, for both, the spatial and the material case, different strain measures with power α of λ can be derived based on the formula $1/\alpha(1 - \lambda^{-\alpha})$. For the material measures, the exponent α has a negative sign, for the spatial measures a positive one. From table 2.1 it can be seen that λ contributes with its second power to the Green–Lagrange and the Euler–Almansi strain. The strain measure of order 0 is the logarithmic strain.

2.1.3 Stress Measures

Stress is the force per area acting on the material. As introduced in section 2.1.1, for a general deformation state a distinction has to be made between the reference and the current configuration. This means that different stress measures exist, depending on the configuration in which force and area are defined.

In the current configuration, a force $\Delta\boldsymbol{r}_\mathrm{t}$ on an area Δa_t with normal vector $\boldsymbol{n}_\mathrm{t}$ results in:

$$\boldsymbol{t}_\mathrm{t}(\boldsymbol{n}_\mathrm{t}) = \lim_{\Delta a_\mathrm{t}\to 0} \frac{\Delta \boldsymbol{r}_\mathrm{t}}{\Delta a_\mathrm{t}} \tag{2.20}$$

where $\boldsymbol{t}_\mathrm{t}$ is called the vector of surface traction or Cauchy traction. The Cauchy stress tensor or "true stress tensor" $\boldsymbol{\sigma}$ is defined by

$$\boldsymbol{t}_\mathrm{t}(\boldsymbol{y},t,\boldsymbol{n}_\mathrm{t}) =: \boldsymbol{\sigma}(\boldsymbol{y},t) \cdot \boldsymbol{n}_\mathrm{t}, \tag{2.21}$$

as the solution that holds for all normal directions $\boldsymbol{t}$. The Cauchy stress is a 2^{nd}

order tensor in spatial coordinates.

Scaling the traction $\boldsymbol{t}_\mathrm{t}$ from to the current area Δa_t to the area in reference configuration Δa_0 results in the so-called pseudo traction vector $\boldsymbol{t}_{0,t}$. It is also called nominal or 1st Piola–Kirchhoff traction vector and is determined by looking at an infinitesimal force $\mathrm{d}\boldsymbol{r}_\mathrm{t}$:

$$\begin{aligned} \mathrm{d}\,\boldsymbol{r}_\mathrm{t} &= \boldsymbol{t}_\mathrm{t}\ \mathrm{d}\,a_\mathrm{t} \\ &= \boldsymbol{t}_{0,t}\ \mathrm{d}\,a_0. \end{aligned} \tag{2.22}$$

The vector notation of the areas in the reference and current configuration is $\mathrm{d}\,\boldsymbol{a}_\mathrm{t} = \boldsymbol{n}_\mathrm{t}\ \mathrm{d}\,a_\mathrm{t}$ and $\mathrm{d}\,\boldsymbol{a}_0 = \boldsymbol{n}_0\ \mathrm{d}\,a_0$, respectively. The deformation of an area can be expressed by $\mathrm{d}\,\boldsymbol{a}_\mathrm{t} = J\,\boldsymbol{F}^{-T} \cdot \mathrm{d}\,\boldsymbol{a}_0$. This allows the transformation of eq. (2.22) and eq. (2.21) into:

$$\boldsymbol{t}_{0,t} = \underbrace{\left(J\,\boldsymbol{\sigma} \cdot \boldsymbol{F}^{-T}\right)}_{=:\boldsymbol{P}} \cdot \boldsymbol{n}_0. \tag{2.23}$$

The product of the two 2nd order tensors and the Jacobian is called the 1st Piola–Kirchhoff stress $\boldsymbol{P}$. Like $\boldsymbol{F}$, $\boldsymbol{P}$ is a 2-point tensor (one basis in spatial basis and one in material base). It is a non-symmetric tensor of 2nd order.

To get a stress measure in the current configuration only, the resulting force $\mathrm{d}\,\boldsymbol{r}_\mathrm{t}$ in reference configuration can be pushed forward as:

$$\begin{aligned} \mathrm{d}\,\boldsymbol{r}_0 &= \boldsymbol{F}^{-1} \cdot \mathrm{d}\,\boldsymbol{r}_\mathrm{t} \\ &= \boldsymbol{F}^{-1} \cdot \boldsymbol{t}_{\mathrm{t},0}\ \mathrm{d}\,a_0, \end{aligned} \tag{2.24}$$

with $\boldsymbol{t}_0 := \boldsymbol{F}^{-1} \cdot \boldsymbol{t}_{t,0}$ being called the 2nd Piola–Kirchhoff traction vector and

$$\boldsymbol{t}_0 = \underbrace{\left(J\,\boldsymbol{F}^{-1} \cdot \boldsymbol{\sigma} \cdot \boldsymbol{F}^{-T}\right)}_{=:\boldsymbol{S}} \cdot \boldsymbol{n}_0 \tag{2.25}$$

holds. The tensor $\boldsymbol{S}$ is called the 2nd Piola–Kirchhoff stress tensor. It is a pure material, symmetric tensor of 2nd order. The 2nd Piola–Kirchhoff stress tensor is the pull back of the Cauchy stress tensor.

In static equilibrium, no forces are acting on the body forcing parts of it to change their position. If a body is in static equilibrium the components of the Cauchy stress tensor in every material point in the body satisfy the following equilibrium condition:

$$\sigma_{ji,j} = 0, \tag{2.26}$$

which is written in the large strain formulation conveniently as (Volokh, 2007)

$$\begin{aligned} \mathbf{0} &= \operatorname{Div} \boldsymbol{P} \\ &= \boldsymbol{\nabla} \cdot \boldsymbol{P}. \end{aligned} \tag{2.27}$$

2.2 Crystal Plasticity

A CP model is a constitutive law, *i.e.* it relates the response of a material to an external load. Using the terminology introduced before, a CP model relates a stress (see subsection 2.1.3 "*Stress Measures*") to a strain (see subsection 2.1.2 "*Strain Measures*")[1]. This relation is necessary to complement the (static) mechanical equilibrium eq. (2.27) and the strain compatibility condition eq. (2.19). In comparison to other, *e.g.* more general constitutive laws, CP models take into account the anisotropic stress–strain relation of crystalline materials, such as metals or water ice. The reason for the anisotropic behaviour of crystalline materials is the regular arrangement of atoms in the solid state. Two close-packed arrangements are possible: the face-centered cubic (fcc) and the hexagonal close-packed (hcp) lattice structure. The hcp structure is, however, only a model and real crystallites have hexagonal (hex) structures with a stacking order like hcp, but a c/a-ratio different from the ideal value of $c/a \approx 1.633$. A third important lattice structure exists for metals: the body-centered cubic (bcc). It is not a closest packed lattice, but its volume ratio is close to the highest possible ratio achieved by hcp and fcc (Gottstein, 2004). Most metals and alloys of technical interest solidify in one of these three structures.

Notation of crystallographic directions

Directions and planes in cubic crystal structures are usually described using the Miller index notation. For convenience reasons, hex structures are usually notated in the Bravais–Miller notation that extends the 3 digits of the Miller notation by a fourth, linearly dependent digit. The digits are written in square brackets $[h\,k\,l]$ for the direction given by the vector $\eta \cdot (h, k, l)$, with η being an arbitrary factor. A negative direction is denoted by a bar as in $[\bar{1}\,1\,0]$ for direction $(-1, 0, 0)$. The family of crystal directions that are equivalent to the direction $[h\,k\,l]$ is notated as $\langle h\,k\,l \rangle$ (in angle brackets). The plane orthogonal to the direction $\eta \cdot (u, v, w)$ is written in normal brackets: $(u\,v\,w)$. The notation $\{l\,m\,n\}$ (in curly brackets) is used for all planes that are equivalent to $(u\,v\,w)$ by the symmetry of the lattice.

To express (lattice) rotations in the 3 dimensional space, often Euler angles are used. The 3 Euler angles define a rotation around a certain fixed axis and, hence, a convention for axis definition and rotation order is needed. Typically,

1 For most material behaviour this view is too simplistic, since loading conditions are of importance as well.

the (z, x', z") convention is used and the angles are named φ_1,Φ,φ_2 (Bunge–Euler notation). A simple rotation, bringing the [0 1 0] direction pointing to [0 0 1] is given by the three angles $\varphi_1 = 0.0, \Phi = 90.0, \varphi_2 = 0.0$.

Here, first the conceptual details of the CP framework DAMASK are outlined, followed by a brief presentation of the exact CP models used in this work in subsection 2.2.1 "*Isotropic Material Model*" and subsection 2.2.2 "*Phenomenological Material Model*". While the DAMASK framework provides more advanced, physical-based models (incorporating *e.g.* TWIP effects, (Steinmetz et al., 2013), or dislocation flux, Reuber et al., 2014), getting the correct values for the constitutive parameters (whose number is increasing with increasing complexity of the model) requires much higher efforts without guaranteeing a better physical understanding of the mechanical behaviour.

In CP modelling, it is common practice to multiplicatively split up the deformation gradient $\boldsymbol{F}$ into an elastic part, $\boldsymbol{F}_\mathrm{e}$, and a plastic part, $\boldsymbol{F}_\mathrm{p}$ (Reina et al., 2014):

$$\boldsymbol{F} = \boldsymbol{F}_\mathrm{e}\boldsymbol{F}_\mathrm{p} \Leftrightarrow \boldsymbol{F}_\mathrm{e} = \boldsymbol{F}\,{\boldsymbol{F}_\mathrm{p}}^{-1} \Leftrightarrow \boldsymbol{F}_\mathrm{p} = {\boldsymbol{F}_\mathrm{e}}^{-1}\boldsymbol{F}. \tag{2.28}$$

The split is introduced to the combined elastic–plastic response usually seen in metals. For small strains (and short loading times), the behaviour is usually purely elastic, *i.e.* reversible. As usual, linear (Hookean) elasticity is assumed in DAMASK. Hence, the second Piola–Kirchhoff stress depends on the elastic Green–Lagrange strain via the anisotropic elastic stiffness $\mathbb{C}$. This relation is written in an artificial, only elastically deformed configuration that is called the "intermediate configuration"[1] (Roters et al., 2010a):

$$\boldsymbol{S} = \mathbb{C}\,({\boldsymbol{F}_\mathrm{e}}^{\mathrm{T}}\boldsymbol{F}_\mathrm{e} - \boldsymbol{I})/2. \tag{2.29}$$

Since $\mathbb{C}$ relates two symmetric tensors, it is itself symmetric and usually the $3\times3\times3\times3$ tensor is written as a 6×6 matrix. Depending on the crystal lattice, $\mathbb{C}$ takes a special form and can be expressed by 3 (cubic structures, *i.e.* bcc and fcc) or 5 (hex) variables only.

The stress $\boldsymbol{S}$ is acting as a driving force for the plastic velocity gradient $\boldsymbol{L}_\mathrm{p}$. $\boldsymbol{L}_\mathrm{p}$ depends on the underlying microstructure represented by a state variable vector $\boldsymbol{\xi}$ of the plasticity model and possibly other variables:

$$\boldsymbol{L}_\mathrm{p} = \boldsymbol{f}(\boldsymbol{S},\boldsymbol{\xi},...) \tag{2.30}$$

with $\boldsymbol{f}$ depending on the details of the used plasticity model.

1 Comparing to section 2.1.1 shows that it is formally equivalent to the stress–strain relation in the reference configuration. The given relation is therefore a valid approximation for small elastic strains, where the difference between reference and intermediate configuration is negligible.

From eq. (2.6) follows

$$\boldsymbol{L}_\mathrm{p} = \dot{\boldsymbol{F}}_\mathrm{p}\boldsymbol{F}_\mathrm{p}^{-1} \Leftrightarrow \dot{\boldsymbol{F}}_\mathrm{p} = \boldsymbol{L}_\mathrm{p}\boldsymbol{F}_\mathrm{p}. \tag{2.31}$$

The rate of the plastic deformation $\dot{\boldsymbol{F}}_\mathrm{p}$ depends not only on the state of the material, but also on the loading: After reaching the yield stress or for long holding times, the material typically deforms plastically (Sedláček, 2009). The plastic deformation remains even when the material is not under loading any more.

The set of non-linear eqs. (2.28) to (2.31), for which the dependency is summarised in fig. 2.2 needs to be solved iteratively. In DAMASK, a Newton-Raphson scheme is used to do that. Since $\boldsymbol{L}_\mathrm{p}$ is used as a predictor, the tangent $\frac{\partial \boldsymbol{L}_\mathrm{p}}{\partial \boldsymbol{S}}$ needs to be computed as well by the plasticity model. More details about the implementation are given by Kords (2013).

The core of each CP model is the formulation of eq. (2.30). In this equation, the plastic deformation of the material and its dependence to the aforementioned influences is incorporated. While some models take only dislocation glide as a carrier of plastic deformation into account, others include additionally mechanical twinning, phase transformations, etc. Depending on the crystal structure, different planes are densely packed and therefore the preferred slip planes. For fcc these are the $\{1\,1\,1\}$, for bcc the $\{1\,1\,0\}$ or $\{1\,1\,2\}$, and for hex usually at least the $\{0\,0\,0\,1\}$ planes. Typically densely packed directions serve as slip directions; these are $\langle 1\,1\,0\rangle$ for fcc and $\langle 1\,1\,1\rangle$ for bcc. For hex usually $\langle 1\,1\,2\,0\rangle$ is the preferred slip direction on $\{0\,0\,0\,1\}$ planes.

As it can be seen from eq. (2.30), the material response depends on the state $\boldsymbol{\xi}$. Therefore, any CP model needs to be completed by a second equation that describes the evolution of the state:

$$\dot{\boldsymbol{\xi}} = \boldsymbol{g}(\boldsymbol{S},\boldsymbol{\xi},...), \tag{2.32}$$

where the details again depend on the selected model. In DAMASK, various integration schemes for the state update exist (Kords, 2013). The two integration schemes are performed staggered, *i.e.* eqs. (2.28) to (2.31) are solved at a fixed plastic state, followed by a state update, the solution of eqs. (2.28) to (2.31), and so forth until a converged solution is achieved within the given tolerances.

Using eqs. (2.23) and (2.25) for conversion from $\boldsymbol{P}$ to $\boldsymbol{S}$ a CP model (*i.e.* eqs. (2.28) to (2.31) can be summarised as

$$\boldsymbol{P}(\boldsymbol{x}) = \boldsymbol{f}(\boldsymbol{x}, \boldsymbol{F}, \boldsymbol{\xi}, ...) \tag{2.33}$$

which is a stress–strain relation with additional dependence on the state and—denoted by "…"—external boundary conditions (BCs) like loading rate and temperature.

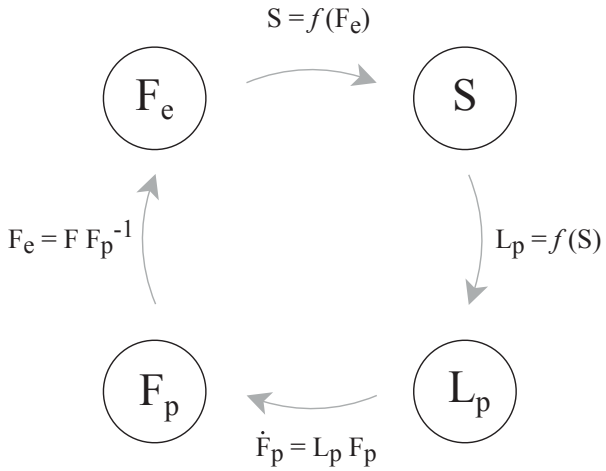

Figure 2.2: Generalised elasto-viscoplastic calculation loop.

2.2.1 Isotropic Material Model

The isotropic formulation is not a CP model, but a simplification of the phenomenological material model. No slip or twin systems are incorporated, *i.e.* when using this model for metals their crystalline structure—and hence, their orientation dependent behaviour—is neglected. The (scalar) VON MISES stress that is related to the second invariant J_2 of the deviatoric stress $\boldsymbol{S}^* = \operatorname{dev} \boldsymbol{S}$, is assumed to drive dislocation motion. Plastic shear occurs at the rate

$$\dot{\gamma} = \dot{\gamma}_0 \left(\frac{\sqrt{3 J_2}}{M\,\xi} \right)^n = \dot{\gamma}_0 \left(\sqrt{\frac{3}{2}} \frac{||\boldsymbol{S}^*||_\mathrm{F}}{M\,\xi} \right)^n \tag{2.34}$$

with the reference shear rate $\dot{\gamma}_0$, the stress exponent n, and the orientation (TAYLOR) factor M. The scalar material state, *i.e.* the resistance to plastic flow ξ, evolves asymptotically towards ξ_∞ with plastic shear γ according to the relationship

$$\dot{\xi} = \dot{\gamma}\, h_0 \left| 1 - \frac{\xi}{\xi_\infty} \right|^a \operatorname{sgn} \left(1 - \frac{\xi}{\xi_\infty} \right) \tag{2.35}$$

with parameters h_0 and a. The plastic velocity gradient $\boldsymbol{L}_\mathrm{p}$ scales with the rate of shear and its "direction" is set equivalent to that of $\boldsymbol{S}^*$:

$$\boldsymbol{L}_\mathrm{p} = \frac{\dot{\gamma}}{M} \frac{\boldsymbol{S}^*}{||\boldsymbol{S}^*||_\mathrm{F}}, \tag{2.36}$$

i.e. eqs. (2.34) and (2.36) make up a concrete formulation for eq. (2.30) and eq. (2.35) makes up one for eq. (2.32).

2.2.2 Phenomenological Material Model

This model is based on the assumption that plastic deformation occurs on a slip or twin system when the resolved shear stress exceeds a critical value, *i.e.* it is not capable of resolving twin formation spatially. The resolved shear stress depends on the amount of the applied stress, the angle between loading and the plane normal, and the angle between loading and the slip direction. The exact relation is known as SCHMIDS law (Gottstein, 2004). The widely used model was first described by Hutchinson (1976) for fcc crystals and is implemented in DAMASK for fcc, bcc, and hex crystal structures.

The microstructural state is parametrised in terms of resistances ξ on $N_{\mathrm{s+t}} = N_{\mathrm{s}} + N_{\mathrm{t}}$ slip and twin system.

The resistances on the $k = 1, \ldots, N_{\mathrm{s}}$ slip systems evolve from their initial value ξ_0 asymptotically to a system dependent saturation value with shear γ^m on all slip systems according to the relationship

$$\dot{\xi}^k = h_{0,\mathrm{slipslip}} \sum_{m=1}^{N_{\mathrm{s}}} |\dot{\gamma}^m| \left| 1 - \frac{\xi^m}{\xi^m_\infty} \right|^a \operatorname{sgn}\left(1 - \frac{\xi^m}{\xi^m_\infty}\right) h_{km} + h_{0,\mathrm{sliptwin}} \sum_{m=1}^{N_{\mathrm{t}}} \dot{\gamma}^m h_{km}, \quad (2.37)$$

where h_{km} is an interaction matrix and h_0 and a are system dependent fitting parameters; ξ_∞ is bounding the resistance evolution.

The resistances on the $k = 1, \ldots, N_{\mathrm{t}}$ twin systems evolve in a similar way and depend on shear on slip and twin systems:

$$\dot{\xi}^k = h_{0,\mathrm{twinslip}} \sum_{m=1}^{N_{\mathrm{s}}} |\dot{\gamma}^m| \, h_{km} + h_{0,\mathrm{twintwin}} \sum_{m=1}^{N_{\mathrm{t}}} \dot{\gamma}^m h_{km}. \quad (2.38)$$

Since this evolution has no upper bound, additionally the twin volume fraction on all twin system needs to be limited to a value less than 1.0.

Given a set of current slip resistances, shear on each slip system evolves at a rate of

$$\dot{\gamma}^k = \dot{\gamma}_0 \left| \frac{\tau^k}{\xi^k} \right|^n \operatorname{sgn}\left(\tau^k\right), \quad (2.39)$$

with $\tau^k = \boldsymbol{S} \cdot (\boldsymbol{s}^k \otimes \boldsymbol{n}^k)$ being—according to SCHMIDS law—the resolved shear stress for applied stress $\boldsymbol{S}$ and the unit vectors along the slip direction $\boldsymbol{s}^k$ and along the slip plane normal $\boldsymbol{n}^k$.

Again, slip due to mechanical twinning is handled in a slightly different way that accounts for the unidirectional character of twin formation:

$$\dot{\gamma}^k = \left(1 - \sum_{m=1}^{N_{\mathrm{t}}} \gamma^m / \gamma^m_{tw}\right) \dot{\gamma}_0 \left| \frac{\tau^k}{\xi^k} \right|^n \mathcal{H}\left(\tau^k\right), \quad (2.40)$$

where $\mathcal{H}$ is the HEAVISIDE function and γ_{tw} the specific shear due to mechanical twinning with a value depend on the twin system.

The sum of slip and twin shear determines the plastic velocity gradient:

$$\boldsymbol{L}_\mathrm{p} = \left(1 - \sum_{m=1}^{N_t} \gamma^m / \gamma^m_{\mathrm{tw}}\right) \sum_{k=1}^{N_s} \dot{\gamma}^k \, \boldsymbol{s}^k \otimes \boldsymbol{n}^k + \sum_{k=1}^{N_t} \dot{\gamma}^k \, \boldsymbol{s}^k \otimes \boldsymbol{n}^k. \tag{2.41}$$

Comparing eq. (2.41) with eq. (2.36) and eqs. (2.37) and (2.38) with eq. (2.35) shows how the slip/twin resolved formulation allows a more detailed description of plastic behaviour. The drawback is that it is computationally more expensive *e.g.* the number of state variables increases from 1 to $N_{\mathrm{s+t}}$.

2.3 Spectral Solver

For general cases, the solution for (static) equilibrium and strain compatibility under the given BCs has to be found numerically. A variety of numerical techniques exist for solving the differential equations. However, only two of them are frequently used: The FEM and the spectral method using fast FOURIER transform (FFT). The idea of using this spectral method for the solution of the mechanical boundary value problem was first introduced by Moulinec et al. (1994, 1998). Limited to periodic BCs, this technique usually exceeds the FEM in terms of solution quality because it uses trigonometric polynomials as ansatz functions. Moreover, since it operates in FOURIER space, the use of FFT allows for a very time- and memory-efficient iterative solution algorithm. Various improvements and extensions were reported in the recent years: Lebensohn (2001) extended it to the context of crystal viscoplasticity and showed the application in a number of studies (Lebensohn et al., 2005, 2011; Lee et al., 2011; Lefebvre et al., 2012). CP-based constitutive laws have been successfully employed by Lebensohn et al. (2012) Kanjarla et al. (2012), Suquet et al. (2012), and Grennerat et al. (2012).

Simulations of heterogeneous materials, however, are limited by the slow convergence of the original fixed-point iterative method when it is applied to materials with a large contrast in the local stiffness (Michel et al., 2001). Several approaches have been proposed to overcome this limitation. Accelerated schemes have been introduced by Eyre et al. (1999) and Monchiet et al. (2012) for materials with large property contrasts. Michel et al. (2001) suggested a method based on augmented LAGRANGIANS that also works in the case of materials with infinite property contrast. Using the original formulation and substituting the fixed-point method by advanced solution methods is another option to improve convergence as shown by Zeman et al. (2010) and Brisard et al. (2010).

Eisenlohr et al. (2013) proposed a flexible implementation into DAMASK that is based—in contrast to aforementioned works—on the large strain formulation of Lahellec et al. (2001). This formulation is presented here, following closely and based on Eisenlohr et al. (2013) and the extension by Shanthraj et al. (2015).

In the following, two alternative formulations are given in section 2.3.1 followed by the concrete implementation details in section 2.3.2. For the visualisation the results obtained by the spectral solver, a reconstruction of a displacement field from a

deformation gradient field is needed and the used method is presented in section 2.3.3. This section ends with a comparison to the finite element method and stability benchmarks.

2.3.1 Formulation

The deformation map $\boldsymbol{\chi}(\boldsymbol{x}) : \boldsymbol{x} \in \mathcal{B}_0 \rightarrow \boldsymbol{y} \in \mathcal{B}_\mathrm{t}$ introduced in section 2.1.1 is expressed as a sum of a homogeneous deformation, characterised by a constant deformation gradient $\overline{\boldsymbol{F}}$, and a superimposed deformation fluctuation field $\tilde{\boldsymbol{w}}$,

$$\boldsymbol{\chi}(\boldsymbol{x}) = \overline{\boldsymbol{F}}\boldsymbol{x} + \tilde{\boldsymbol{w}}(\boldsymbol{x}), \tag{2.42}$$

for which periodicity conditions hold, *i.e.* $\tilde{\boldsymbol{w}}^- = \tilde{\boldsymbol{w}}^+$ on corresponding surfaces $\partial\mathcal{B}^-$ and $\partial\mathcal{B}^+$.

Equation (2.42) allows writing the deformation gradient $\boldsymbol{F}$ as the sum of a spatially homogeneous deformation part, $\overline{\boldsymbol{F}}$, and a locally fluctuating displacement part, $\tilde{\boldsymbol{F}}$:

$$\boldsymbol{F} = \overline{\boldsymbol{F}} + \tilde{\boldsymbol{F}}. \tag{2.43}$$

The material response eq. (2.33) is formally written as a relation between the deformation gradient, $\boldsymbol{F}$ and the first Piola–Kirchhoff stress, $\boldsymbol{P}$, through a strain energy density functional, $\mathcal{W}$:

$$\boldsymbol{P}(\boldsymbol{x}) = \frac{\delta\mathcal{W}}{\delta\boldsymbol{F}(\boldsymbol{x})} = \boldsymbol{f}(\boldsymbol{x}, \boldsymbol{F}, \boldsymbol{\xi}, ...). \tag{2.44}$$

Based on eqs. (2.42) to (2.44), two formulations are presented in the following, namely a direct variational formulation and a mixed variational formulation.

Direct Variational Formulation

The original spectral method by Moulinec et al. (1994) is based on a direct variational formulation. Since the CP models in DAMASK are written in a large strain framework, the form of Lahellec et al. (2001) is used in Eisenlohr et al. (2013) and presented here. In contrast to the work by Moulinec et al. (1994) and Lahellec et al. (2001), here it is written in a more general form that allows using different numerical solvers instead of the original fixed-point approach as outlined by Shanthraj et al. (2015)

In this formulation, the equilibrated deformation field is obtained by minimising $\mathcal{W}$ over all deformation fields fulfilling eq. (2.42) for an externally prescribed average deformation. Static equilibrium expressed in real (see eq. (2.27)) and Fourier[1] space

1 Quantities in real space and Fourier space are distinguished by notation $Q(\boldsymbol{x})$ and $Q(\boldsymbol{k})$, respectively, with $\boldsymbol{x}$ the position in real space, $\boldsymbol{k}$ the frequency vector in Fourier space, and $i^2 = -1$. $\mathcal{F}^{-1}[\cdot]$ denotes the inverse Fourier transform.

follows as:

$$\min_{\boldsymbol{\chi}} \mathcal{W} \implies \operatorname{Div} \boldsymbol{P}(\boldsymbol{x}) = \mathcal{F}^{-1}\left[\boldsymbol{P}(\boldsymbol{k})\, i\, \boldsymbol{k}\right] = \boldsymbol{0}, \tag{2.45}$$

which is equivalent to finding the root of the residual body force field

$$\mathscr{F}\left[\boldsymbol{\chi}(\boldsymbol{k})\right] := \boldsymbol{P}(\boldsymbol{k})\, i\, \boldsymbol{k} = \boldsymbol{0}. \tag{2.46}$$

The differential eq. (2.46) in Fourier space is numerically difficult to solve because of its high condition number. Introducing, in the spirit of Eshelby and Mura (1987), a linear comparison material of stiffness $\mathbb{D}$ allows reformulating to an equivalent problem $\boldsymbol{P}(\boldsymbol{x}) = \mathbb{D}\boldsymbol{F}(\boldsymbol{x}) = \mathbb{D}\operatorname{Grad}\boldsymbol{\chi}$ with better numerical properties, *i.e.* a lower condition number. Equilibrium in this reference material is fulfilled if, for a given deformation map $\boldsymbol{\chi}$, the residual body force field vanishes

$$\mathscr{P}\left[\boldsymbol{\chi}(\boldsymbol{k})\right] := \mathbb{D}\left[\boldsymbol{\chi}(\boldsymbol{k}) \otimes i\, \boldsymbol{k}\right]\, i\, \boldsymbol{k} = \boldsymbol{A}(\boldsymbol{k})\, \boldsymbol{\chi}(\boldsymbol{k}) = \boldsymbol{0}. \tag{2.47}$$

The acoustic tensor $\boldsymbol{A}(\boldsymbol{k})$ is a shorthand notation for $\boldsymbol{A}(\boldsymbol{k})\, \boldsymbol{a}(\boldsymbol{k}) := \mathbb{D}\left[\boldsymbol{a}(\boldsymbol{k}) \otimes i\, \boldsymbol{k}\right]\, i\, \boldsymbol{k}$ for any given vector field $\boldsymbol{a}(\boldsymbol{k})$. It corresponds to an operator on a deformation map producing the body forces resulting in the reference material. The inverse $\boldsymbol{A}^{-1}$ therefore gives the deformation map that would result from a known body force field in the reference material. This deformation map vanishes iff the body force field vanishes, *i.e.*, in static equilibrium, since $\boldsymbol{A}(\boldsymbol{k})$ is non-zero at all considered frequencies (*i.e.* $\forall\, \boldsymbol{k} \neq \boldsymbol{0}$) and if the stiffness $\mathbb{D}$ is—as usually—positive-definite. Next, an operator that results in the deformation map causing the same body force field in the reference material as a given deformation map in the original material is defined. This corresponds to a preconditioning operation of $\mathscr{P}^{-1}$ on the non-linear operator $\mathscr{F}$. $\mathscr{P}$ is straightforward to invert since it is local in $\boldsymbol{k}$, with $\mathscr{P}^{-1} = \boldsymbol{A}(\boldsymbol{k})^{-1}$. The preconditioned system thus reads:

$$\mathscr{P}^{-1}\mathscr{F}\left[\boldsymbol{\chi}(\boldsymbol{k})\right] = \boldsymbol{A}(\boldsymbol{k})^{-1}\boldsymbol{P}(\boldsymbol{k})\, i\, \boldsymbol{k} = \boldsymbol{0} \qquad \forall\, \boldsymbol{k} \neq \boldsymbol{0}. \tag{2.48}$$

The deformation gradient field corresponding to this deformation map is obtained from the gradient in real space of eq. (2.48)

$$\mathscr{P}^{-1}\mathscr{F}\left[\boldsymbol{\chi}(\boldsymbol{k})\right] \otimes i\, \boldsymbol{k} = \left[\boldsymbol{A}(\boldsymbol{k})^{-1}\boldsymbol{P}(\boldsymbol{k})\, i\, \boldsymbol{k}\right] \otimes i\, \boldsymbol{k} = \boldsymbol{0} \qquad \forall\, \boldsymbol{k} \neq \boldsymbol{0}. \tag{2.49}$$

This is equivalent to eq. (2.48) except for a constant residual field, *i.e.* at $\boldsymbol{k} = \boldsymbol{0}$ where the prescribed average deformation gradient is known to hold anyway. Expressed in terms of the deformation gradient field, eq. (2.49), reads

$$\mathscr{F}_{\text{direct}}\left[\boldsymbol{F}(\boldsymbol{k})\right] := \mathbb{\Gamma}(\boldsymbol{k})\, \boldsymbol{P}(\boldsymbol{k}) = \boldsymbol{0} \qquad \forall\, \boldsymbol{k} \neq \boldsymbol{0}, \tag{2.50}$$

where the Gamma operator $\mathbb{\Gamma}(\boldsymbol{k})$ is defined as a further shorthand notation to

$\mathbb{\Gamma}(\boldsymbol{k})\,\boldsymbol{T}(\boldsymbol{k}) := \left[\boldsymbol{A}(\boldsymbol{k})^{-1}\boldsymbol{T}(\boldsymbol{k})\,i\,\boldsymbol{k}\right] \otimes i\,\boldsymbol{k}$ for a tensor field $\boldsymbol{T}(\boldsymbol{k})$.

The solution given in eq. (2.50) allows violating the compatibility condition eq. (2.19). Compatibility has to be ensured by using a suitable root-finding algorithm as shown in section 2.3.2 "*Numerical Solution*".

The discretisation of eq. (2.50) results in the so-called basic scheme. Using a collocation-based approach at the grid points in real space, the resulting system of equations reads as:

$$\mathscr{F}_{\text{basic}}\left[\boldsymbol{F}(\boldsymbol{x})\right] := \mathcal{F}^{-1}\left[\begin{cases}\mathbb{\Gamma}(\boldsymbol{k})\,\boldsymbol{P}(\boldsymbol{k}) & \text{if } \boldsymbol{k} \neq \boldsymbol{0} \\ \Delta\boldsymbol{F}_{\text{BC}} & \text{if } \boldsymbol{k} = \boldsymbol{0}\end{cases}\right], \tag{2.51}$$

The desired deformation BC $\boldsymbol{F}_{\text{BC}}$ of the volume element is conveniently prescribed by setting $\Delta\boldsymbol{F}_{\text{BC}} = \overline{\boldsymbol{F}} - \boldsymbol{F}_{\text{BC}}$. This allows adjusting the deformation gradient such that a stress BC is fulfilled as shown later in section 2.3.2.

Mixed Variational Formulation

The idea of using a mixed variational formulation was firstly outlined by Michel et al. (2000) to overcome convergence problems with high phase contrast. Here, this idea is presented in a general form given by Shanthraj et al. (2015). In contrast to the direct variational formulation, in the mixed variational formulation the equilibrium deformation field (*i.e.* satisfying eq. (2.27)) is obtained by minimising $\mathcal{W}$ over all deformation gradient fields fulfilling eq. (2.42) for an externally prescribed average deformation. Additionally, contrary to the direct variational formulation the compatibility of the deformation gradient eq. (2.19) field is imposed as an auxiliary constraint in the mixed variational formulation.

$$\min_{\boldsymbol{F}} \mathcal{W}(\boldsymbol{F}) \quad \text{subject to} \quad \boldsymbol{F} = \operatorname{Grad}\boldsymbol{\chi}. \tag{2.52}$$

This can be reformulated as an unconstrained optimisation problem by introducing a Lagrange multiplier field, $\boldsymbol{\Lambda}(\boldsymbol{x})$, and a penalty term. Conveniently, the reference stiffness $\mathbb{D}$ as defined for the direct variational formulation is used as the penalty parameter. The resulting Lagrange multiplier functional reads

$$\begin{aligned}\mathcal{L}[\boldsymbol{F},\boldsymbol{\chi},\boldsymbol{\Lambda}] = \mathcal{W} & \\ + \int_{\mathcal{B}_0} \boldsymbol{\Lambda}(\boldsymbol{x}) \cdot \left[\operatorname{Grad}\boldsymbol{\chi}(\boldsymbol{x}) - \boldsymbol{F}(\boldsymbol{x})\right] \mathrm{d}\,\boldsymbol{x} & \\ + \frac{1}{2}\int_{\mathcal{B}_0} \left[\operatorname{Grad}\boldsymbol{\chi}(\boldsymbol{x}) - \boldsymbol{F}(\boldsymbol{x})\right] \cdot \mathbb{D}\left[\operatorname{Grad}\boldsymbol{\chi}(\boldsymbol{x}) - \boldsymbol{F}(\boldsymbol{x})\right] \mathrm{d}\,\boldsymbol{x}. &\end{aligned} \tag{2.53}$$

The equilibrium condition is equivalent to the saddle point of eq. (2.53) (for details see Fortin et al., 1983). This results in the following three stationary conditions:

$$\frac{\delta \mathcal{L}}{\delta \boldsymbol{F}(\boldsymbol{x})} = \boldsymbol{P}(\boldsymbol{x}) - \boldsymbol{\Lambda}(\boldsymbol{x}) + \mathbb{D}\Big\{\boldsymbol{F}(\boldsymbol{x}) - \operatorname{Grad}\boldsymbol{\chi}(\boldsymbol{x})\Big\} = \boldsymbol{0}, \tag{2.54a}$$

$$\frac{\delta \mathcal{L}}{\delta \boldsymbol{\chi}(\boldsymbol{x})} = \operatorname{Div}\Big[\boldsymbol{\Lambda}(\boldsymbol{x}) - \mathbb{D}\Big\{\boldsymbol{F}(\boldsymbol{x}) - \operatorname{Grad}\boldsymbol{\chi}(\boldsymbol{x})\Big\}\Big] = \boldsymbol{0}, \tag{2.54b}$$

$$\frac{\delta \mathcal{L}}{\delta \boldsymbol{\Lambda}(\boldsymbol{x})} = \operatorname{Grad}\boldsymbol{\chi}(\boldsymbol{x}) - \boldsymbol{F}(\boldsymbol{x}) = \boldsymbol{0}. \tag{2.54c}$$

After the application of the Fourier transform, it reads as:

$$\boldsymbol{P}(\boldsymbol{k}) - \boldsymbol{\Lambda}_0(\boldsymbol{k}) + \mathbb{D}\Big\{\boldsymbol{F}(\boldsymbol{k}) - \boldsymbol{\chi}(\boldsymbol{k}) \otimes i\,\boldsymbol{k}\Big\} = \boldsymbol{0} \tag{2.55a}$$

$$\boldsymbol{\chi}(\boldsymbol{k}) = \boldsymbol{A}(\boldsymbol{k})^{-1}\Big\{\mathbb{D}\boldsymbol{F}(\boldsymbol{k}) - \boldsymbol{\Lambda}_0(\boldsymbol{k})\Big\}\, i\,\boldsymbol{k} \tag{2.55b}$$

$$\boldsymbol{\chi}(\boldsymbol{k}) \otimes i\,\boldsymbol{k} - \boldsymbol{F}(\boldsymbol{k}) = \boldsymbol{0} \tag{2.55c}$$

with the Lagrange multiplier field relative to the reference configuration as $\boldsymbol{\Lambda}_0(\boldsymbol{x}) = \boldsymbol{F}(\boldsymbol{x})\boldsymbol{\Lambda}(\boldsymbol{x})$. Eliminating $\boldsymbol{\chi}$ from eqs. (2.55a) and (2.55c) using eq. (2.55b) gives the equilibrium deformation gradient field as the solution to:

$$\begin{aligned}\mathscr{F}_{\text{mixed}}\left[\boldsymbol{F}(\boldsymbol{k}), \boldsymbol{\Lambda}(\boldsymbol{k})\right] := &\begin{Bmatrix} \boldsymbol{P}(\boldsymbol{k}) - \boldsymbol{\Lambda}_0(\boldsymbol{k}) \\ +\mathbb{D}\big(\boldsymbol{F}(\boldsymbol{k}) - \mathbb{\Gamma}(\boldsymbol{k})(\mathbb{D}\boldsymbol{F}(\boldsymbol{k}) - \boldsymbol{\Lambda}_0(\boldsymbol{k}))\big) \\ \boldsymbol{F}(\boldsymbol{k}) - \mathbb{\Gamma}(\boldsymbol{k})(\mathbb{D}\boldsymbol{F}(\boldsymbol{k}) - \boldsymbol{\Lambda}_0(\boldsymbol{k})) \end{Bmatrix} \\ &= \boldsymbol{0}.\end{aligned} \tag{2.56}$$

The condition $\boldsymbol{F}(\boldsymbol{k}) - \mathbb{\Gamma}(\boldsymbol{k})\{\mathbb{D}\boldsymbol{F}(\boldsymbol{k}) - \boldsymbol{\Lambda}_0(\boldsymbol{k})\} = \boldsymbol{0}$ in eq. (2.56) is necessary and sufficient to enforce both the compatibility of the deformation gradient field, given by $\boldsymbol{F}(\boldsymbol{k}) - \mathbb{\Gamma}(\boldsymbol{k})\mathbb{D}\boldsymbol{F}(\boldsymbol{k}) = \boldsymbol{0}$, and equilibrium of the Lagrange multiplier field, given by $\mathbb{\Gamma}(\boldsymbol{k})\boldsymbol{\Lambda}_0(\boldsymbol{k}) = \boldsymbol{0}$ (for details see Monchiet et al., 2012). The condition $\boldsymbol{P}(\boldsymbol{k}) - \boldsymbol{\Lambda}_0(\boldsymbol{k}) = \boldsymbol{0}$ enforces equilibrium of the stress field corresponding to $\boldsymbol{F}$.

The mixed variational form is used for two collocation-based discretisation approaches at the grid points in real space: the Lagrange multiplier field-based scheme and the polarisation field-based scheme, both are outlined in the following.

Lagrange Multiplier Field-Based Scheme The Lagrange multiplier field-based scheme is based on the discretisation of the mixed variational formulation of the static equilibrium condition eq. (2.56) in real space. To get a well-conditioned system of equations, the inverse of the reference stiffness, $\mathbb{D}^{-1}$, introduced for the direct

variational formulation, is used to scale the stress terms in eq. (2.56).

$$\mathscr{F}_{\boldsymbol{\Lambda}}\left[\boldsymbol{F}(\boldsymbol{x}), \boldsymbol{F}_{\boldsymbol{\Lambda}}(\boldsymbol{x})\right] := \tag{2.57}$$
$$\begin{Bmatrix} \mathbb{D}^{-1}(\boldsymbol{P}(\boldsymbol{x}) - \boldsymbol{\Lambda}_0(\boldsymbol{x})) \\ +\beta\,\boldsymbol{F}(\boldsymbol{x}) - \mathcal{F}^{-1}\left[\begin{cases} \mathbb{\Gamma}(\boldsymbol{k})\left(\beta\,\mathbb{D}\boldsymbol{F}(\boldsymbol{k}) - \alpha\boldsymbol{\Lambda}_0(\boldsymbol{k})\right) & \text{if } \boldsymbol{k} \neq \boldsymbol{0} \\ \beta\,\boldsymbol{F}_{\mathrm{BC}} & \text{if } \boldsymbol{k} = \boldsymbol{0} \end{cases}\right] \\ \\ \beta\,\boldsymbol{F}(\boldsymbol{x}) - \mathcal{F}^{-1}\left[\begin{cases} \mathbb{\Gamma}(\boldsymbol{k})\left(\beta\,\mathbb{D}\boldsymbol{F}(\boldsymbol{k}) - \alpha\boldsymbol{\Lambda}_0(\boldsymbol{k})\right) & \text{if } \boldsymbol{k} \neq \boldsymbol{0} \\ \beta\,\boldsymbol{F}_{\mathrm{BC}} & \text{if } \boldsymbol{k} = \boldsymbol{0} \end{cases}\right] \end{Bmatrix}$$

where the Lagrange multiplier field relative to the reference configuration is determined through the relation $\boldsymbol{\Lambda}_0(\boldsymbol{x}) = \boldsymbol{F}(\boldsymbol{x})\mathbb{D}\boldsymbol{F}_{\boldsymbol{\Lambda}}(\boldsymbol{x})$. The coefficients α and β with default value $\alpha = \beta = 1.0$ enable to weight the conditions for static equilibrium and strain compatibility. Their optimal choice depends on the problem type, *e.g.* the ratio of increased or decreased stiffness compared to the average stiffness. Since the values of these parameters influence the convergence behaviour, they can be used to improve convergence rate and stability. A detailed study of the convergence rate is given by Moulinec et al. (2014) for a similar formulation in a small strain framework.

During the non-linear iterations, the deformation gradient field $\boldsymbol{F}(\boldsymbol{x})$ is corrected towards its compatible counterpart $\boldsymbol{F}_{\mathrm{c}}(\boldsymbol{x}) = \beta^{-1}\mathbb{\Gamma}(\boldsymbol{x}) * [\beta\,\mathbb{D}\boldsymbol{F}(\boldsymbol{x}) - \alpha\boldsymbol{\Lambda}_0(\boldsymbol{x})]$. This allows performing this convolution operation before the constitutive evaluation in the residual, eq. (2.57). The constitutive evaluation is performed on the compatible deformation gradient field $\boldsymbol{F}_{\mathrm{c}}(\boldsymbol{x})$ to accelerate convergence.

Polarisation Field-Based Scheme In the polarisation field-based scheme, the mixed variational formulation of the static equilibrium condition is expressed in terms of the deformation gradient field and a rescaled polarisation field, $\boldsymbol{F}_{\boldsymbol{\tau}}(\boldsymbol{x}) := \boldsymbol{F}_{\boldsymbol{\Lambda}}(\boldsymbol{x}) + \boldsymbol{F}(\boldsymbol{x})$. Following a similar discretisation procedure as for the Lagrange multiplier field-based scheme and substituting into eq. (2.56) gives

$$\mathscr{F}_{\boldsymbol{\tau}}\left[\boldsymbol{F}(\boldsymbol{x}), \boldsymbol{F}_{\boldsymbol{\tau}}(\boldsymbol{x})\right] := \tag{2.58}$$
$$\begin{Bmatrix} \mathbb{D}^{-1}(\boldsymbol{P}(\boldsymbol{x}) - \boldsymbol{\Lambda}_0(\boldsymbol{x})) \\ +\beta\,\boldsymbol{F}(\boldsymbol{x}) - \mathcal{F}^{-1}\left[\begin{cases} \mathbb{\Gamma}(\boldsymbol{k})\left(\beta\,\mathbb{D}\boldsymbol{F}(\boldsymbol{k}) - \alpha\boldsymbol{\Lambda}_0(\boldsymbol{k})\right) & \text{if } \boldsymbol{k} \neq \boldsymbol{0} \\ \beta\,\boldsymbol{F}_{\mathrm{BC}} & \text{if } \boldsymbol{k} = \boldsymbol{0} \end{cases}\right] \\ \\ \beta\,\boldsymbol{F}(\boldsymbol{x}) - \mathcal{F}^{-1}\left[\begin{cases} \mathbb{\Gamma}(\boldsymbol{k})\left(\beta\,\mathbb{D}\boldsymbol{F}(\boldsymbol{k}) - \alpha\boldsymbol{\Lambda}_0(\boldsymbol{k})\right) & \text{if } \boldsymbol{k} \neq \boldsymbol{0} \\ \beta\,\boldsymbol{F}_{\mathrm{BC}} & \text{if } \boldsymbol{k} = \boldsymbol{0} \end{cases}\right] \end{Bmatrix}.$$

The Lagrange multiplier field relative to the reference configuration is determined from the rescaled polarisation field though the relation $\boldsymbol{\Lambda}_0(\boldsymbol{x}) = \boldsymbol{F}(\boldsymbol{x})\mathbb{D}[\boldsymbol{F}_{\boldsymbol{\tau}}(\boldsymbol{x}) - \boldsymbol{F}(\boldsymbol{x})]$. The constitutive evaluation is conveniently performed on the compatible deformation

gradient field, $\boldsymbol{F}_{\mathrm{c}}(\boldsymbol{x}) = \beta^{-1}\mathbb{\Gamma}(\boldsymbol{x}) * [\beta\,\mathbb{D}\boldsymbol{F}(\boldsymbol{x}) - \alpha\boldsymbol{F}(\boldsymbol{x})\mathbb{D}\,\{\boldsymbol{F}_{\boldsymbol{\tau}}(\boldsymbol{x}) - \boldsymbol{F}(\boldsymbol{x})\}]$.

2.3.2 Implementation

Here, the important details of the implementation of the direct variational formulation and mixed variational formulation into DAMASK are briefly outlined. First, the FFT and its implementation details are presented in "*Fast* Fourier *Transform*". "*Reference Stiffness*" outlines the computation of the reference stiffness used for the various schemes and in "*Mixed Boundary Conditions*" the handling of stress BCs is detailed. How the root of the three schemes is found is subject of the following paragraph "*Numerical Solution*". A short summary of the resulting algorithm is giving in "*Algorithm*" and this subsection ends with the details of the convergence criteria.

Fast Fourier Transform

The discretisation of the formulation is done using a discrete Fourier transform (DFT). For that, the hexahedral domain $\mathcal{B}_0$ with side lengths d_x, d_y, d_z is discretised into a regular grid of $N_x \times N_y \times N_z = N$ points with unit spacing. The solution field is approximated in the discrete Fourier space associated with this real space grid. To achieve a reasonable performance, the FFT is used. The term FFT refers to a group of algorithms that compute the DFT in $\mathcal{O}(N \log N)$ operations. A free DFT implementation which has shown an excellent performance is the Fastest Fourier Transform in the West (Frigo et al., 2014) developed by Frigo et al. (2005). To further save memory and computation time, the complex conjugate symmetry resulting from the real space deformation gradient data is exploited.

Reference Stiffness

The choice of the reference stiffness has a strong influence on stability and convergence rate as shown by Michel et al. (2001). In absence of an analytic expression for the large strain formulation, similar to Michel et al. (2001), the reference stiffness $\mathbb{D}$ is selected as

$$\mathbb{D} = \frac{1}{2}\left(\arg\max \left|\left| \frac{\mathrm{d}\boldsymbol{P}}{\mathrm{d}\boldsymbol{F}}(\boldsymbol{x}) \right|\right|_{\mathrm{F}} + \arg\min \left|\left| \frac{\mathrm{d}\boldsymbol{P}}{\mathrm{d}\boldsymbol{F}}(\boldsymbol{x}) \right|\right|_{\mathrm{F}} \right). \tag{2.59}$$

Mixed Boundary Conditions

For both formulations the direct variational formulation, and the mixed variational formulation, the BCs are given in terms of the deformation gradient $\boldsymbol{F}_{\mathrm{BC}}$. In order to allow the (component-wise) prescription of stress BCs $\boldsymbol{P}_{\mathrm{BC}}$, an iterative adjustment[1]

1 The correction of the deformation gradient field, *i.e.* the actual spectral method procedure, is performed in parallel at these iterations.

of $\boldsymbol{F}_{\mathrm{BC}}$ needs to be done until the stress BCs are fulfilled. To do this, conveniently $\boldsymbol{F}_{\mathrm{BC}}$ is expressed in rate form, *i.e.* $\boldsymbol{F}_{\mathrm{BC}} = \dot{\boldsymbol{F}}_{\mathrm{BC}}\,\Delta t$ for a given time increment of length Δt. Within Δt the volume element is then subjected to a set of complementary BCs in terms of deformation rate $\dot{\boldsymbol{F}}_{\mathrm{BC}}$ and stress $\boldsymbol{P}_{\mathrm{BC}}$, where stress BCs must not allow for rigid body rotations. Components of both are mutually exclusive and, when not defined, set to zero in the following equation. These mixed BCs are translated into pure deformation BCs at iteration $n+1$ by setting

$$\left\{\boldsymbol{F}_{\mathrm{BC}}\right\}_{n+1} = \left\{\overline{\boldsymbol{F}}\right\}_{n=0} + \dot{\boldsymbol{F}}_{\mathrm{BC}}\,\Delta t - \left\{\overline{\left(\frac{\partial \boldsymbol{F}}{\partial \boldsymbol{P}}\right)}\right\}_{n} \left(\left\{\overline{\boldsymbol{P}}\right\}_{n} - \boldsymbol{P}_{\mathrm{BC}}\right). \tag{2.60}$$

The last term in eq. (2.60) corrects for deviations from the prescribed stress BCs. The average compliance $\overline{\partial \boldsymbol{F}/\partial \boldsymbol{P}}$ required for this is estimated with the following computation procedure:

1. spatially average the tangent modulus $\partial \boldsymbol{P}/\partial \boldsymbol{F}$ known at each grid point from the constitutive model;
2. transform the fourth-order tensor into a 9×9 matrix;
3. drop all rows mn and columns kj for which no stress BCs are defined at mn or kj;
4. invert the reduced square matrix;
5. re-insert zero-filled rows and columns at mn and kj that were dropped before;
6. transform back to a regular fourth-order tensor.

Numerical Solution

The non-linear solution methods to solve the resulting systems of discretised equations are taken from the portable, extensible toolkit for scientific computation (PETSc) developed by Balay et al. (2013) and PETSc Team (2015). The residual results from evaluating eq. (2.51), eq. (2.57), or eq. (2.58) at the grid points. The convolution operation is performed in the discrete Fourier space associated with the same grid with the help of the FFT.

In Shanthraj et al. (2015), three solution methods implemented in PETSc are compared: the non-linear Richardson method (Kelley, 1995), the non-linear generalised minimal residual method (GMRES) method (Oosterlee et al., 2000) and the inexact Newton-GMRES method (Chen et al., 2006). In these methods, an existing solution $\{\square\}_n$ at iteration n is iteratively improved until the prescribed convergence criteria are satisfied. Here, the notation $\{\square\}$ is used here as a placeholder that represents $\{\boldsymbol{F}(\boldsymbol{x})\}$ in the basic scheme, $\{\boldsymbol{F}(\boldsymbol{x}), \boldsymbol{F}_{\boldsymbol{\Lambda}}(\boldsymbol{x})\}$ in the Lagrange multiplier field-based scheme, or $\{\boldsymbol{F}(\boldsymbol{x}), \boldsymbol{F}_{\boldsymbol{\tau}}(\boldsymbol{x})\}$ in the polarisation field-based scheme.

Non-linear RICHARDSON The non-linear RICHARDSON method iteratively improves a solution $\{\square\}_n$ found at iteration n through the update

$$\{\square\}_{n+1} = \{\square\}_n - \mathscr{F}\{\square\}_n . \tag{2.61}$$

When applied to the direct variational formulation, this is equivalent to the approach presented by Moulinec et al. (1998) in a finite-strain formulation (see Eisenlohr et al., 2013). Strain compatibility of the deformation gradient field is ensured in this case because, as for an arbitrary second order tensor field $\boldsymbol{T}(\boldsymbol{x})$, the convolution with $\mathbb{\Gamma}(\boldsymbol{x})$ ensures a compatible solution (Lahellec et al., 2001).

When applied to the set of equations resulting from the LAGRANGE multiplier field-based scheme or polarisation field-based scheme, this is the finite-strain formulation of the polarisation scheme by Monchiet et al. (2012).

Non-linear GMRES In the non-linear GMRES method an updated solution, $\{\square\}_{n+1}$, is found as the linear combination of the m previous solutions spanning a KRYLOV subspace $\mathcal{K}_n = \operatorname{span}\left\{\{\square\}_n, \cdots, \{\square\}_{n-m+1}\right\}$ for which the norm of the linearised residual is minimal

$$\min_{\{\square\}_{n+1}\in\mathcal{K}_n} \left|\left| \frac{\partial\mathscr{F}}{\partial\{\square\}_n}\left[\{\square\}_{n+1} - \{\square\}_n\right] + \mathscr{F}\{\square\}_n \right|\right|_2 . \tag{2.62}$$

This residual is approximated by PETSc in a JACOBIAN-free way (Oosterlee et al., 2000).

Applied to the basic system of equations, compatibility of the deformation gradient is ensured since each deformation gradient field is a linear combination of compatible fields.

Inexact NEWTON-GMRES In NEWTON methods, an existing solution $\{\square\}_n$ is incrementally updated to $\{\square\}_{n+1} = \{\square\}_n + \{\Delta\square\}_n$ with each NEWTON step given by

$$\begin{aligned} &\frac{\partial\mathscr{F}}{\partial\{\square\}_n}\{\Delta\square\}_n = -\mathscr{F}\{\square\}_n \\ \Leftrightarrow &\left|\left| \frac{\partial\mathscr{F}}{\partial\{\square\}_n}\{\Delta\square\}_n + \mathscr{F}\{\square\}_n \right|\right|_2 = 0. \end{aligned} \tag{2.63}$$

To increase the efficiency of such an algorithm, eq. (2.63) is solved only in an inexact fashion:

$$\left|\left| \frac{\partial\mathscr{F}}{\partial\{\square\}_n}\{\Delta\square\}_n + \mathscr{F}\{\square\}_n \right|\right|_2 \leq \eta_n \left|\left|\mathscr{F}\{\square\}_n\right|\right|_2 , \tag{2.64}$$

where the tolerance for a vanishing norm of the residual is gradually tightened, *i.e.* $\eta_n \to 0$, with increasing iteration count (Eisenstat et al., 1996).

Within each Newton iteration, the typically large linear system (2.64) is solved for $\{\Delta\square\}_n$ by means of the GMRES method where the k^{th} GMRES iterate of the Newton step is given by

$$\min_{\{\Delta\square\}_n^k \in \mathcal{K}_k} \left\| \frac{\partial \mathscr{F}}{\partial \{\square\}_n} \{\Delta\square\}_n^k + \mathscr{F}\{\square\}_n \right\|_2 \tag{2.65}$$
$$\text{where} \quad \mathcal{K}_k = \operatorname{span}\left\{ \frac{\partial \mathscr{F}}{\partial \{\square\}_n} \{\Delta\square\}_n^{k-1}, \cdots, \frac{\partial \mathscr{F}}{\partial \{\square\}_n} \{\Delta\square\}_n^{k-m} \right\}$$

and $\mathcal{K}_0 = \operatorname{span}\{-\mathscr{F}\{\square\}_n\}$. Since the discretisation of the Jacobian is dense and numerically difficult to handle, a finite difference approximation

$$\frac{\partial \mathscr{F}}{\partial \{\square\}_n} \{\Delta\square\}_n^k \approx \frac{\mathscr{F}\left[\{\square\}_n + \epsilon \{\Delta\square\}_n^k\right] - \mathscr{F}\{\square\}_n}{\epsilon} \tag{2.66}$$

is used to update the Krylov subspace $\mathcal{K}_k$.

Compatibility of the deformation gradient field is preserved when this method is applied to the basic system of equations for a compatible Newton step. This follows from eq. (2.65) and the observation that $\mathcal{K}_k$ is spanned by compatible fields since $\frac{\partial \mathscr{F}_{basic}}{\partial \boldsymbol{x}} = \mathbb{\Gamma}(\boldsymbol{x}) * \frac{\partial \boldsymbol{P}}{\partial \boldsymbol{F}}(\boldsymbol{x})$.

Algorithm

For a given time step, the solution is found iteratively. The iterative scheme, here shown for the direct variational formulation, consists of the following steps:

1. evaluate the constitutive response at all points (including tangent)
2. determine correction to deformation gradient BCs to fulfil stress BCs
3. FFT of stress field
4. correct average deformation gradient to fulfil stress BCs
5. determine correction to deformation gradient field to fulfil mechanical equilibrium
6. inverse FFT of deformation field
7. correct deformation gradient field.

The volume element has to satisfy static equilibrium and—when using the mixed variational formulation—strain compatibility, and the stress BCs must be fulfilled before the iterative scheme is stopped.

Convergence Criteria

A solution is accepted if the stress field is equilibrated, the deformation gradient field is compatible and both of them follow the prescribed macroscopic BCs.

To ensure the resulting stress field is in equilibrium, the root mean square (RMS) value of the divergence of the stress field is reduced below a prescribed tolerance. The corresponding equilibrium criterion reads:

$$\begin{aligned}\max\left(\varepsilon_{\mathrm{eq,rel}}\left|\left|\overline{\boldsymbol{P}}\right|\right|_{\max},\varepsilon_{\mathrm{eq,abs}}\right)/\mathrm{m} &\geq \mathrm{RMS}\Big(||\mathrm{Div}\,\boldsymbol{P}(\boldsymbol{x})||_2\Big)\\ &= \sqrt{\sum_{j=1}^{N}||\boldsymbol{P}(\boldsymbol{k}_j)\,i\,\boldsymbol{k}_j||_2{}^2/\,N^2},\end{aligned} \tag{2.67}$$

where $\varepsilon_{\mathrm{eq,rel}}$ and $\varepsilon_{\mathrm{eq,abs}}$ are the relative and absolute equilibrium tolerances.

Similarly, for discretisations of the mixed variational formulation the RMS value of the curl of the deformation gradient field is reduced below a prescribed tolerance. The following compatibility criterion ensures the deformation gradient field of the Lagrange multiplier field-based scheme and the polarisation field-based scheme is compatible:

$$\begin{aligned}\max\left(\varepsilon_{\mathrm{comp,rel}}\left|\left|\overline{\boldsymbol{F}}-\boldsymbol{I}\right|\right|_{\max},\varepsilon_{\mathrm{comp,abs}}\right)/\mathrm{m} &\geq \mathrm{RMS}\Big(||\mathrm{Curl}\,\boldsymbol{F}(\boldsymbol{x})||_{\mathrm{F}}\Big)\\ &= \sqrt{\sum_{j=1}^{N}||\boldsymbol{F}(\boldsymbol{k}_j)\times i\,\boldsymbol{k}_j||_{\mathrm{F}}{}^2/\,N^2},\end{aligned} \tag{2.68}$$

where $\varepsilon_{\mathrm{comp,rel}}$ and $\varepsilon_{\mathrm{comp,abs}}$ are the relative and absolute compatibility tolerances.

The fulfilment of complementary macroscopic deformation gradient and stress BCs is determined by

$$\begin{aligned}&\max\left(\varepsilon_{\mathrm{BC,rel}}\left|\left|\overline{\boldsymbol{P}}\right|\right|_{\max},\varepsilon_{\mathrm{BC,abs}}\right) \geq ||\Delta\boldsymbol{P}_{\mathrm{BC}}||_{\max}\\ &\qquad\text{where } \Delta P_{\mathrm{BC}ij} = \begin{cases} A_{ijkl}\left(F_{\mathrm{BC}}-\overline{F}\right)_{kl} & \text{if } F_{\mathrm{BC}ij} \text{ prescribed}\\ \left(P_{\mathrm{BC}}-\overline{P}\right)_{ij} & \text{if } P_{\mathrm{BC}ij} \text{ prescribed}\end{cases}\end{aligned} \tag{2.69}$$

and $\varepsilon_{\mathrm{BC,rel}}$ and $\varepsilon_{\mathrm{BC,abs}}$ are the relative and absolute BC tolerances.

The default tolerance values are $\varepsilon_{\mathrm{eq,rel}} = 5.0\times10^{-4}$, $\varepsilon_{\mathrm{eq,abs}} = 1.0\times10^{-10}\,\mathrm{Pa}$, $\varepsilon_{\mathrm{comp,rel}} = 5.0\times10^{-4}$, $\varepsilon_{\mathrm{comp,abs}} = 1.0\times10^{-10}$, $\varepsilon_{\mathrm{BC,rel}} = 1.0\times10^{-2}$, $\varepsilon_{\mathrm{BC,abs}} = 1.0\times10^{3}\,\mathrm{Pa}$. Unless otherwise specified, these values are used for the simulations presented in this work.

Equilibrium and compatibility in Fourier space

In eq. (2.67) and eq. (2.68), norms of static equilibrium (see eq. (2.27)) and strain compatibility (see eq. (2.19)) are computed in FOURIER space. Using the differentiation property $\mathcal{F}[df(x)/dx] = i2\pi k f(k)$, this is done in a computationally efficient way by combining the different spatial derivatives for curl and divergence according to their definition. Moreover, the RMS as a volume average is easily accessible as discussed in Eisenlohr et al. (2013) in FOURIER space.

2.3.3 Reconstruction of a Displacement Field from a Deformation Gradient Field

In the presented large strain framework, the displacement field—*i.e.* the vector field that maps each computation point from the reference into the deformed configuration (see section 2.1.1)—is not known. Therefore, it must be calculated in a post processing step for spatially resolved visualisation. For the data presented in this thesis this is done with a method proposed by Eisenlohr et al. (2013) that is briefly recapitulated here.

The proposed shape reconstruction algorithm is suitable to reconstruct the geometry of volume elements (VEs) with periodic BC and known deformation gradient field on a regular, three dimensional grid in undeformed configuration. Starting from the separation of the deformation gradient in average and fluctuating part (eq. (2.43)), the fluctuation in the displacement field can be recovered as

$$\begin{aligned}
\tilde{\boldsymbol{F}}(\boldsymbol{x}) &= \tilde{\boldsymbol{w}}(\boldsymbol{x}) \otimes \nabla \\
\tilde{\boldsymbol{F}}(\boldsymbol{k}) &= \tilde{\boldsymbol{w}}(\boldsymbol{k}) \otimes i\,\boldsymbol{k} \\
\tilde{\boldsymbol{F}}(\boldsymbol{k}) i\,\boldsymbol{k} &= \tilde{\boldsymbol{w}}(\boldsymbol{k})\,(i\,\boldsymbol{k} \cdot i\,\boldsymbol{k}) \\
-\tilde{\boldsymbol{F}}(\boldsymbol{k}) \frac{i\,\boldsymbol{k}}{|\boldsymbol{k}|^2} &= \tilde{\boldsymbol{w}}(\boldsymbol{k}) \quad \forall\, \boldsymbol{k} \neq \boldsymbol{0}.
\end{aligned} \tag{2.70}$$

Since the fluctuation, $\tilde{\boldsymbol{F}}$, of the deformation gradient has by definition a vanishing average, the exclusion of the zero-frequency vector $\boldsymbol{k} = \boldsymbol{0}$ in eq. (2.70) to prevent a division by zero is inconsequential. When inserting the result of eq. (2.70) into eq. (2.42) the overall deformation map can be assembled as

$$\boldsymbol{y}(\boldsymbol{x}) = \overline{\boldsymbol{F}}\boldsymbol{x} - \mathcal{F}^{-1}\left(\tilde{\boldsymbol{F}}(\boldsymbol{k}) \frac{i\,\boldsymbol{k}}{|\boldsymbol{k}|^2}\right), \tag{2.71}$$

i.e., integrating the locally fluctuating part of the deformation gradient in FOURIER space and the average part in real space. A beneficial side effect of this splitting is the possibility of independently re-scale the displacement fluctuation in the visualisation.

From eq. (2.71) the coordinates of the deformed grid are recovered. For a subsequent

visualisation hexahedral cells are constructed around these grid points. Each node of a cell is positioned at the average location of all eight surrounding grid points, accounting for periodicity.

For an evaluation of the reconstruction accuracy, benchmark results are presented by Eisenlohr et al. (2013).

2.3.4 Comparison to the Finite Element Method and Stability Benchmarks

To show the advantages of the spectral method, here results obtained by the basic variant of the spectral solver are compared to results obtained with a commercial FEM solver. Furthermore, the different spectral solver variants—*i.e.* the direct variational formulation, the LAGRANGE multiplier field-based scheme, and the polarisation field-based scheme—are benchmarked to each other in terms of stability. The examples nicely show, which detailed insights into polycrystal mechanics are enabled by high-resolution CP simulations. The geometries used for the simulations shown in this section are presented in fig. 2.3. In total, three geometries are used: a synthetic polycrystal consisting of 50 grains generated by a VORONOI tessellation, an elastic plate with a circular inclusion and a plastic plate with a circular inclusion divided into its quadrants.

Comparison to the Finite Element Method

As pointed out by Eisenlohr et al. (2013), DAMASK allows a comparison of different BVP solvers using exactly the same material point model. For the comparison of the

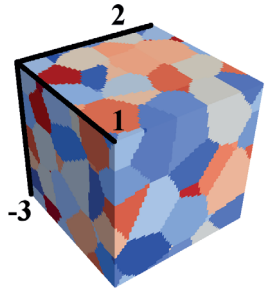

(a) Periodic VORONOI tessellation of 50 randomly placed seeds at grid resolution of 64^3. Each color represents one randomly chosen crystal orientation.

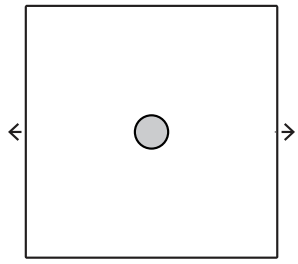

(b) Two-dimensional elastic plate with central circular inclusion. Arrows indicate horizontal extension direction.

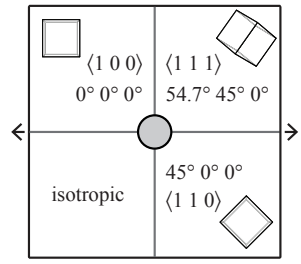

(c) Plastic plate with circular inclusion. Orientations are sketched as unit cells and given as crystallographic loading directions and EULER angles. Loading in uniaxial tension along horizontal arrows.

Figure 2.3: Geometries used to discuss the performance of the spectral solver.

original basic scheme formulation (*i.e.* equivalent to the direct variational formulation using the non-linear RICHARDSON solver) of the spectral method and the commercial FEM solver MSC.MARC in version 2010, the 3D microstructure shown in fig. 2.3a was deformed in pure shear in $2-3$-direction up to approximately 0.2. In the FEM model, a periodic displacement field is enforced by linking the degrees of freedom for matching nodes on opposite faces. The material parameters of the phenomenological material model are chosen to represent copper. Different tolerance criteria are set for both solvers and the tessellated structure was resolved with a 16^3, a 32^3, and a 64^3 grid for both solvers and additionally at 128^3 and 256^3 points for the spectral solver. For more details about material parameters, numerical settings, and loading conditions see Eisenlohr et al. (2013).

First, the macroscopic response, *i.e.* the stress–strain curve in loading direction is compared and discussed. From fig. 2.4 it can be seen that the FEM solutions (shown in red) show a much higher mesh dependence than the solutions obtained by the spectral method (shown in blue). In this figure, for both solution methods, mesh/grid resolution increases from light to dark and convergence tolerance decreases from dotted to dashed to solid line. Comparing the mesh dependence shows that essentially, the spectral method converges already at a grid of 32^3, while for the FEM no mesh convergence is observed for the examined meshes, where computation limits made higher mesh resolution infeasible. This example shows that the exponential convergence of the spectral method makes it attractive for the determination of average values, as at a low resolution—at least for single phase materials—the solution is already grid-converged. However, a more pronounced dependence on the convergence criterion is seen for the spectral method while the FEM is only slightly influenced (see inset in fig. 2.4).

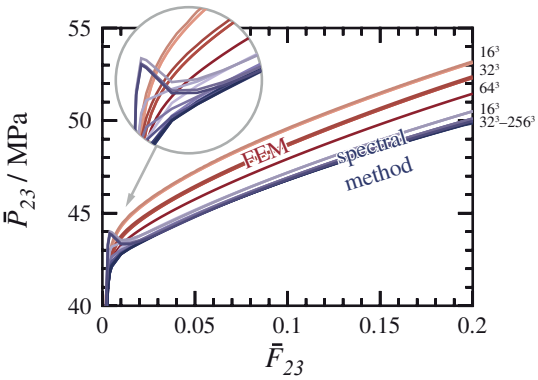

Figure 2.4: Stress–strain response of the polycrystal example shown in in fig. 2.3a.

Next, in fig. 2.5, the VON MISES equivalent strain ($\varepsilon_{\mathrm{v}M}$) and stress ($\sigma_{\mathrm{v}M}$) at the final applied shear strain along the $(0,0,0)-(1,1,1)$ diagonal of the grain aggregate is shown. The profiles resulting at different mesh/grid resolutions exhibit similar trends as already observed for the volume averaged mechanical response. Considering the equivalent strain the FEM results gradually approach, at increasing mesh resolution, the profile to which the spectral method appears to have converged already at a grid resolution of 64^3 for the local response. The strain profiles predicted by FEM are comparably smooth, while the spectral method solutions show considerably higher variability in grains and at grain boundaries. Relatively large amplitudes of high-frequency strain oscillations are found in the spectral solutions, particularly at some

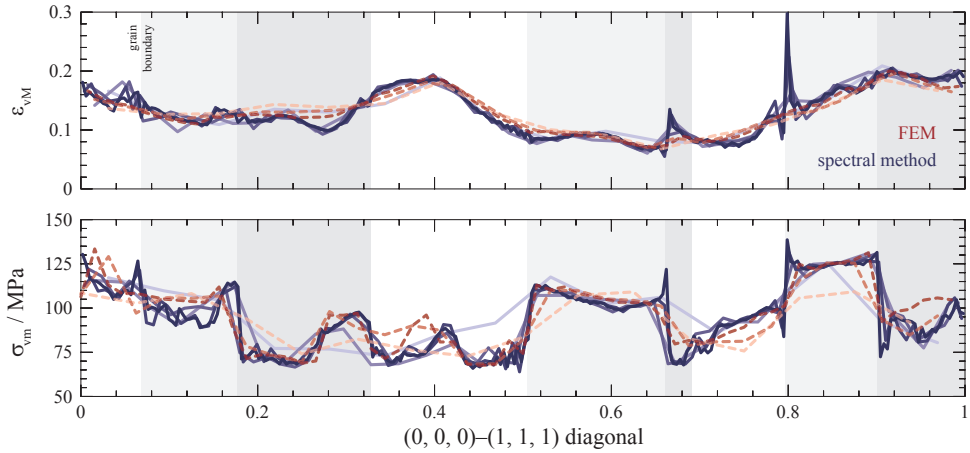

Figure 2.5: Equivalent strain and stress along a diagonal through the polycrystal example at approximately 0.2 shear strain.

grain boundaries. At most of the grain boundaries crossed by this particular diagonal, the converged spectral results reveal significant and sudden jumps in equivalent stress. This feature is also suggested by extrapolating the evolution of FEM profiles with mesh resolution, despite them not reaching the high fidelity of the spectral profiles that are obtainable with help of the trigonometric polynomials.

Finally, the stress field mapped onto the deformed configuration is shown in fig. 2.6. The trends that the spectral method converges faster with increasing resolution and shows a higher fidelity in the solution field already observed in figs. 2.4 and 2.5 can be confirmed by comparing the local response. With respect to the further use of the spectral method, *i.e.* the potential use of high-resolution CP simulations, the solution of the VE discretised at 256^3 points (lower right corner in fig. 2.6) is very promising. It can be obtained in roughly one week of computation time and shows highly resolved stress gradients inside single grains.

Comparison of Spectral Solver Variants

To benchmark the different variants of the spectral solver, the well-known Kirsch's plate (as shown in fig. 2.3b) was used. A square plate with unit dimensions containing a circular inclusion of area fraction 1.3 % is discretised into 2048×2048 grid points (fig. 2.3b). An isotropic elastic material model is used to describe the plate and the inclusion. The inclusion stiffness is scaled by factors in the range of 10^{-8} to 10^{4} relative to the plate stiffness and the plate is strained to 0.01 strain in horizontal direction. The solution, *i.e.* the Cauchy stress in horizontal loading direction, obtained at 10^{-4} (void) and 10^{3} (rigid) using the basic variational scheme and the non-linear GMRES solver is shown in fig. 2.7.

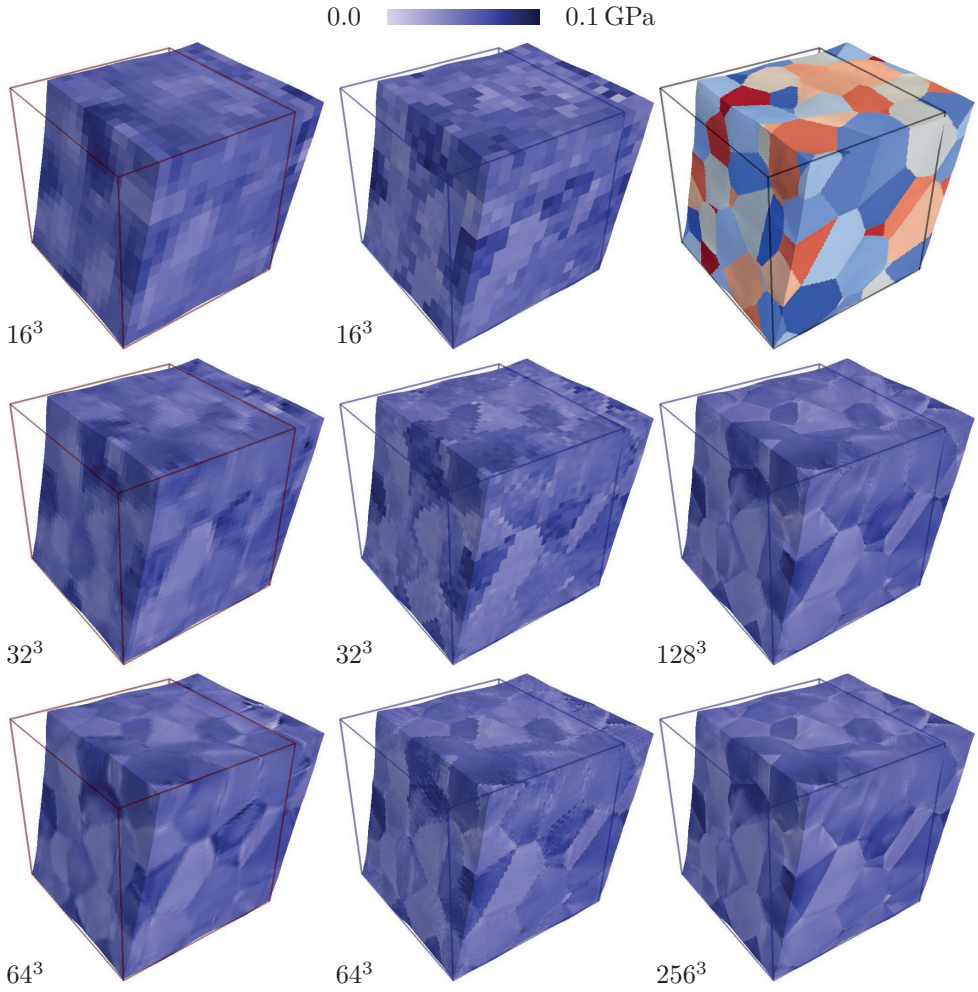

Figure 2.6: Piola–Kirchhoff stress at a shear strain of approximately 0.2 mapped onto the deformed configuration of the polycrystal example for FEM (red frame) and the spectral solver (blue frame) at all calculated resolutions.

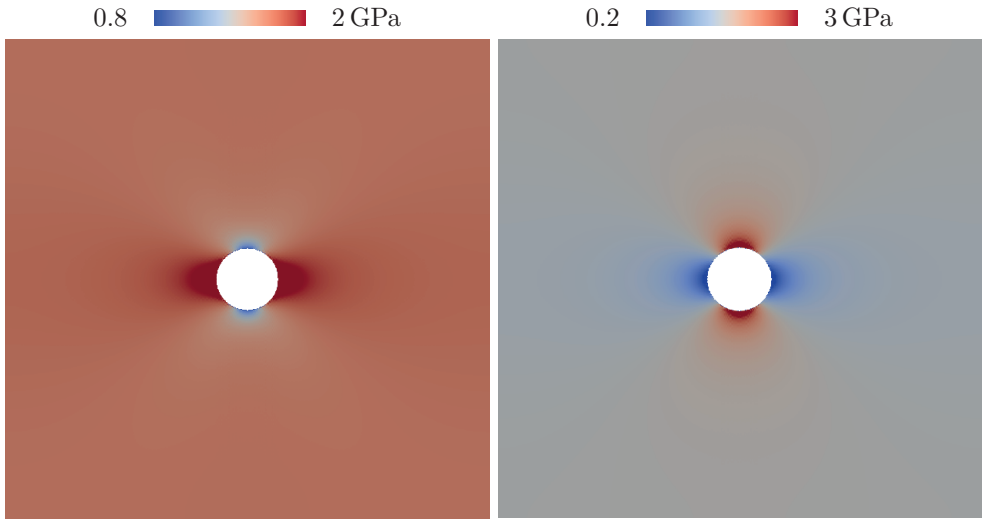

(a) Rigid inclusion. **(b)** Void inclusion.

Figure 2.7: CAUCHY stress in horizontal loading direction mapped on the elastic inclusion problem (fig. 2.3b) at the final strain of 0.01.

Figure 2.8 presents the number of residual evaluations required by the various spectral methods to solve for the applied uniaxial tensile deformation. An increase in the computational cost in relation to an increasing stiffness contrast of the inclusion is generally observed.

The least favorable convergence and stability is exhibited by the non-linear RICHARDSON method (fig. 2.8 top). In combination with the basic and the LAGRANGE multiplier field-based scheme, convergence within the specified iteration limit is only found for stiffness contrasts in the range $10^{-1,\dots,2}$. For the polarisation field-based scheme a wider stiffness contrast range $10^{-8,\dots,3}$ of convergence is seen. Consistent with the results of Monchiet et al. (2012), the polarisation field-based scheme results in an accelerated convergence compared to the basic scheme. Contrary to the results reported by Michel et al. (2001), the LAGRANGE multiplier field-based scheme exhibits worse convergence behaviour than the basic scheme.

Improved stability is achieved by using the inexact NEWTON-GMRES method (fig. 2.8 center). Here, the basic schemes converge over the entire range of stiffness contrasts and the mixed variational methods in the range $10^{-4,\dots,3}$.

The non-linear GMRES method exhibits the most favorable convergence and stability properties (fig. 2.8 bottom). All schemes require a roughly similar number of residual evaluations for given stiffness contrast. However, with decreasing stiffness contrast of the void inclusion the performance of theLAGRANGE multiplier field-based scheme gradually worsens up to a factor of about 10 relative to the other three schemes.

For all schemes that converged within the prescribed iteration limit for the case of a

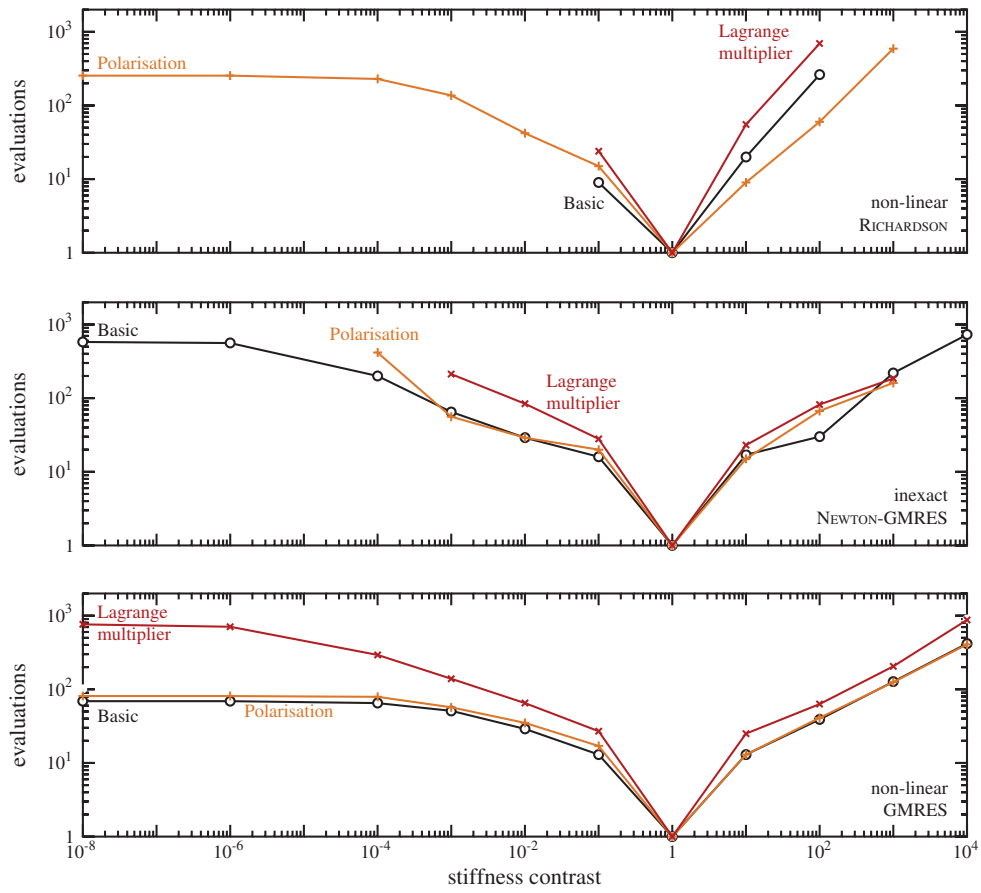

Figure 2.8: Number of residual evaluations required to solve the elastic inclusion problem as a function of stiffness contrast.

void inclusion (left side of fig. 2.8) a saturation in the number of residual evaluations with increasing contrast is observed—indicating the existence of a finite bound for the zero-stiffness case. This is in contrast to the unbounded behaviour of the conventional fixed-point solution schemes as discussed in Michel et al. (2001). Furthermore, for rigid inclusions (right side of fig. 2.8), the computational cost of the non-linear GMRES and inexact NEWTON-GMRES grows only with an exponent of about 0.5 with increasing stiffness contrast compared to an exponent of close to 1.0 seen for the non-linear RICHARDSON method. While the inexact NEWTON-GMRES method results in a larger number of residual evaluations, the error is reduced super-linearly per iteration compared to the non-linear GMRES and non-linear RICHARDSON which exhibit linear convergence rates (Kelley, 1995).

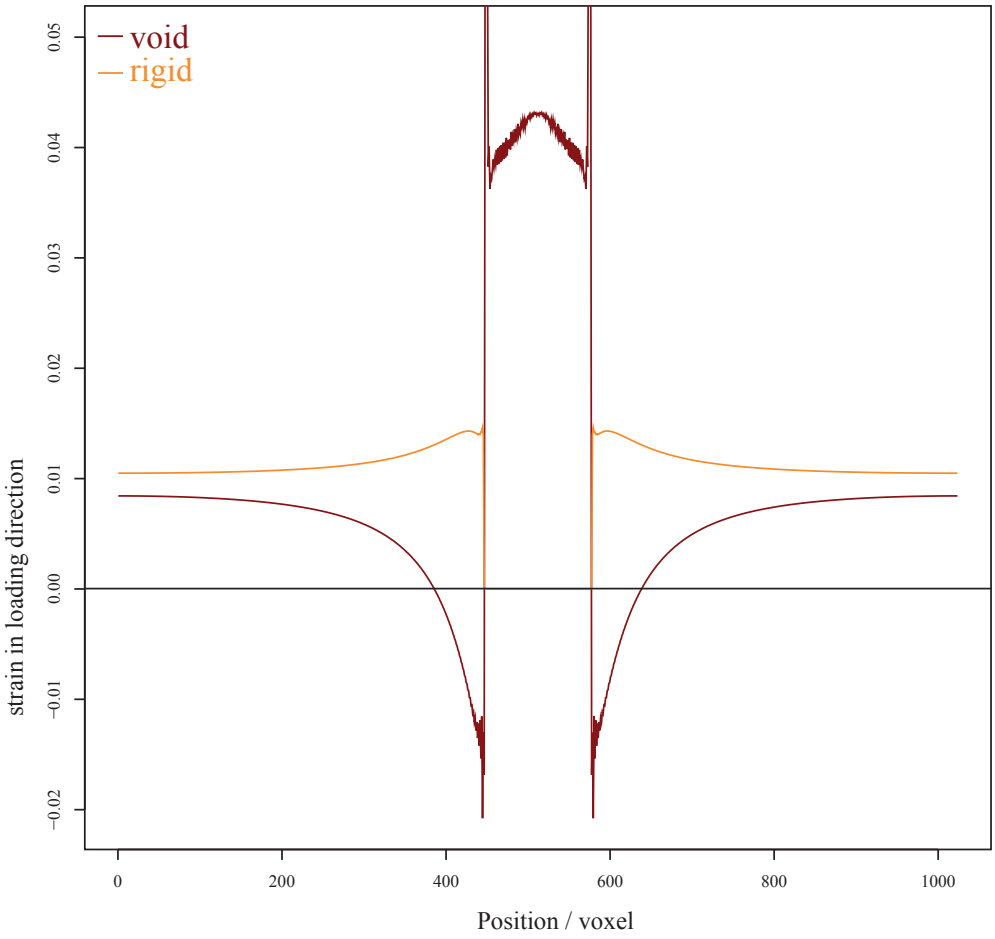

Figure 2.9: Logarithmic strain in horizontal loading direction shown along the horizontal center for the elastic inclusion problem.

The approximation of the solution with trigonometric polynomials raises the problem of GIBBS phenomenon. GIBBS phenomenon is the name given to the fact that approximation by FOURIER series "overshoots" at steep gradients. This is exemplarily shown on the results of the elastic plate, like in fig. 2.7 for a phase contrast of 10^{-4} (void) and 10^{3} (rigid). The horizontal strain profile along the middle of the plate in fig. 2.9 clearly shows oscillations in the vicinity of the jump in stiffness. However, since the property contrasts for simulation set-ups closer to reality are much lower, this issue is not further examined yet. Still, for the planned incorporation of damage mechanics into DAMASK, it has to be addressed to avoid damage related softening due to numerical artefacts at grain or phase boundaries.

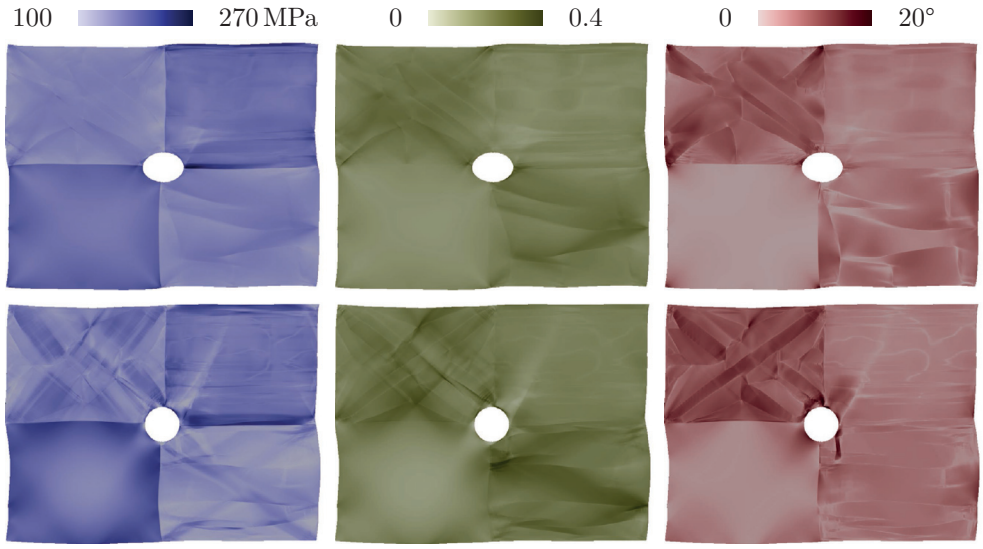

(a) Equivalent stress σ_{vM}. **(b)** Equivalent strain $\varepsilon_{\mathrm{vM}}$. **(c)** Rotation angle between initial and current grain orientation.

Figure 2.10: Field quantities at a strain of 0.2 in horizontal loading direction mapped onto the deformed configuration of the simplified polycrystal with void (top) and with rigid (bottom) inclusion (stiffness contrast 0.01 and 100).

As a last example, a square plate with unit dimensions containing a circular inclusion of area fraction 1.3 % divided into four quadrants as shown in fig. 2.3c and discretised into 1024×1024 grid points is presented here. The fcc-materials in three quadrants have distinct orientations and are described by a phenomenological crystal plasticity model, while the remaining lower left quadrant is described by the isotropic material model commensurate with the behaviour a non-textured polycrystal composed of these distinct crystalline orientations. As reported by Shanthraj et al. (2015), the non-linearities introduced by the far more complex material behaviour compared to the simulation of the elastic plate, decrease stability and convergence rate. Instead of discussing the limits of the spectral solver variants in detail here, some of the field quantities obtained by the simulation at a strain of 0.2 are shown in fig. 2.10. Even a quick visual inspection shows how complex strain and stress distribution develops in the presence of various complex materials and it becomes obvious that high-resolution is necessary to capture the evolving gradients.

3 Simulations

The various aspects of the simulations conducted in this study are presented here. Each series of simulations aims at a specific question which can be answered with the help of high-resolution crystal plasticity (CP) simulations. Hence, first the reason for performing the simulations is given. The outline of the aims is followed by a summary of the model details, *e.g.* used constitutive model, input parameters, and microstructure details. Finally, the conclusions that can be drawn from the results are presented.

The studies are categorised into the following two modelling approaches,

1. section 3.1 "*Real Microstructures*"
2. section 3.2 "*Artificial Microstructures*",

with both of them having their specific advantages and drawbacks.

Using microstructure models based on real microstructures is a widely used approach (Karlsson et al., 1974; Maresca et al., 2014; Raabe et al., 2001; Reuber et al., 2014) that enables a direct comparison to experimental results and allows studying the full variety of experimentally observable microstructural features present in real materials. The spectral method based solver allows a direct takeover of the experimentally obtained data on regular grids, *i.e.* from pixel (2D) or voxel (3D) based datasets into the simulation set-up The high authenticity of the model is a huge advantage of using real microstructures. Differences of the model geometry to the experimentally observed microstructure are only caused by experimental limitations. However, obtaining spatially fine resolved data is extremely challenging, especially when dealing with 3D microstructures. Moreover, there are two additional major drawbacks associated with the use of real microstructures: First, resolving all measured microstructural features requires a high resolution associated with high computational costs. This leads to the situation that simulations of real microstructures—including all details—are often done on microstructural parts that are not large enough to be representative for the material, and, hence, the average behaviour cannot be deducted from these simulations. As outlined before, the performant spectral solver used in conjunction with plain material models can tackle also this second challenge as it enables the use of large, but still highly resolved microstructures. Second, using existing microstructures as the basis for simulations limits the microstructural parameters space to materials that can already be produced. Hence, thought experiments are limited to changing constitutive parameters and boundary conditions on models that are created from experimental data.

To overcome the limitations associated with the use of real microstructures, artificial microstructures can be created. Having full control over the microstructure parameters used allows investigating easily the influence of isolated features. As an additional advantage, the parameter space is not limited to existing microstructures. Grain shape and size distribution can be chosen from a range that is only depending on the available tools for the microstructure generation. The models are usually much simpler than realistic microstructures and capture only some dominant geometrical features, where the incorporated details depend on the aim of the study. Actually, often microstructures are designed in an idealised way to avoid the variety of microstructural features and heterogeneities in real microstructures. This especially holds when only the average response of a material under investigation is of interest and a structure representative for the material called a representative volume element (RVE) is used. Still, it must be ensured that the same response—with respect to selected parameters—as for the real material is obtained. Usually, periodic boundary conditions (BCs) are enforced in all directions on the RVE expanding the volume to infinity and avoid that boundaries influence the behaviour. As outlined in section 2.3, periodic BCs are inherent to the employed solution technique.

3.1 Real Microstructures

In the two studies on "*Strain and Stress Partitioning* in *Dual Phase Steel*" and "*Strain Localisation in Magnesium*" presented in this thesis, the experimental data used as the model input is obtained using electronic backscatter diffraction (EBSD) measurements. EBSD is a surface measurement technique, and obtaining a 3D dataset is only possible by a destructive serial sectioning approach. Since a close coupling between experimental results and simulations is required in the context of the conducted studies, the destruction of the undeformed microstructures must be avoided. Therefore, *pre-mortem* measurements are conducted only on the surface, which especially means that 2D simulations are conducted. The implications of this approach are in detail discussed in "*Strain and Stress Partitioning* in *Dual Phase Steel*", but equally hold for "*Strain Localisation in Magnesium*". As shown later, the strong coupling between experiments and simulations allows for a deeper understanding of the microstructure physics and is preferred over a more realistic 3D simulation with missing experimental results for validation.

3.1.1 Strain and Stress Partitioning in Dual Phase Steel

Dual phase (DP) steels consists mainly of two phases, a softer ferritic matrix with hard martensitic inclusions for simultaneous improvement of strength and ductility. They find a wide field of applications due to their excellent mechanical properties (Tasan et al., 2015). Despite the successful application of DP steels and a large number of works on modelling the mechanical behaviour of DP steels, a full understanding of the local stress and strain partitioning that is responsible for the mechanical properties, is

still not achieved.

The high degree of interest on DP micro-mechanical simulations is coming from (i) the demand coming from industrial application, and (ii) the fact that the challenges in modelling DP steels—stemming from the high phase contrast and the crystalline nature of both phases—render DP steels a perfect benchmark in modelling complex materials regarding simulation stability, prediction quality, etc. Current, CP based simulation techniques enable to investigate strain and stress partitioning effects at the micro-scale (Chen et al., 2014; Ghassemi-Armaki et al., 2014; Ramazani et al., 2014) with the target to improve DP microstructures with respect to specific properties like higher yield strength or improved ductility for given minimum yield strength. The presented work is—in line with these recent simulation approaches—aiming at a strong coupling between experiment and simulation. More results related to micro-mechanical simulations of DP steels are given in Tasan et al. (2014a,b) which provide the basis for the work—especially the experimental characterisation and the joint numerical-experimental investigation—presented here.

Purpose of the first series of simulations is the quantification of the size needed of a microstructural patch to be representative. Determination of the minimum RVE size is of great importance to limit the computational costs when predicting average quantities, *e.g.* in the determination of yield surfaces. A closer look on the local stress and strain partitioning is the focus of the second simulation study. The comparison to experimental data obtained by *in-situ* experiments performed at the microstructure used for the simulation allows analysing sub-surface effects, the main drawback of using 2D microstructures. A sensitivity study on the martensite properties helps to quantify the effect of martensite yield strength in alloy design.

Experimental Preparation and Characterisation

The DP steel used in this study was provided by Tata Steel (IJmuiden, Netherlands). Two different grades where used, one having an initial yield strength of 600 MPa (subsequently called DP600) and one of 800 MPa (subsequently called DP800). However, to get a coarser microstructure, both samples were subjected to a second laboratory-scale heat-treatment cycle following spark erosion to cut microstructure samples. Specimen surfaces are polished with colloidal SiO_2 particles ranging from 0.01 µm to 0.05 µm in size, followed by a conventional metallographic grinding, diamond-polishing, and etching procedure.

For studying the effect of the microstructure patch size on the average response, an EBSD scan of 1618 × 1155 points with a step size of 0.087 µm was conducted on the DP600 material shown in fig. 3.2. The EBSD measurements are carried out using a Zeiss-Crossbeam XB 1540 focused ion beam (FIB)-scanning electron microscopy (SEM) instrument (Oberkochen, Germany). Each computation point is assigned an initial crystallographic orientation and a phase (*i.e.* martensite or ferrite, based on the grain average image quality (IQ), see fig. 3.1).

For the coupled experimental–numerical approach, preliminary large field-of-view EBSD measurements are conducted to identify region of interests (ROIs) in the DP800

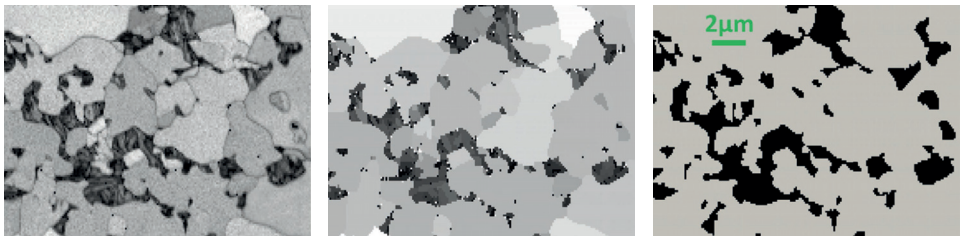

(a) EBSD-based IQ map. **(b)** Grain average IQ. **(c)** Phase distribution from grain average IQ.

Figure 3.1: Generation of a DP microstructure model from the EBSD-based IQ map. Darker areas represent worse IQ and indicate martensite.

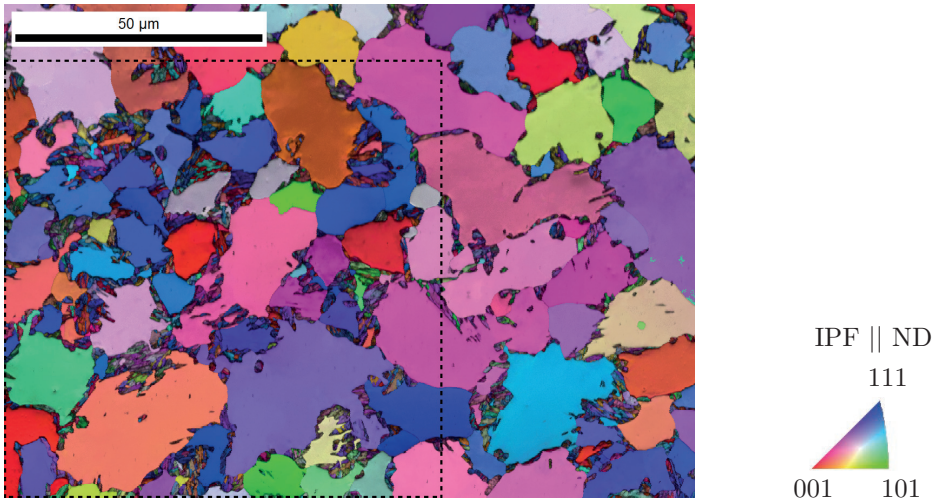

Figure 3.2: EBSD based orientation and IQ map (darker areas indicate lower IQ) of the DP600 microstructure. The dashed line indicates an area of 1024 × 1024 pixel of the full 1618 × 1155 pixel microstructure map.

microstructure that enable an investigation of the influence of different microstructural features on strain partitioning (fig. 3.3a). Out of these, tensile samples with gauge dimensions of 4 mm × 2 mm × 1 mm are produced by spark erosion. The EBSD data obtained on the investigated microstructural areas (fig. 3.3a) is set as the starting point for the CP simulations using the same SEM instrument and the same technique as for the DP600. Prior to the deformation experiments, a single layer of $0.015 \pm 0.005 \mu$m SiO_2 particles is homogeneously distributed on the sample surfaces for follow-up local strain field measurements. Using a Kammrath & Weiss GmbH (Dortmund, Germany) stage, the tensile sample is deformed in uniaxial tension to increasing levels of strain. At each deformation level, ROIs are imaged using different detectors in

SEM (*i.e.* secondary electron (SE), backscatter electron (BSE), inlens SE, EBSD). For optimal image correlation conditions and microstructure imaging, low-voltage imaging conditions are employed to get a small interaction volume. The images captured by the inlens SE detector are used for the microscopic digital image correlation (μDIC) analysis using the ARAMIS software (GOM GmbH, Braunschweig, Germany). Imaging of the surface topography is done by SE detector and the underlying microstructure is analysed by BSE imaging. As shown in fig. 3.3, the single layer pattern of SiO_2 particles offers two evident advantages: On the one hand, it does not obstruct SE and BSE imaging as demonstrated in fig. 3.3b, thus allowing microstructure and surface imaging without any interference from the overlaying pattern. On the other hand, the SiO_2 pattern can be selectively imaged for follow-up μDIC at high resolution without any disturbance by the underlying microstructure (thus avoiding effects of surface roughening and/or changing electron channelling conditions) by inlens SE imaging as shown in fig. 3.3c. Following the deformation experiments, a colloidal SiO_2 polishing based serial sectioning procedure is carried out to reveal the 3D microstructure underneath the observed surface layer.

Digital Image Correlation

Digital image correlation techniques are used to track changes in images. For images captured with an (electron) microscope, the approach is termed "microscopic digital image correlation" (μDIC) Commonly, digital image correlation (DIC) relies on the maximisation of a correlation coefficient for each pixel of two subsequently taken images. This allows deriving the (2D) strain fields at the surface during deformation of a microstructure. Different approaches (*e.g.* place markers or etch the microstructure) exist to increase uniqueness and contrast to enable an improved correlation finding, however they usually either affect the microstructure integrity or limit the view on the surface. The approach by Yan et al. (2015) used here has neither of these disadvantages, as the pattern on top of the microstructure is only visible in the inlens SE detector while it is "invisible" in the other imaging modes.

Modelling Details

The phenomenological material model is used to model both phases, ferrite and martensite. However—despite the term "dual phase"—some retained austenite (face-centered cubic (fcc) phase of steel) is often found in the microstructures (Tasan et al., 2015). Since it is known from experimental observations that the austenite transforms to martensite at early deformation states in the considered material and phase transformation is not (yet) included in Düsseldorf advanced material simulation kit (DAMASK), austenitic grains are treated as martensite.

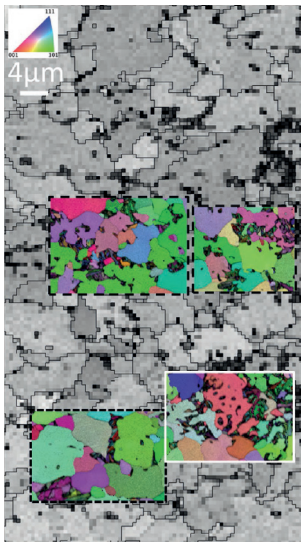

(a) EBSD-based IQ map that shows the ROI's locations with high-resolution IPF overlays. The ROI with the solid white border is discussed in detail.

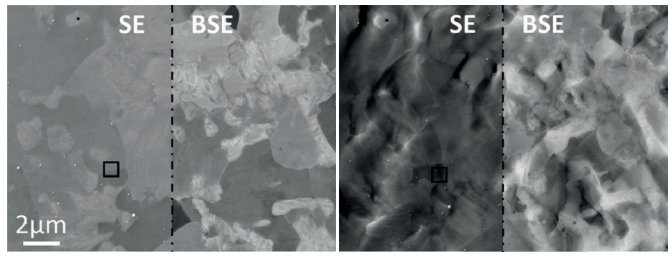

(b) BSE/SE microstructure images at the undeformed state (left) and at $\bar{\varepsilon}_x = 0.08$ strain in horizontal loading direction (right).

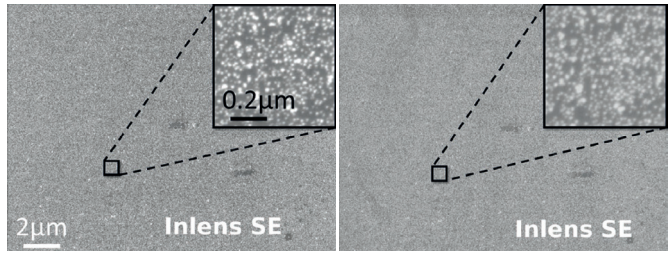

(c) Inlens SE microstructure images at undeformed state (left) and at $\bar{\varepsilon}_x = 0.08$ strain in horizontal loading direction (right). High magnification insets show that microstructure-free pattern images are obtained by the inlens detector.

Figure 3.3: Methodology of ROI selection and microstructure imaging during the deformation experiments on the DP800. Note that all images in figs. 3.3b and 3.3c are of exactly the same ROI, underlining the strength of the developed selective pattern imaging methodology.

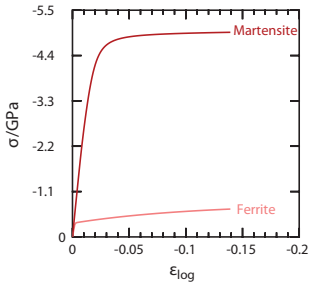

Figure 3.4: Stress–strain curve of martensite and ferrite for the DP600 simulations.

For the statistical analysis performed on the DP600 microstructure, two simulations have been performed: One on a 1024^2 sized subset of the patch shown in fig. 3.2 that allows simple down sampling by factors of two, and one on the whole microstructure (having a resolution of 1618×1155 pixel). Since the exact constitutive behaviour is of minor importance, the crystal structure is assumed to be body-centered cubic (bcc) with 12 slip systems of the $\langle 1\,1\,1\rangle\{1\,1\,0\}$ family for martensite and ferrite and CP data obtained from stress–strain curves of a similar material is used. The stress–strain curves of both phases resulting from uniaxial compression are shown in fig. 3.4. Both samples are deformed in uniaxial tension (along the horizontal direction in figs. 3.6 and 3.7)

at a rate of $6.0 \times 10^{-4}\,\mathrm{s}^{-1}$.

For the coupled experimental–numerical study, the same strain rate as in the experiment, namely, $6.0 \times 10^{-4}\,\mathrm{s}^{-1}$ is applied to microstructural patches under tensile-strain for 170 s, *i.e.* until a final average strain of approximately $\bar{\varepsilon}_{\mathrm{x}} = 0.08$ is reached. The out-of-plane direction of the 2D model is set to be stress-free on average to reflect the experimental situation of a free surface. As it is characteristic for the spectral method, the microstructure is periodically repeated in all three directions, *i.e.* the prescribed BCs are volume/area averages. It will be shown later that the strain heterogeneity is influenced mainly by the immediate neighbourhood of a given microstructural area, suggesting that the influence due to the artificial periodicity introduced by the boundary description is confined to a narrow zone (Tasan et al., 2014b). Nevertheless, to minimize this deviation further the simulated microstructural areas are kept larger than those tracked experimentally. The errors introduced through the mentioned uncertainties in phase determination and through the setting of phase properties are critically discussed in section 3.1.1.

Parameter Identification for the Coupled Experimental–Numerical Study Additional authenticity is introduced into the model by extracting the phase properties directly from the microstructure (see figs. 3.5a to 3.5c). This is done with the help of an inverse CP finite element method (FEM) simulation procedure which was originally developed for and applied to hexagonal materials (Yang et al., 2011; Zambaldi et al., 2010, 2012). It is here applied to the case of bcc crystal structure of ferrite. This approach to identify the mechanical behaviour of the ferrite matrix phase involves optimisation of initial and final resolved shear stress on the $\langle 1\,1\,1\rangle\{1\,1\,0\}$ and $\langle 1\,1\,1\rangle\{1\,1\,2\}$ slip system families[1] in four differently oriented grains (fig. 3.5b) to correctly predict the pile-up topography resulting from nano indentation experiments (fig. 3.5a). To achieve this, load-controlled indentation experiments ($f_{\max} = 4.0\,\mathrm{mN}$) are performed using a spheroconical diamond tip with a nominal tip radius of 1.0 µm and a nominal cone angle of 90° on the same undeformed DP microstructure (away from the ROIs). From the array of indents, those in the center of differently oriented, large ferrite grains are selected (shown as highlighted grains in fig. 3.5a). Thus, grain boundary effects on indentation measurements, and surface relief effects on follow-up atomic force microscopy (AFM) measurements are both minimised. The pile-up topography in the vicinity of the indents (10 µm × 10 µm) are measured using tapping mode AFM measurements with a scan rate of 0.25 Hz and a tip velocity of $5\,\mu\mathrm{m\,s}^{-1}$. Finally, using a Nelder-Mead type non-linear optimisation algorithm, the initial and saturation shear strength values for the two slip system families are identified. The objective function is based on differences in pile-up topographies (fig. 3.5b) and the load–displacement curves. The identified set of parameters is given in table 3.2a and shown in comparison to the

1 For coupled experimental–numerical study, $\langle 1\,1\,1\rangle\{1\,1\,2\}$ systems have been additionally introduced. The parameter identification procedure should predict high resistances for them if they are not needed to reproduce the experimental results.

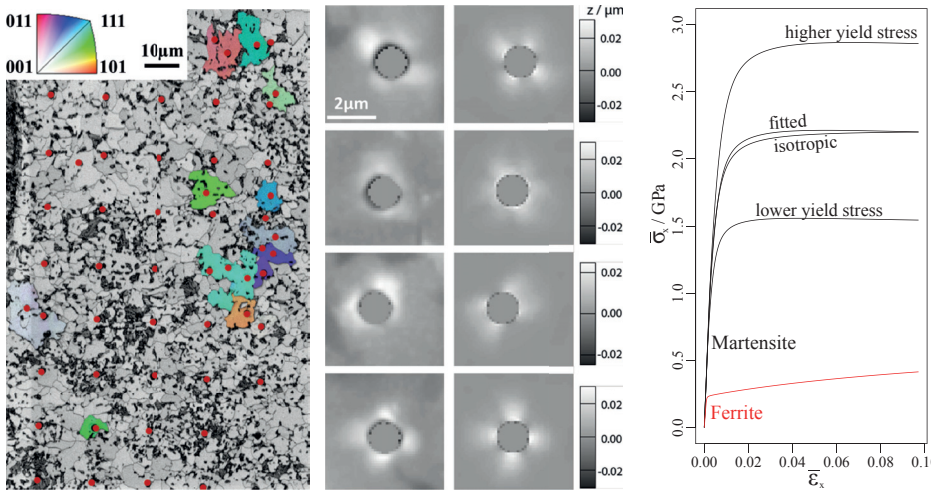

(a) Location of all indents in the selected microstructure. IPF parallel to normal direction shown in inset.

(b) AFM measured pile-up topography of the indents (left) and simulated topographies (right).

(c) Determined ferrite phase behaviour and the different martensite behaviours considered.

Figure 3.5: Ferrite phase properties extraction from nano indentation experiments: Grid of indents in DP microstructure fig. 3.5a, pile-up topography fig. 3.5b and simulated stress–strain curves fig. 3.5c.

martensite stress–strain curves in fig. 3.5c. Using the DAMASK framework allows using for both, the simulation of the DP microstructure with the fast and efficient spectral solver, as well as for the parameter identification—where complex geometries not accessible to the spectral solver are required—with the commercial FEM solver MSC.Marc, exactly the same material point model.

As shown in fig. 3.5b for the four chosen grains, the final CPFEM predicted pile-up patterns are in good agreement with the AFM based experimental measurements. This indicates that the hardening behaviour is correctly described by the determined set of parameters. However, as the approach described in Zambaldi et al. (2012) does not strongly penalize deviations from the load–displacement curve, the force is underestimated by the simulation and reaches only values of approximately $f_{\max} = 2.5\,\mathrm{mN}$ instead of the experimentally determined $f_{\max} = 4.0\,\mathrm{mN}$ (for the same indentation depth).

The same procedure is not applicable to the martensitic phase, as the dimensions of the martensitic laths are of similar size as the nano indents. Therefore, for the martensite, constitutive parameters are fitted to the macroscopic behaviour, *i.e.* polycrystal stress–strain curves, of a similar martensitic material. To strengthen the correlation with the martensite found in the considered DP steel, the initial flow stress

ratio between ferrite and martensite (identified from the nano indentation experiments) is considered. This ratio is used as the basis to scale the initial and final shear resistance on each slip system family in the martensite. The resulting parameters are given in table 3.2b. Additionally, the sensitivity of the simulation results on the martensitic phase properties is studied with the aid of follow-up simulations using modified mechanical contrast between ferrite and martensite. For that, martensite variations are introduced by $\pm 25\,\%$ scaling of the initial and final shear stress on each slip system family. Also, the influence of martensite anisotropy is investigated by comparing the results of anisotropic CP simulations to results obtained using the isotropic material model for the martensite. The stress–strain curves in uniaxial tension for the various martensite parameters are shown in fig. 3.5c in comparison to the response of the ferrite.

Table 3.1: Material parameters for DP800. Based on Tjahjanto et al. (2008) and fitted for the simulation of DP steel presented in Roters et al. (2012).

(a) Ferrite, initial and saturation slip resistance determined using inverse simulation procedure.

Property	Value	Unit
C_{11}	233.3×10^9	Pa
C_{12}	235.5×10^9	Pa
C_{44}	128.0×10^9	Pa
$\dot{\gamma}_0$	1.0×10^{-3}	$\mathrm{m\,s^{-1}}$
$\xi_{0,\{1\,1\,0\}}$	95.0×10^6	Pa
$\xi_{\infty,\{1\,1\,0\}}$	222.0×10^6	Pa
$\xi_{0,\{1\,1\,2\}}$	96.0×10^6	Pa
$\xi_{\infty,\{1\,1\,2\}}$	412.0×10^6	Pa
$h_{0,slipslip}$	1.0×10^9	Pa
$h_{\alpha\beta}$	1.0	
n	20.0	
a	2.25	

(b) Martensite, initial and saturation slip resistance fitted to stress–strain curve and hardness ratio.

Property	Value	Unit
C_{11}	417.4×10^9	Pa
C_{12}	242.4×10^9	Pa
C_{44}	211.1×10^9	Pa
$\dot{\gamma}_0$	1.0×10^{-3}	$\mathrm{m\,s^{-1}}$
$\xi_{0,\{1\,1\,0\}}$	406.0×10^6	Pa
$\xi_{\infty,\{1\,1\,0\}}$	873.0×10^6	Pa
$\xi_{0,\{1\,1\,2\}}$	457.0×10^6	Pa
$\xi_{\infty,\{1\,1\,2\}}$	971.0×10^6	Pa
$h_{0,slipslip}$	563.0×10^9	Pa
$h_{\alpha\beta}$	1.0	
n	20.0	
a	2.25	

Results and Discussion

In the following, the results of the simulations are presented and discussed. First, the results of the solely simulation-based study on the effects of the microstructure patch size on the average response are given. Second, the results of the coupled experimental–numerical approach are depicted.

Statistical Analysis of Stress and Strain Partitioning The distribution of the equivalent stress shown in fig. 3.6a confirms the expected inhomogeneous stress partitioning in DP steels. While the martensite regions can bear a stress much higher than the average

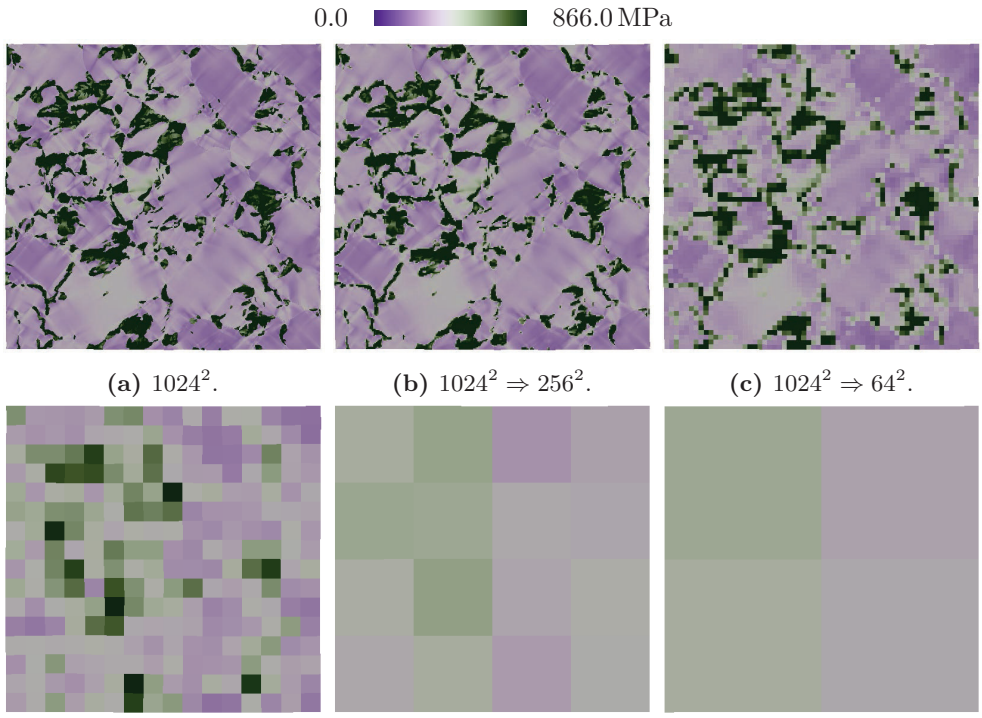

(a) 1024^2. **(b)** $1024^2 \Rightarrow 256^2$. **(c)** $1024^2 \Rightarrow 64^2$.

(d) $1024^2 \Rightarrow 16^2$. **(e)** $1024^2 \Rightarrow 4^2$. **(f)** $1024^2 \Rightarrow 2^2$.

Figure 3.6: Equivalent stress at 1.5 % strain in horizontal loading direction averaged over differently sized square regions of a 1024^2 pixel microstructure shown in fig. 3.2. Central color represents average of the whole patch.

of the whole microstructure, stress in most of the ferritic grains is below the average. Additionally, a dependence of the stress distribution on crystallographic orientation in ferritic grains can be seen. However, the inhomogeneous stress distribution caused by martensitic grains at the phase boundaries usually penetrates into the center of the ferritic grains, only weakly affected by their crystallographic orientation. This leads to steep stress gradients, an effect which is naturally more pronounced in small ferritic grains that lie in regions with relatively high martensite volume/area fraction. The stress partitioning in martensite also depends on orientation and the neighbourhood: The connected network of martensite in the upper left regions exhibits a rather large stress. However, individual orientations lead to a visible partitioning within individual grains. Most of the small, angular shaped martensitic grains that are distributed all over the microstructure show a stress clearly below the average load in martensite.

The subsequent merging and averaging of individual computation points into larger areas in figs. 3.6b to 3.6f shows, how sensitive the averaged response is on the local microstructure: Even the four quarters of the investigate microstructure do not show

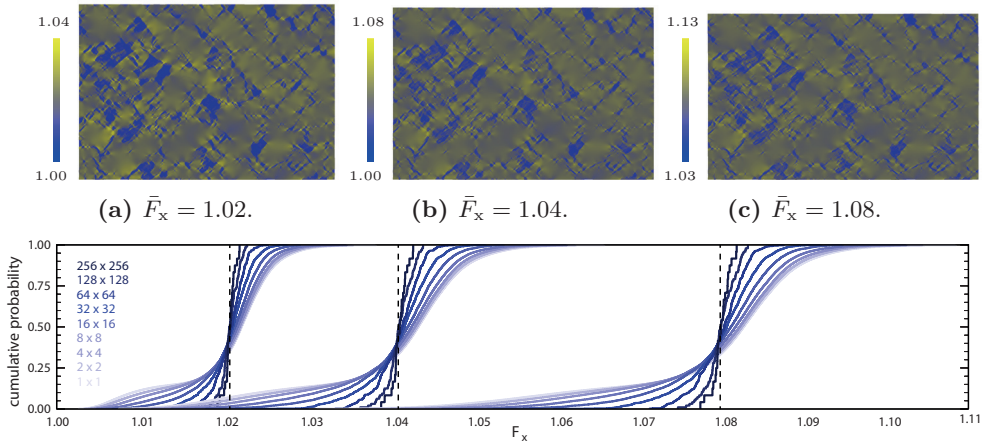

(a) $\bar{F}_{\mathrm{x}} = 1.02$. **(b)** $\bar{F}_{\mathrm{x}} = 1.04$. **(c)** $\bar{F}_{\mathrm{x}} = 1.08$.

(d) Cumulative probability of F_{x} for $\bar{F}_{\mathrm{x}} = 1.02$,1.04, and 1.079. The square size varies from 1×1 to 256×256.

Figure 3.7: Deformation gradient F_{x} in horizontal loading direction at different deformation levels of a 1618×1154 patch. With increasing deformation, the spread in the local deformation grows.

the same stress response as the whole patch, despite the fact that they contain all more than approximately 25 individual ferrite grains. This clearly shows that a statistically RVE for a given DP steel grade cannot be based on a small microstructural patch only, especially since the microstructure varies significantly within a single sheet (Peranio et al., 2012).

The results presented in fig. 3.7 show the evolution of the strain distribution with increasing applied strain, where in figs. 3.7a to 3.7c the local distribution is shown and in fig. 3.7d the averaged response over patches of increasing size is given. In contrast to the results in fig. 3.6, the full microstructure is investigated. This particularly means that averaging into larger block sizes (fig. 3.7d) introduces some inaccuracy because some points are taken into account twice when averaging over the border to the periodically repeated points. Two important conclusions can be drawn from this figure: (i) the spatial strain distribution is to a large extend constant over time, and (ii) the absolute spread between lower and higher strain is increasing with increasing total strain level.

In summary, the microstructure inhomogeneities and the strong phase contrast present in DP steels require the use of rather large microstructural patches to capture the average response of a given material. Therefore, a fast solution method as the spectral solver is especially favorable for the determination of average quantities like yield surfaces and stress–strain curves. It should also be mentioned that the 2D simulations tend to exaggerate the effect, as *e.g.* a soft ferritic grain is not supported

by sub-surface martensite and vice versa. A detailed investigation on the effects of subsequent slicing of a 3D volume element to estimate the errors introduced in strain and stress partitioning on DP steels is presented in subsection 3.2.2 "*Subsurface Effects in Simplified Dual Phase Steel*" and Diehl et al. (2015).

Coupled Experimental–Numerical Study As already outlined, the microstructure shown in fig. 3.3a is investigated experimentally and by CP simulations. Hence, first a comparison of both results is presented here followed by a detailed discussion of the observed stress and strain partitioning. The comparison and the discussion are based and follow closely Tasan et al. (2014b).

Comparing the overall strain distributions obtained from the experiments (fig. 3.8b) to those from the simulations (fig. 3.9a) reveals that many features are in good agreement, especially:

- A strong strain partitioning is observed among ferrite and martensite (compare *e.g.* rightmost images in figs. 3.8b and 3.9a). A more quantitative analysis, given in fig. 3.10, shows that in the simulated results the ferrite grains accommodate most of the deformation, *i.e.* $\bar{\varepsilon}_{\mathrm{vM}} = 0.12 \pm 0.09$ at an average deformation of $\bar{\varepsilon}_{\mathrm{vM}} = 0.10$ compared to $\varepsilon_{\mathrm{vM}} = 0.02 \pm 0.01$ in martensite. These values correspond well to the experimentally observed strong partitioning shown in the same graph.
- There is also good qualitative agreement in the level of scatter observed in the ferritic regions. A large scatter ($\varepsilon_{\mathrm{vM}} = 0.020 - 0.35$ for a nominal strain of $\varepsilon_{\mathrm{vM}} = 0.010$) corresponds to the highly heterogeneous nature of strain distribution in ferrite, which is clearly seen in fig. 3.8b and fig. 3.9a.
- The strain in many ferritic regions is localised in bands oriented at 45° to 50° w.r.t. the loading direction in both experiment and simulation.

These observations indicate that the model is suitable to describe the overall mechanical behaviour correctly. However, there are some differences between simulation and experiments regarding the exact location of some of the high strain bands. The possible reasons of these differences are discussed later on.

Given the good correlation of the strain distribution between simulation and experiment, von Mises stress maps obtained from simulations (fig. 3.9b) are considered to represent the correct stress partitioning in the microstructure during the *in-situ* experiments. For further discussion, the undeformed microstructural image is subdivided into four regions, termed (i), (ii), (iii), and (iv) (see fig. 3.8b). As already observed in fig. 3.6a, it can be seen that long and thin martensite connections aligned with the loading direction experience the highest stress while smaller, globular shaped martensite areas show rather small stresses. The observation from fig. 3.7 that strain partitioning is spatially constant is confirmed here for the stress: The local stress peaks up at these points right away with the start of straining. Already at $\bar{\varepsilon}_{\mathrm{vM}} = 0.03$, the stress distribution in martensite is very heterogeneous and the pattern is kept with increasing deformation. Notch effects arising from morphological irregularities also

contribute to the high stresses observed in the martensitic areas. Stress heterogeneity is also observed in martensitic regions where morphology or geometrical orientation do not seem to play a significant role (see, *e.g.* the large martensite grains in region (iii)). It is thus clear that the stress in martensite depends on the crystallographic orientation of each martensitit block (Morito et al., 2003), although this does not reflect to a significant difference in strain within such large martensitic regions.

The influence of martensite constitutive properties on the stress partitioning is presented in fig. 3.11. Here it is clearly seen that the martensite accommodates most of the stress in the microstructure independently of its exact constitutive behaviour. Martensite has an equivalent stress of $\sigma_{\mathrm{vM}} = 1.0 - 4.0\,\mathrm{MPa}$ compared to $\sigma_{\mathrm{vM}} = 0.1 - 1.0\,\mathrm{MPa}$ in the ferrite. Two trends are evident: (i) for the martensite with the lower yield stress shown in fig. 3.11c, the stress distribution within the martensitic regions is more homogeneous compared to the case with higher martensite yield stress values (fig. 3.11d). (ii) Stress heterogeneity in martensite is significantly decreased when the martensite behaviour is assumed to be isotropic (compare fig. 3.11a with fig. 3.11b). However, the overall strain partitioning and the stress distribution in ferrite is not significantly influenced by the constitutive parameters of the martensite. This explains, why the experimental and and simulated results are in good agreement, even though the martensite constitutive behaviour is not known as exactly as the ferrite properties.

The results presented above demonstrate the vast amount of reliable simulated micro-mechanical data that can complement the experimental findings. Hence, the

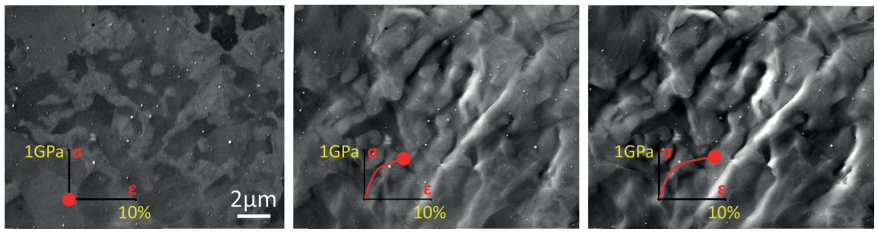

(a) SE images. Global stress strain curves are provided as insets.

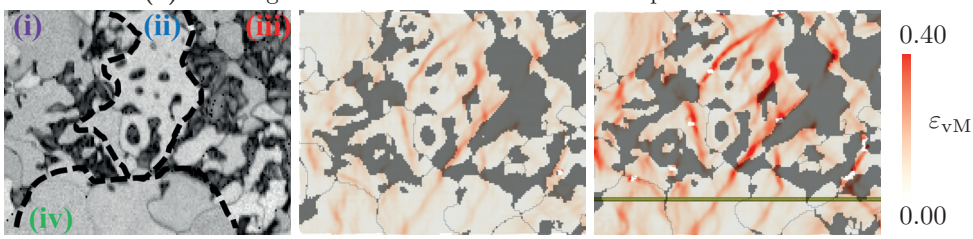

(b) μDIC strain maps.

Figure 3.8: Results of the *in-situ* deformation experiments in the undeformed state (left) and at an average strain of $\bar{\varepsilon}_{\mathrm{x}} = 0.05$ (center) and $\bar{\varepsilon}_{\mathrm{x}} = 0.08$ (right).

obtained results allow a discussion regarding the validity of the observed DP micromechanics and the gained understanding that enables to develop guidelines for the development of microstructures tailored to desired properties.

The overall success in capturing the similar qualitative (see fig. 3.8b and fig. 3.9a) and quantitative (see fig. 3.10) strain distribution trends in simulations and experiments strongly underlines the correctness of the presented simulation results. However, differences are observed in some cases as well, for example regarding the position of the highly strained bands. More specifically, the simulations reveal strain bands that are following narrow ferritic zones in regions with higher martensite content (*e.g.* regions (ii) and (iii)), whereas in ferritic regions that are more remote from martensite islands (*e.g.* in region (iv)), the strain distribution is smoother compared to the experimental results. The causes of these deviations are discussed in the following paragraphs, and tracked to known limitations of the experimental methodology or to the underlying simplifications in the simulation methodology.

The main limitation for the experiments is that SEM is a surface analysis technique and cannot (at least in a non-destructive manner) be used to reveal 3D information of the investigated microstructure. This inevitably introduces the columnar microstructure in the DP simulation model, while in reality there may be martensite layers below the surface ferrite grains, or vice versa (see also subsection 3.2.2 "*Subsurface Effects in Simplified Dual Phase Steel*" and Diehl et al., 2015). However, as shown in Tasan et al. (2014a), a *post-mortem* serial sectioning methodology allows assessing the role of the underlying microstructure in a critical manner and can partially compensate the difficulties associated with the 2D modelling approach. An example is discussed regarding region (iii), where a significant difference is observed between experiments and simulations (rightmost images in figs. 3.8b and 3.9a). The simulations predict a

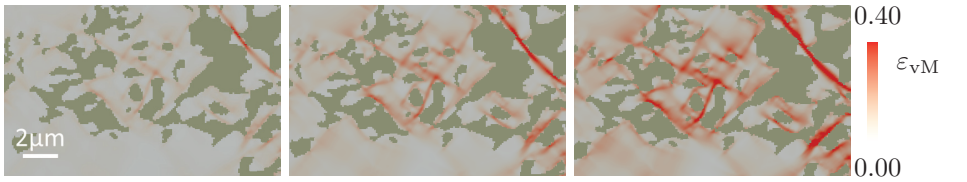

(a) von Mises strain in ferrite. Gray areas indicate martensite.

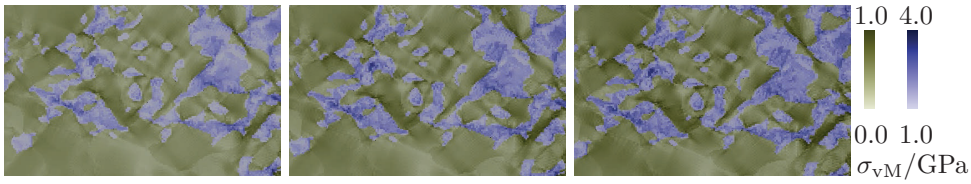

(b) von Mises stress in ferrite and martensite.

Figure 3.9: Results obtained from the CP simulations at an average strain of $\bar{\varepsilon}_x = 0.03$ (left), $\bar{\varepsilon}_x = 0.05$ (center) and $\bar{\varepsilon}_x = 0.08$ (right).

strain band running throughout the gap between two large martensite grains, while in the experiments such a pronounced strain band is not present, and the strain is much more localised at the narrowest opening between the two martensite grains. Closer inspection of the rightmost image in fig. 3.8a reveals that this latter localisation point is a continuation of a strain band from region (ii) that penetrates the large martensite grain. The serial sectioning data presented by Tasan et al. (2014a) reveals that this large martensite grain is considerably thinner in the z-direction with respect to other martensitic regions in the patch. Thus, the strain band approaching from region (ii) can easily penetrate these large (but thin) martensite regions and cause the unexpected strain localisation. This observation obviously cannot be captured in the simulations where the particular martensite grain—like all other grains—is considered columnar. Nevertheless, given that only one of the considered four regions has a significantly different subsurface structure (*i.e.* region (iv)), the overall influence of the subsurface microstructure is observed to be limited in the given case. A more generalised discussion on subsurface effects on surface observations is given in section 3.2.2.

For the simulations, incorporating effects of (currently not implemented) phenomena such as pre-hardening due to transformation-induced geometrically necessary dislocation (GND) and damage modelling are also important for improving the prediction of the micro-mechanical behaviour of DP steels. Most obvious examples for the former are observed through the hard response of small ferritic grains with high initial GND density (Calcagnotto et al., 2011) that is created during processing due to the different thermal (expansion) properties of ferrite and martensite. Even though it is clear that the local strain distribution is most strongly dependent on the distribution heterogeneity of martensite (see the strain levels in the identified regions in the leftmost image in fig. 3.8b), the experimental results show that the strain distribution in ferrite is also highly heterogeneous. Sharp deformation bands nucleate at ferrite

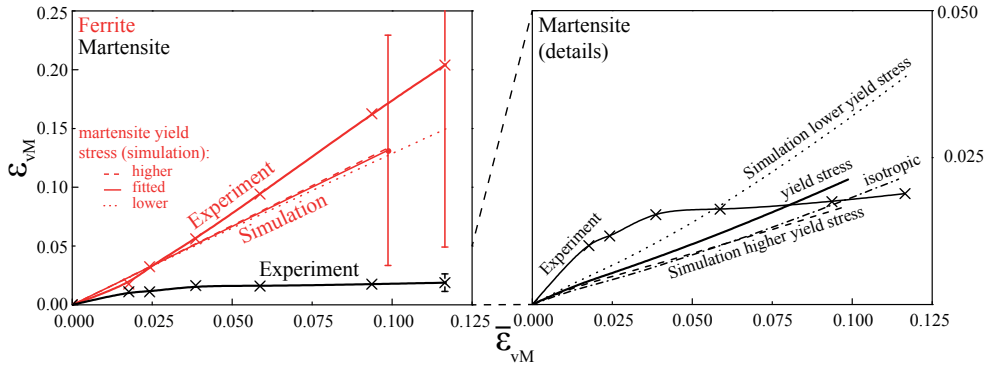

Figure 3.10: Quantitative analysis of strain partitioning between ferrite and martensite evaluated from the experiments (averaged over 50 μDIC data points per phase) and the simulations (averaged over all data points) for ferrite and martensite.

grain interiors, and then propagate along the softest routes with 45° to 50° inclination to the loading direction, even in regions with little or no martensite (*i.e.* region (iv)). This experimental observation of the strong heterogeneity of strain distribution within the ferritic grains (fig. 3.8b) suggests that pre-straining effects may play a significant role, and, therefore, should be taken into account in future simulations.

An example for a damage incident *i.e.* the micro-cracking observed at comparatively low strain levels in a narrow martensite section surrounded by ferrite is given in Tasan et al. (2014a). In the simulation, high hydrostatic stress can be seen in the vicinity of this damage incident and it is assumed that this is a general phenomenon that plays a significant role in the plasticity of martensite (and the surrounding ferrite). Since most martensite grains have irregular geometries that lead to stress concentrations, early damage nucleation is assumed to take place frequently. However, at these low strain levels where damage nucleates, the surrounding ferrite is not yet fully hardened, and thus can successfully arrest these micro-cracks, also effectively dispersing the stress concentration in the process. This effect is believed to be the reason of the discrepancy between results of experiments and simulations observed for martensite plasticity at early strain levels (fig. 3.10). Softening due to damage in both phases will assumably lead to a re-distribution of strain in the microstructure. Incorporating damage mechanics is therefore—in conjunction with the use of 3D microstructures—the most important future modelling task that is assumed to improve the prediction quality more than a refined plasticity model can do.

In summary, the integrated experimental–numerical methodology presented here is able to capture many of the quantitative aspects such as strain and stress partitioning in a realistic way. Further authenticity can be implemented, and a significantly improved quantitative–qualitative agreement can most likely be achieved when advanced material models including damage mechanics are used and if 3D effects could be successfully taken into account. As discussed later on, probably taking either a 3D microstructure or damage modelling into account is not sufficient. Due to the close interconnection of 3D effects and strain localisation, both limitations need to be expelled together (see also section 3.2.2).

A number of interesting observations regarding DP steel micro-mechanics can be made: As shown in the strain maps fig. 3.8b, the deformation in ferrite is significantly localised. That is, in many ferritic grains high strain gradients can be found. This observation is in contrast to some of the earlier works with limited spatial resolution (*e.g.* by Tasan et al., 2010), where more homogeneous strain distributions in ferrite grains were recorded. This underlines that the strain partitioning process in martensite–ferrite microstructures is more complex than assumed for a simple hard–soft composite material. The soft ferrite phase here has processing-inherited in-grain microstructural heterogeneity, which leads to an in-grain strain partitioning. Ghassemi-Armaki et al. (2013) found similar mechanical heterogeneity when doing micro pillar compression experiments in ferritic grains. Various causes can be proposed for such heterogeneity, *e.g.* dislocation density gradients due to transformation-induced GNDs, transformation-induced residual stresses, ferrite grain size heterogeneity, etc., all leading to the same micro-mechanical behaviour: The deformation of the relatively harder shell of a given

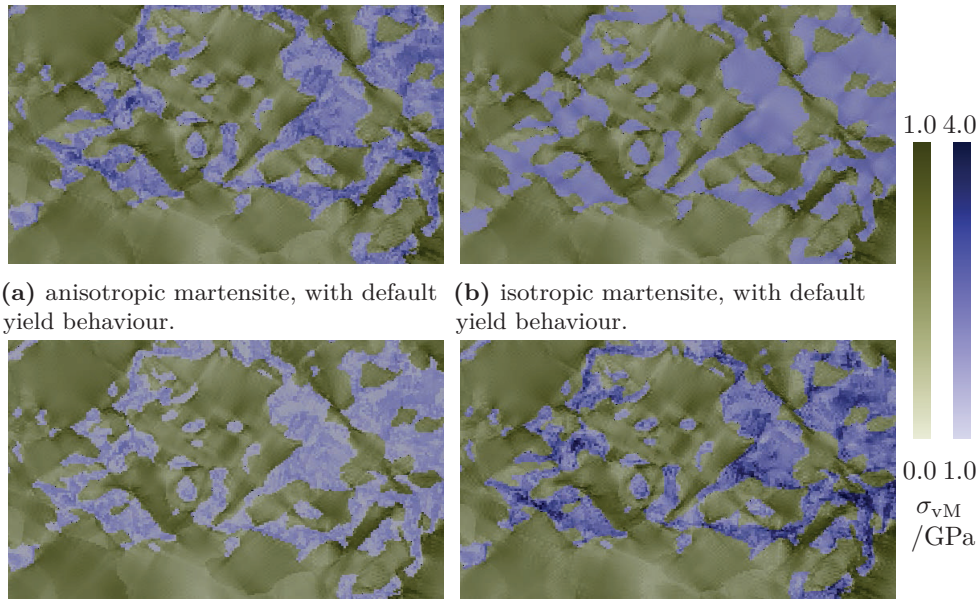

(a) anisotropic martensite, with default yield behaviour.

(b) isotropic martensite, with default yield behaviour.

(c) anisotropic martensite with lower yield stress values.

(d) anisotropic martensite with higher yield stress values.

Figure 3.11: VON MISES stress distribution for differently modelled martensite constitutive response (table 3.2b) at an average strain of $\bar{\varepsilon}_{\mathrm{x}} = 0.08$.

ferritic grain is further constrained due to the surrounding hard martensite, forcing the ferritic center to accommodate most of the deformation in sharp strain bands. From an alloy design point of view, this result suggests that the ferrite properties are as important as those of the martensite in the design of DP steels with tailored mechanical behaviour.

The early and time-wise almost constant stress and strain partitioning might lead to damage nucleation, preferentially at martensitic sites (figs. 3.9b and 3.10). Since the CP simulations suggest that the shape of the martensite and its local alignment with respect to the loading direction do play a direct role (fig. 3.9b), controlling the shape of the martensite seems a promising way to hamper early damage. This analysis is supported by experimental reports that show that high martensite plasticity and damage resistance can be achieved when the martensite morphology is spherical (Calcagnotto et al., 2011).

Simulations with different martensite behaviour reveal another interesting observation regarding the micro-mechanics of DP steels (see fig. 3.11, as well as fig. 3.10): Apparently, the behaviour of the martensite has only a small influence on the stress–strain partitioning in the microstructure. Alteration of martensite properties has only a pronounced effect in the heterogeneity of stress distribution inside the martensitic regions (fig. 3.11). For example, for the harder martensite shown in fig. 3.11d, relatively

higher stress levels are observed within the narrow zones aligned parallel to the loading direction, compared to small, isolated martensitic islands. This observation again clearly underlines the importance of martensite shape and morphology in DP steel micro-mechanics. Thus, avoiding early damage nucleation in martensite, especially when martensite carbon content is high, requires avoiding morphological irregularities to avoid stress intensification effects.

3.1.2 Strain Localisation in Magnesium

The results presented here are contributions to a joint experimental–numerical investigation by Wang et al. (2014) on Magnesium (Mg) and closely follow this study. Mg and its alloys have received great attention for potential use in light weight structures because with a mass density of $1740\,\mathrm{kg\,m^{-3}}$ Mg is the lightest structural metal. However, the application of materials with hexagonal (hex) crystal structure is restricted by their poor formability and wrought Mg alloys develop strong basal-type textures during processing at room temperature caused by the lack of available deformation mechanisms (Yoo, 1981). Basal slip—typical for hex materials—and tension twinning are the primary deformation modes observed at room temperature in Mg. Both are easy to activate and their critical resolved shear stress (CRSS) could be determined in single crystal experiments by Akhtar et al. (1969) to be in the range of a few MPa. Slip on the basal systems leads to a grain-reorientation, such that the basal planes are closely aligned with the main material flow direction. This limits the contribution of the basal slip system to further deformation and hence, fracture is observed a comparably low strain levels (Gottstein et al., 2005; Humphreys et al., 2004).

Twinning allows strain along the crystal c-axis, providing additional degrees of freedom matching the requirement for five independent shear systems in the classical Taylor–Bishop–Hill sense (Agnew et al., 2001; Bishop et al., 1951). As outlined in section 2.2.2 twinning is—in comparison to slip—of unidirectional nature; *i.e.* a twin system is limited in its contribution to arbitrary shape changes. This further restriction of available deformation mechanisms explains the limited ductility of Mg. However, investigation of grain scale mechanics by Raabe et al. (2001) have shown that the Taylor–Bishop–Hill criterion must not be fulfilled at the local grain scale, since collective deformation of grain clusters can in certain cases provide a sufficient number of shear degrees of freedom for compatible polycrystalline deformation (Zhao et al., 2008). In room temperature deformation of Mg, these plastic heterogeneities and strain localisations are typically observed in the form of shear bands. Shear banding in Mg is a mesoscopic "grain-cluster" deformation process where the grains inside the shear band are reported to subsequently re-orient in the macroscopic shear direction, *i.e.* "soften" the sheared region with respect to further basal dislocation slip during continuing deformation (Barnett et al., 2004; Chun et al., 2012; Ion et al., 1982). The mechanisms associated with such shear band formation in Mg alloys are not well understood and are focus of current research (Chun et al., 2012; Hazeli et al., 2013; Kim et al., 2012; Scott et al., 2013). Shear band formation mechanisms are also the target in the presented experimental–numerical analysis following Wang et al. (2014).

In Wang et al. (2014), the activation of plastic heterogeneities such as shear bands and the effects of the local stress state on tension twinning with specific regard to grain-to-grain interactions and collective grain mechanisms were experimentally investigated on pure Mg and three different Mg-alloys. CP simulations are conducted to gain more quantitative insights into strain partitioning, local micro-mechanical stress states and the associated slip system activity, and the mechanisms leading to shear band formation during deformation. The data obtained by the simulations supplements the experimental findings, *e.g.* knowing the local stress state instead of assuming it to follow the applied load. In the presented example different scenarios for the applied BCs allow doing virtual experiments that are not feasible in *in-situ* experiments.

Experimental Preparation and Characterisation

The pure Mg was melted and solidified by induction in a steel crucible under Argon (Ar) pressure (1500 kPa). Homogenisation annealing of the as-cast materials was performed for 24 h at 450 °C under Ar atmosphere followed by water quenching. The material was hot rolled at 500 °C to a total engineering thickness reduction of 50 %, imposing 8 % to 10 % reduction per pass. Subsequent recrystallisation annealing was carried out at 350 °C under Ar atmosphere for 30 min again followed by water quenching.

The *in-situ* specimens were cut via spark erosion to a size of 5 µm × 2 µm × 3 µm (longitudinal direction × compression direction × transverse direction). Perpendicular to the compression direction, the observation plane (transverse direction) was mechanically ground followed by electro-polishing using the AC2 electrolyte (Struers GmbH, Willich, Germany). Prior to compression the grain orientations were measured by EBSD for the CP model. Displacement controlled *in-situ* compression experiments were carried out with approx. 0.002 mm displacement per compression step (corresponding to 1 % strain). The samples were kept under load in the compression stage throughout the measurements, hence, microstructure relaxation was minimised. Compression was continued until a maximum total strain of approximately 5 %, when increased surface roughness produced by slip traces and twins after higher deformation inhibits further SEM analysis. The microstructure evolution and active deformation carriers (dislocations, twins) during *in-situ* compression tests were tracked using EBSD and electron channelling contrast imaging (ECCI) on a Zeiss 1540XB Crossbeam FIB-SEM instrument at an acceleration voltage of 15 kV. Identification of active deformation systems was conducted by trace analysis in the ECCI images combined with orientation data from EBSD.

Modelling Details

The orientation information from the EBSD measurements of the undeformed ROI shown in fig. 3.12b is taken as the initial configuration for the CP simulation. Twinning is introduced for the six first-order tension twins (T1) according to the concept outlined in Kalidindi (1998) into the phenomenological material model. The following slip and twin systems are incorporated: three basal ($\{0\,0\,0\,1\}\langle 2\,\bar{1}\,\bar{1}\,0\rangle$), three first-order

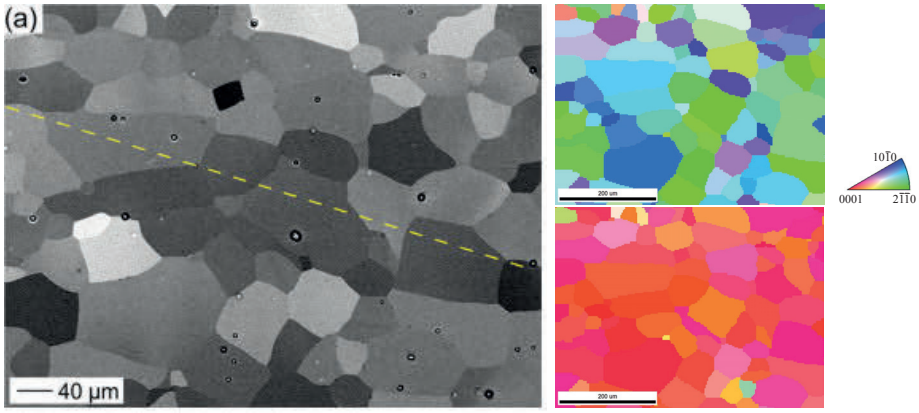

(a) ECC image.

(b) EBSD lattice orientation images (Top: || to transverse direction. Bottom: || to compression direction).

Figure 3.12: Initial Mg microstructures images. Vertical direction is compression direction.

Table 3.3: Material parameters for Mg, based on Tromans (2011) and Agnew et al. (2006).

(a) Elastic properties.

Property	Value	Unit
C_{11}	59.3×10^9	Pa
C_{33}	61.5×10^9	Pa
C_{44}	16.4×10^9	Pa
C_{12}	25.7×10^9	Pa
C_{13}	21.4×10^9	Pa
c/a	1.6235	

(b) Dislocation slip.

Property	Value	Unit
$\xi_{0,\text{basal}}$	10.0×10^6	Pa
$\xi_{\infty,\text{basal}}$	40.0×10^6	Pa
$\xi_{0,\text{prism}}$	55.0×10^6	Pa
$\xi_{\infty,\text{prism}}$	135.0×10^6	Pa
$\xi_{0,\text{pyr(a)}}$	60.0×10^6	Pa
$\xi_{\infty,\text{pyr(a)}}$	150.0×10^6	Pa
$\xi_{0,\text{pyr(c+a)}}$	60.0×10^6	Pa
$\xi_{\infty,\text{pyr(c+a)}}$	150.0×10^6	Pa
$h_{0,\text{slipslip}}$	500.0×10^6	Pa
$h_{0,\text{sliptwin}}$	0.0×10^6	Pa

(c) Twinning.

Property	Value	Unit
$\xi_{0,\text{T1}}$	40.0×10^6	Pa
$h_{0,\text{twintwin}}$	50.0×10^6	Pa
$h_{0,\text{twinslip}}$	150.0×10^6	Pa

prismatic $\langle a \rangle (\{0\,1\,\bar{1}\,0\}\langle 2\,\bar{1}\,\bar{1}\,0\rangle)$ six first-order pyramidal $\langle a \rangle (\{0\,1\,\bar{1}\,1\}\ \langle 2\,\bar{1}\,\bar{1}\,0\rangle)$, and six second-order pyramidal $\langle c + a \rangle (\{2\,1\,1\,2\}\langle 2\,\bar{1}\,\bar{1}\,3\rangle)$. Following Tromans (2011) and Agnew et al. (2006) the parameters to model the constitutive response are given in table 3.3. Like in the experiments, a quasi-static compression loading at $1.0 \times 10^{-3}\,\mathrm{s}^{-1}$ is applied to the microstructural patch until a final average strain of approximately $\bar{\varepsilon}_{22} = 0.05$ is reached. Since the local deformation state inside a sample of macroscopic dimensions can profoundly differ from the macroscopic BCs (Gutierrez-Urrutia et al., 2013; Raabe et al., 2001), the microstructure is loaded with four different BCs in order to understand the effect of the loading conditions on the evolution of an experimentally observed shear band.

In a first simulation run, plane strain compression (F_{11}, *i.e.* longitudinal direction, adjusted such that this direction is stress free on average, *i.e.* $P_{11} = 0$) without allowing in-plane and out-of plane shear is applied. These simulation conditions are macroscopically equivalent to the deformation state in the sheet center layer of industrially rolled material or—when translated into laboratory scale—channel die compression conditions. In a second CP simulation, plane strain compression allowing in-plane shear in the image plane (F_{12} additionally adjusted such that $P_{12} = 0$) was applied, mimicking a rolling-type loading situation where macroscopic thickness reduction is applied and shear is admitted. The third simulation was performed applying plane strain compression and allowing out-of-plane deformation normal to the image plane (F_{33} additionally adjusted such that $P_{33} = 0$). In order to further analyse the impact of shear stress, a fourth CP simulation was performed imposing compression loading and allowing additional out-of-plane shear (F_{12}, F_{13}, F_{23}, and F_{33} additionally adjusted such that $P_{12} = P_{13} = P_{23} = P_{33} = 0$).

The imposed boundary conditions at the end of the loading in terms of the deformation gradient $\boldsymbol{F}$ are as follows:

$$\boldsymbol{F}_1 = \begin{bmatrix} * & 0.0 & 0.0 \\ 0.0 & 0.95 & 0.0 \\ 0.0 & 0.0 & 1.0 \end{bmatrix} \qquad \boldsymbol{F}_2 = \begin{bmatrix} * & * & 0.0 \\ 0.0 & 0.95 & 0.0 \\ 0.0 & 0.0 & 1.0 \end{bmatrix}$$

$$\boldsymbol{F}_3 = \begin{bmatrix} * & 0.0 & 0.0 \\ 0.0 & 0.95 & 0.0 \\ 0.0 & 0.0 & * \end{bmatrix} \qquad \boldsymbol{F}_4 = \begin{bmatrix} * & * & * \\ 0.0 & 0.95 & * \\ 0.0 & 0.0 & * \end{bmatrix}$$

Where the "$*$" indicates that this component of the deformation gradient is adjusted as outlined in section 2.3.2 such that the corresponding component of the 1st Piola–Kirchhoff stress $\boldsymbol{P}$ equals to 0.0.

Results and Discussion

Pure Mg exhibits a strong basal-type recrystallisation texture (Gottstein et al., 2005; Humphreys et al., 2004), *i.e.* most grains adopt an orientation with a low Schmid -factor for basal slip and tension twinning systems with respect to plane strain boundary conditions. As outlined before, in this case a collective deformation of grain

clusters can accommodate for the missing degrees of freedom according to the Taylor–Bishop–Hill criterion. The macroscopic shear band observed during the *in-situ* compression (fig. 3.13) is a result of such a collaborative grain cluster deformation.

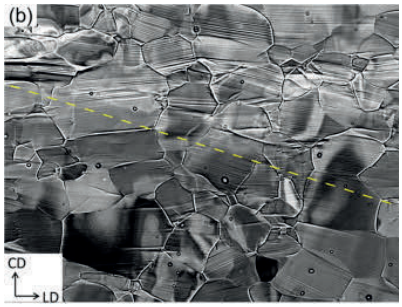

Figure 3.13: ECC microstructure image at 0.05 compressive strain in vertical loading direction.

Since no compression or Experimentally, the formation of the shear band was observed to start in conjunction with massive basal slip traces and tension twins are formed only after the third deformation step. secondary twins were observed, the formation of the shear band can be attributed to concentrated basal slip activity. The crystal orientations of the grains inside the shear band and in the non-shear-banded areas in pure Mg were investigated by Wang et al. (2014). The grains away from the shear band have basal orientations while the grains in the region where the shear band formed have their basal poles about 5° to 10° deviated from the compression direction, creating a slightly more favourable orientation for basal slip. These deformation characteristics observed during *in-situ* compression are consistent with microstructures observed during bulk *ex-situ* compression. Hence, the deformation microstructure given in fig. 3.13 can claimed to be representative.

The experimental observations impose several questions regarding shear banding that will be answered with the help of high-resolution CP simulations in the following:

1. Is the observed intense basal slip activity the source for or a result of the shear band formation?

2. What is the impact of the observed slightly off-basal orientation on the shear band formation?

3. Why does continuous softening occur as consequence of localised intense basal slip and not, instead, gradual strain hardening?

As confirmed experimentally, results from the simulation showed mainly activity on the basal slip systems. Hence, only the basal slip activity is shown in fig. 3.14 for the considered load cases. The strain localisation experimentally observed in the upper part, as well as the inhomogeneously deforming area in the lower part are also the spots where high stress gradients could be observed in the simulation results. Looking at the upper part where experimentally the most severe strain localisation is observed, it is clear from fig. 3.12b that the orientation of these grains allows easy slip on basal systems. However, the experimentally determined strain localisation penetrates horizontally through the whole microstructure, while in the simulation it is interrupted for the first two load cases.

The results of the first load case, applying plane strain compression, are given in fig. 3.14a. It is clearly visible that no pronounced strain localisation in the form of a

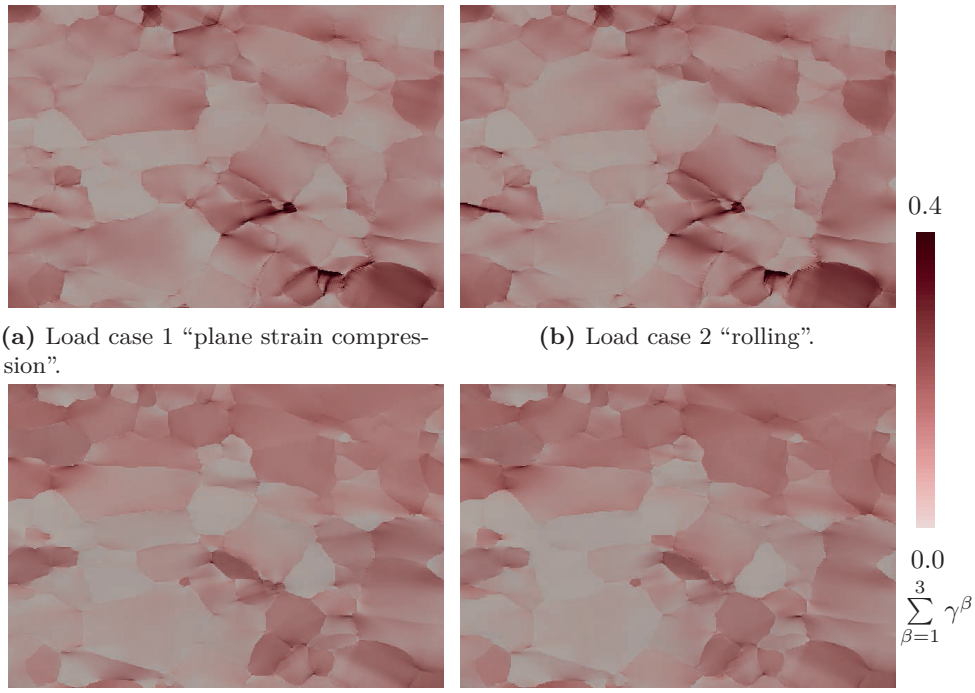

(a) Load case 1 “plane strain compression”.

(b) Load case 2 “rolling”.

(c) Load case 3.

(d) Load case 4.

Figure 3.14: Accumulated slip on basal systems at 0.05 compressive strain in vertical loading direction for the considered load cases.

shear band occurs, but instead high strain gradients at the grain boundaries are formed under these conditions. To verify the CP simulation result, channel die experiments were performed that confirmed that under this loading condition, no shear band is formed and instead early fracture of the material along the grain boundaries is observed (Wang et al., 2014). The results of rolling-type loading (fig. 3.14b) show slightly lower strain gradients at the grain boundaries than under pure plane strain compression conditions but also no strain localisation in the form of a shear band. This indicates that the in-plane shear relaxation does not promote shear banding and that instead out-of-plane deformation components seem to be required for the formation of shear bands during compression of Mg polycrystals. This assumption is confirmed by the results of the third load case given in fig. 3.14c. Clearly, a percolation of high basal slip activity in the upper region of the ROI can be seen in excellent agreement with the experimentally observed localised basal activity and shear band formation in fig. 3.13. The results imply the subsequent development of a considerable out-of-plane shear stress component during compression. A similar shear distribution resulted from the fourth load case fig. 3.14d, indicating that the additional degrees of freedom do not

contribute significantly to the deformation.

Given the similarity between fig. 3.14c and fig. 3.14d, a detailed discussion on the numerical results is based on results of both load cases. The experimentally most obvious feature, which is a strain localisation in the upper part is correctly predicted by the CP simulation. This indicates that the selected modelling approach is able to describe the micro-mechanics of the ROI correctly. Additionally, in accordance with the experimental results, the simulation predicts:

- at the bottom, less strain in the left part of the microstructure compared to the center part;
- a little deformed grain in the lower right part is surrounded by highly deforming grains;
- almost no tension twinning activity (not shown).

These findings imply that the out-of-plane shear stress component which is activated through the percolation of intense basal dislocation slip in slightly off-basal oriented grains is causing a dynamic self-enhancing process facilitating local softening and leading to the formation of shear bands in polycrystalline Mg with pronounced basal texture. Based on the above presented and discussed experimental and computational results the following mechanisms for shear band formation in basal-textured Mg is proposed: A cluster of slightly off-basal oriented grains (where the slightly inclined near-basal texture components might be retained from a preceding inhomogeneous hot working and/or rotation recrystallisation step) exhibit a slightly more favourable orientation for basal slip than grains with an almost perfect basal alignment. In these grains, intensive basal slip is locally activated during the on-set of plastic deformation leading to a micro-mechanical strain percolation effect in the form of a collective grain cluster deformation mechanism. This cumulated basal slip extending across multiple neighboured grains creates a pronounced shear component parallel to the active basal glide planes (out-of-plane) in the percolation area and, consequently, basal slip becomes more favourable in this area. Via this self-enhancing dynamical process strain localisation is facilitated and results in shear band formation.

In summary, the main observations and conclusions of this study presented in extended version by Wang et al. (2014) are:

1. Below an engineering strain of 5 %, Mg exhibits localised slip activity and twinning exclusively in shear bands. The strong basal texture and the associated grain clusters of similar basal orientation in the recrystallised Mg are an important factor responsible for strain localisation.

2. The combination of experiments and simulations shows that shear band formation is a result of percolated basal slip activity in slightly off-basal orientated grains. As a result of this locally cumulated intense basal slip a shear stress component parallel to the active basal glide planes develops and subsequently eases the basal slip leading to the formation of shear bands.

3. In Mg, tension twins are activated in areas with high local stresses, *i.e.* inside shear bands. The activation of tension twinning can be understood in combination with the local stress BC only.

Wang et al. (2014) additionally proposed that twinning is a process of accommodating local strain and thereby maintaining strain compatibility at grain boundaries rather than a response to macroscopically imposed strain at low strain levels. Failure to accommodate strain by twinning results in an orientation gradient in the vicinity of grain boundaries or even ledges at the grain boundary.

3.2 Artificial Microstructures

The limitations associated with the use of 2D microstructures are already outlined in section 3.1.1 and will be discussed in detail in this section. However, the (non-destructive) acquisition of 3D microstructures is time consuming and requires the availability of *e.g.* neutron diffraction devices. Therefore—especially when a large number of microstructures is needed—the generation of artificial microstructures is a convenient and usually time-efficient alternative to the use of experimentally acquired microstructures.

Three different simulation series based on artificial microstructures are presented here. First, in section 3.2.1, two approaches to generate artificial microstructures are outlined and the results are compared to investigate how the generation methodology influences stress and strain partitioning. After that, as a follow-up survey to the study on strain and stress partitioning in dual phase steel, the influences of the unknown subsurface microstructural features on the experimentally accessible 2D ROI are studied in section 3.2.2. Finally, pattern formation in polycrystalline ice under cyclic loading is examined in section 3.2.3 and the limitations of the phenomenological material model for cyclic loading conditions are discussed.

3.2.1 Comparison of Microstructure Generation Approaches

A well-known and widely used approach to generate artificial microstructures is the Voronoi tessellation. In this approach, the area or volume under consideration is partitioned into cells (*i.e.* "grains" in materials science) such that all cells together fill the whole area or volume under consideration. This is done by placing N seeds for N grains in the ROI; the area or volume that is closest to a given seed makes up a single grain. The grain boundary is than exactly located on the half of the distance between two neighbouring seeds. In the simplest case, the seeds are randomly distributed. When applying this approach on a regular grid as it is needed for the spectral solver, the use of efficient algorithms for the nearest neighbour search, *e.g.* based on a k-d tree (Kennel, 2004) enable a fast tessellation.

However, it is know that microstructures generated with the help of a standard Voronoi tessellation differ with respect to

1. Shape of the grains
2. Grain-size distribution

from real microstructures as shown by, *e.g.*, Xu et al. (2009).

Several approaches exist to approach the experimentally observed microstructural parameters: Lyckegaard et al. (2011) have shown that the weighted Voronoi tessellation (also called the Laguerre tessellation) allows reconstructing experimentally measured microstructures much better than the standard Voronoi tessellation. In this approach, assigning a weight to the seed points shifts the grain boundaries from the halfway position between the seeds to a position depending on the weights of the two adjacent grains. As a result, the grain size distribution can be adjusted by the choice of the weights and does not need to follow the one observed in the case of the standard approach with random seeds. A second approach that can also be used in conjunction with the Laguerre tessellation is the use of a non-random seed point distribution. Xu et al. (2009) proved that this approach in combination with a Monte Carlo simulation can be iteratively applied to generate microstructures that follow a prescribed grain size distribution. Since both methods are still closely related to the Voronoi tessellation, they are are able to change the grain *size distribution* but fail to generate grains with realistic grain *shapes*. More specifically, the grain boundaries are planes or straight lines. The simulation of grain growth (Krill III et al., 2002) is one way to change grain shape and size simultaneously.

In this study, microstructures are generated with a standard Voronoi tessellation and compared to microstructures obtained by a grain growth simulation. The aim of the simulation series is the investigation of possible differences in the micro-mechanical response of both approaches, which are either due to the grain shape or due to the grain size distribution. This investigation is of interest as a meta-study on micro-mechanical simulations, because a vast amount of current work is using Voronoi tessellated structures, *i.e.* implicitely it is usually assumed that the differences between these structures and real microstructures are negligible.

Isotropic grain growth

The simulation of grain growth in polycrystalline materials is often done using a phase field approach. Phase field models describe interfaces in a diffuse way and are suitable to model phenomena like solidification, crack propagation, and dislocation dynamics (Chen, 2002). For the simulation of grain growth, interface energy is assigned to the grain boundaries and minimised by repeated diffusion and sharpening. Sharp edges are associated with a high interfacial energy, and, hence, they vanish during the simulation of grain growth which is equivalent to the reduction of interfacial energy. In the isotropic model, the dependence of the energy on the grain boundary character is neglected. This allows modelling grain growth depending only on a unique grain number without considering the grains orientation or phase.

Microstructures

For a series of simulations, 14 microstructures with 100 grains are generated by a standard VORONOI tessellation. The microstructures have a periodic structure to avoid unrealistic grain boundaries that require in the case of experimentally obtained microstructures to limit the ROI to the center of the volume element (VE). Seed point locations are randomly chosen. The (initially constant) orientation of the individual grains is also randomly selected in EULER space. For a second series of simulations, first 14 microstructures with *1000* grains are generated also using a VORONOI tessellation. In a follow-up step, an isotropic grain growth algorithm is used to change grain shape and size distribution of these microstructures while retaining periodicity. In order so see a significant change in the microstructure characteristics, the grain growth simulation was performed until 900 grains are consumed by the growing grains. The same orientations as for the first microstructures have been randomly assigned to the 100 remaining grains. Hence, two sets with each having 14 microstructures are created. Each microstructure has 100 grains and the EULER angles of the grains match pairwise between two microstructures in both sets. The geometries are mapped on a $256 \times 256 \times 256$ grid on a unit square cube. This high resolution was chosen to avoid any artefacts at the grain boundaries due to the "staircase-shape" approximation of a smooth surface.

The top view on one randomly selected microstructure for both approaches is shown in fig. 3.15. From this figure, the grain shape difference can clearly be seen: Grains generated using the standard VORONOI tessellation (see fig. 3.15a) have boundaries without curvature and acute angles between the straight segments.

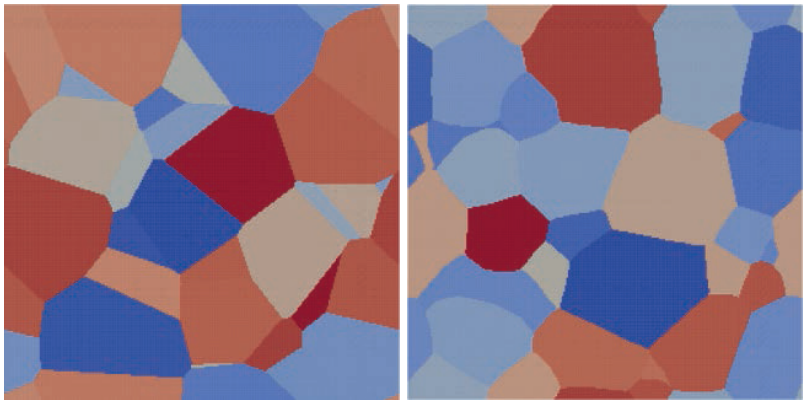

(a) Microstructure generated by a standard VORONOI tessellation.

(b) Microstructure generated by an isotropic grain growth simulation of originally 1000 grains.

Figure 3.15: Top view on two microstrucutres consisting of 100 grains generated by two different approaches. Color indicates unique grain number.

These features typical for the standard VORONOI tessellation are energetically unfavorable in a grain growth simulation and therefore cannot be seen in fig. 3.15b. Since the grain size distribution is difficult to estimate from a 2D slice (*i.e.* comparing fig. 3.15a with fig. 3.15b), the average grain size for all 2×14 microstructures is shown in fig. 3.16. A significant difference can be seen here: Compared to the dense size distribution of the standard VORONOI tessellation, where most of the 1400 grains occupy approximately 1/10 of the volume and the others take up at most twice that volume, the grain growth simulation results in a strong grain size partitioning. One single grain is occupying up to 60 % of a volume in a particular microstructure. The requirement of having 100 grains in each VE results in a large number of extremely small grains that are just about to be consumed by the growing large grains.

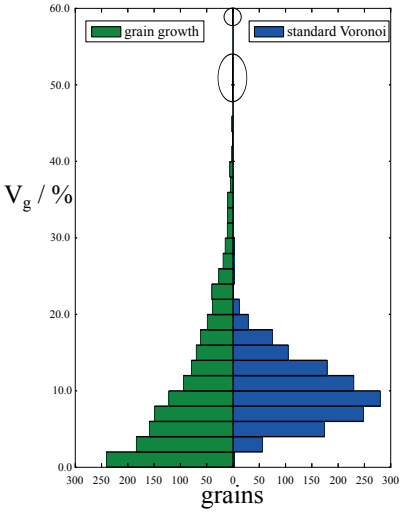

Figure 3.16: Grain size distribution obtained by VORONOI tesselation and by a grain growth algorithm. The circle and the ellipse indicate non-empty bins.

It should be noted that neither of the grain size distributions is representative for *all* real microstructures, since in general fundamentally different grain size distributions might be observed in reality. The two sets rather represent two specific cases: The first set of microstructures has characteristics typical for VORONOI tessellated structures as investigated in detail by Meijering (1953) and Kumar et al. (1992). Like, *e.g.* Nickel (Dalla Torre et al., 2002), the grain size distribution follows a lognormal distribution. However the experimentally obtained distributions might have different standard deviations than the 0.45 found in VORONOI tessellated structures Xu et al. (2009). The design goal for the second set was the creation of a microstructure that differs significantly from the first one. With a few extremely large grains and a high number of small grains it can be considered as a microstructure that has undergone abnormal grain growth.

Modelling Details

Since the exact material behaviour is not of special interest in this study, an existing parameter set to model copper using the phenomenological material model is used to describe the single crystal behaviour. The parameters for the fcc structure with 12 $\langle 1\,1\,1\rangle\{1\,1\,0\}$ slip systems are given in table 3.5. The VE was loaded in uniaxial tension with a constant technical strain rate of $1.0 \times 10^{-3}\,\mathrm{s}^{-1}$ with stress free normal directions:

$$\dot{\boldsymbol{F}} = \begin{bmatrix} 0.001 & 0.000 & 0.000 \\ 0.000 & * & 0.000 \\ 0.000 & 0.000 & * \end{bmatrix},$$

where the asterisk "$*$" indicates a stress free component for $\boldsymbol{P}$. This load was applied for 20 s, *i.e.* until a final strain of 20.0 % was reached.

Table 3.5: Material parameters for copper.

Property	Value	Unit
C_{11}	106.8×10^9	Pa
C_{12}	60.4×10^9	Pa
C_{44}	28.3×10^9	Pa
$\dot{\gamma}_0$	1.0×10^{-3}	$\mathrm{m\,s^{-1}}$
ξ_0	31.0×10^6	Pa
ξ_∞	63.0×10^6	Pa
$h_{\alpha\beta}$	75.0×10^6	
n	20.0	
a	2.25	

Results and Discussion

In the following, the results of the VEs in terms of the equivalent VON MISES strain ($\varepsilon_{\mathrm{vM}}$) and stress ($\sigma_{\mathrm{vM}}$) are discussed. Despite the significantly different grain size distribution (see fig. 3.16), no difference in the global stress–strain curves can be observed. A more detailed analysis of the average stress and strain state in the individual grains confirms this observation: In fig. 3.17 $\varepsilon_{\mathrm{vM}}$ (fig. 3.17a) and σ_{vM} (fig. 3.17b) are shown in comparison. The results shown in green color (left side) are obtained from the microstructures generated with the help of the grain growth simulation, the results given in blue (right side) are obtained from the VEs generated by standard VORONOI tessellation. Figure 3.17a shows that only a slight difference in $\varepsilon_{\mathrm{vM}}$ exists between the two approaches. Namely, the strain of the VORONOI tessellated microstructures is slightly more concentrated around the average value of 20 %. In the stress response, a less pronounced peak at high values in a bimodal distribution can be seen for the microstructure obtained by the grain growth simulation.

For a quantitative analysis of the in-grain stress distribution, the following procedure is applied: First, a normed histogram distributing the results into 60 bins[1] designated as $h_0^{60}(n)$ $n = 1 \ldots 2800$ was computed for each of the 2800 grains. The results of individual grains for the two approaches are then summed up to get two histograms $h^{60}_{0,\mathrm{grown}} = \sum_{n=1}^{1400} h_0^{60}(n)$ and $h^{60}_{0,\mathrm{VORONOI}} = \sum_{n=1401}^{2800} h_0^{60}(n)$. Finally, the difference between the two histograms is calculated per bin as $\Delta h_0^{60} = h^{60}_{0,\mathrm{grown}} - h^{60}_{0,\mathrm{VORONOI}}$ and

1 The integral over the 0 to 60 bins equals to 1.0.

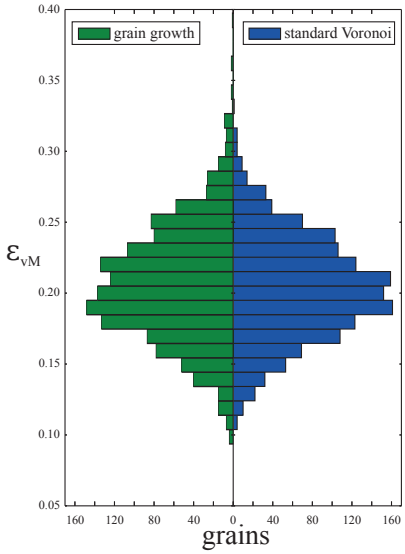

(a) Distribution of $\varepsilon_{\mathrm{vM}}$ per grain of all 28 microstructures.

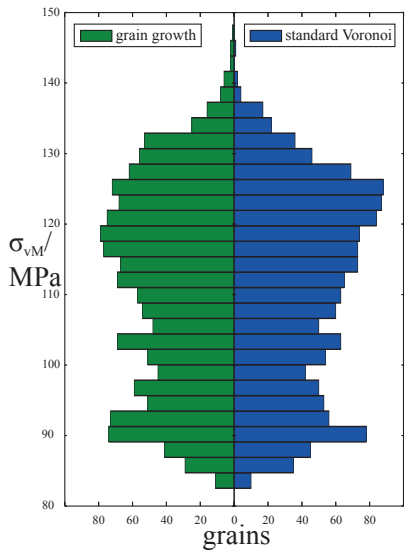

(b) Distribution of σ_{vM} per grain of all 28 microstructures.

Figure 3.17: Distribution of equivalent strain, $\varepsilon_{\mathrm{vM}}$, and equivalent stress, σ_{vM}, resulting from the grown microstructures on the left (green) and the standard Voronoi tessellation on the right (blue).

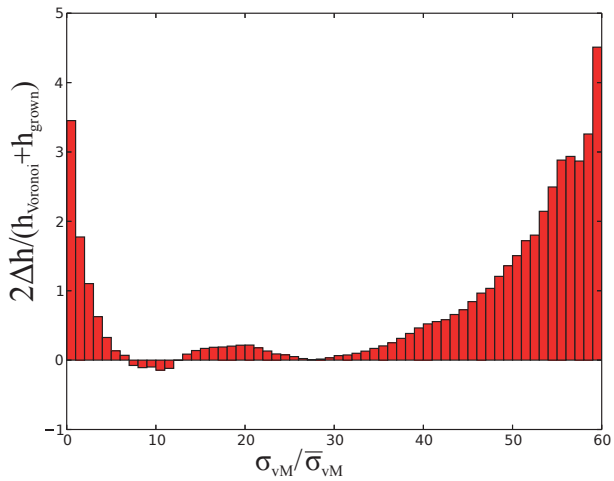

Figure 3.18: Relative difference in distribution of normalised in-grain stress values.

normed over the average per bin $0.5 \cdot (h^{60}_{0,\text{grown}} + h^{60}_{0,\text{VORONOI}})$. The plots of this procedure given in fig. 3.18 indicate that the in-grain stress distribution differs significantly between the two microstructure generation approaches. Using the standard VORONOI tessellation results in a more flat distribution, where especially the high stress values occur less often than for the microstructures having grown grains. For the in-grain strain distribution (not shown), a similar behaviour is observed, where, however, the increase for small values was less pronounced than for the stress distribution shown in fig. 3.18.

It can be assumed that the high number of small grains in the microstructures that have undergone grain growth is the reason for the observed differences in the in-grain stress distribution. These grains have a comparably high surface-to-volume ratio and therefore a higher ratio of material points at the grain boundary that adapt to the behaviour of the differently oriented neighbouring grains. Since the phenomenological material model is a size-independent and local model, no size effects or a strain gradient behaviour can counteract the resulting stress and strain partitioning. However, the absence of sharp edges in comparison to the VORONOI tessellated structures might soften the effect coming from the grain size alone. Further investigations using a constraint VORONOI tessellation that allows using the grain size distribution of the microstructures generated with the grain growth simulation as an input parameter will help to interrogate if this is a result of the grain shape or of the grain size distribution.

In summary the results show that the grain shape and grain size distribution have only a minor influence on the average results when using the phenomenological material model. This indicates that using the fast standard VORONOI approach is justified for simulations that aim at investigating *e.g.* the stress–strain response or the mean stress–strain partitioning. However, in the case of investigations at a very local scale, the artificial grain shape and/or grain size distribution introduces an error that might influence the results. For example, more realistic grain structures should be used when damage mechanisms are included in the simulation. In damage modelling, already small local deviations might influence the behaviour of the whole structure drastically and therefore result in unexpected behaviour.

3.2.2 Subsurface Effects in Simplified Dual Phase Steel

As outlined in section 3.1.1, a full understanding of the local stress and strain partitioning that determines the global mechanical properties of DP steels is not achieved yet. Despite the general ability of taking the full 3D microstructure into account (Chen et al., 2014), most recent simulation approaches comparing experimental and simulated results (*e.g.* Ramazani et al., 2014; Tasan et al., 2014a) are limited to two dimensions due to experimental limitations. More precisely, the acquisition of 3D strain maps via digital volume correlation or of stress partitioning via X-ray diffraction is associated with high experimental effort. Hence, even though Landron et al. (2013) presented a study on void coalescence in DP steels using 3D data, most of the investigations are still limited to surface measurements of microstructural features and—with the help of digital image correlation—strain partitioning.

Figure 3.19: Color map for the IPFs (parallel to z).

To better understand the behaviour investigated in section 3.1.1, here the effects of subsurface features—that are difficult to obtain in a non-destructive fashion—on experimentally obtainable surface measurements is investigated. The pioneering work of Zeghadi et al. (2007a,b) has already shown the importance of subsurface microstructure. The presented study extends their investigations to the case of a dual phase microstructure. Moreover, the size of the region of influence is quantified by systematically evaluating the interactions of microstructural features in relation to the distance to the ROI at the surface. This study is published in extended form by Diehl et al. (2015)

Microstructures

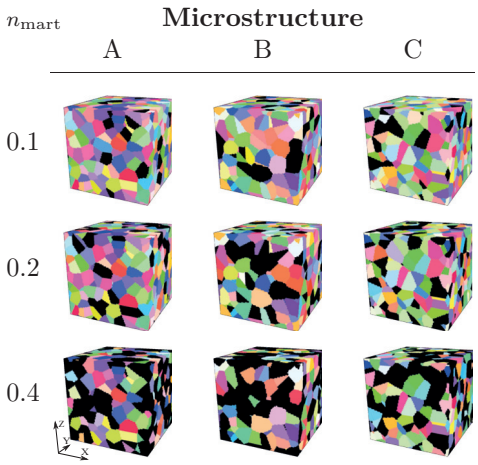

Figure 3.20: Periodic microstructures A, B, and C (left to right) discretised by 100^3 points and containing a total of 400 grains. Black color indicates martensite grains with fraction of $n_{\mathrm{mart}} = 0.1$, 0.2, and 0.4 (top to bottom). For IPF legend see fig. 3.19.

Three periodic, artificial grain structures, each filling a unit cube, are created by a standard VORONOI tessellation (also see section 3.2.1) approach based on 400 randomly[1] placed seed points each. These structures, referred to as "A", "B", and "C", are discretised by a regular grid of $100 \times 100 \times 100$ points. All grid points of one grain are designated the same phase (ferritic or martensitic) with initially homogeneous and randomly chosen lattice orientation. For each of the three microstructures, a fraction $n_{\mathrm{mart}} = 0.1$, 0.2, and 0.4 of the grains are randomly selected as martensitic, resulting in martensite volume fractions of 9.24 % to 11.23 %, 18.41 % to 20.56 %, and 38.83 % to 40.62 %, respectively. The resulting nine initial microstructures are given in fig. 3.20.

Parameters for the constitutive behaviour are the same as in the study on strain and stress partitioning in dual phase steel presented in section 3.1.1 (table 3.1).

1 Ensuring that at least one voxel is assigned to each seed point when discretising on a 64^3 grid.

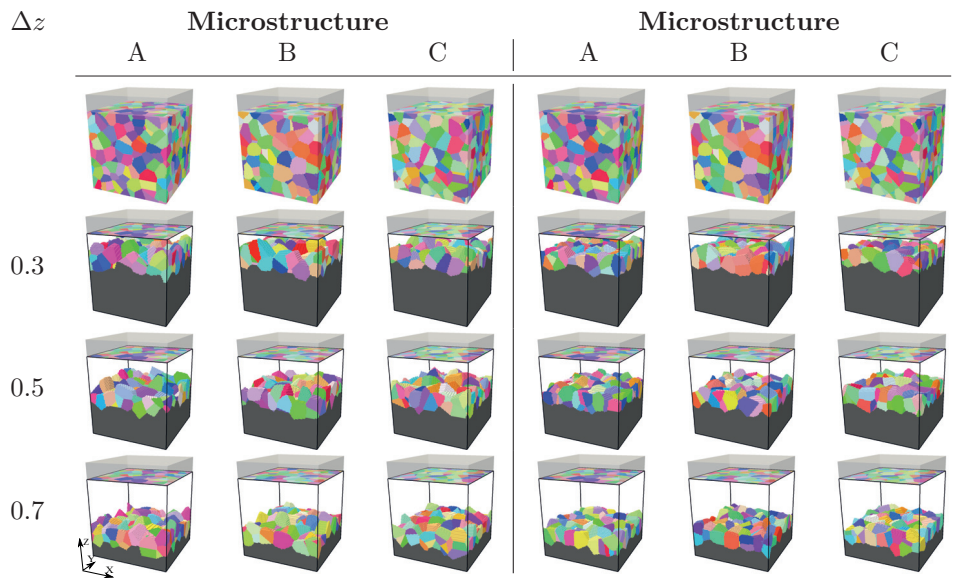

Figure 3.21: Localised variation of grain *orientation* (left) and grain *shape* (right). Grains whose VORONOI seed points fall within a layer of thickness $t = 0.2$ centered Δz below the (top) surface have altered lattice orientation or altered postion of seed point relative to unaltered structure (top, transparent, and bottom, dark gray color), respectively. The fade gray color indicates the "buffer zone". For IPF legend see fig. 3.19.

Grain Orientation Variation In a first simulation series, the influence of the subsurface grain orientation on the kinematic response at a surface is investigated. For that, 27 variants of the initial 9 microstructures are created by randomly altering the *lattice orientation* of grains that belong to VORONOI seed points within a slice of thickness $t = 0.2$ centered at the plane $\Delta z = 0.3$, 0.5, or 0.7 below the surface (at $z = 1$). No values $\Delta z < 0.3$ are considered, since the lattice orientation of grains observable at $z = 1$ (*i.e.* the ROI at the surface) might be changed. A "buffer zone" of height 0.2 (corresponding to 20 additional grid layers along z) is added in between periodic repetitions of the microstructure (see left side of fig. 3.21). Elastic-isotropic behaviour with $C_{11} = 20.0\,\mathrm{GPa}$ and $C_{12} = 13.3\,\mathrm{GPa}$ is assigned to this zone. Introduction of the buffer zone above the ROI at $z = 1$ results in boundary conditions that are reminiscent of a free surface. The microstructure geometry can be best described as a "thick film".

Grain Shape Variation In the same spirit as for the grain orientation variation, 27 variants of the initial 9 microstructures are created by randomly altering the *position* of VORONOI seed points within a slice of thickness $t = 0.2$ centered at the plane $\Delta z = 0.3$, 0.5, or 0.7 below the surface (at $z = 1$). The change in position is limited to a distance

of the equivalent average grain radius.[1] As a consequence of the altered seed positions, the tessellation results in differently shaped grains in the vicinity of the affected plane (see right side of fig. 3.21). No values $\Delta z < 0.3$ are considered, since the geometry of the grain structure observable at the ROI might be changed by altering the seed point coordinates close to this (surface) plane. Again, to mimic the effect of a free surface at the ROI, a "buffer zone" consisting of a soft material is added in between periodic repetitions of the microstructure to get a a "thick film" behaviour.

Microstructure Variety Reduction To interrogate the influence of grains within a bulk polycrystal that are located some distance from a (planar) ROI, taken as the plane $z = 0.5$, the height of the periodic grain structure introduced in section 3.2.2 is gradually reduced to $h = 0.9, 0.8, \ldots, 0.3$.[2] The periodic VORONOI tessellation then includes only seed points within $\Delta z < h/2$ from $z = 0.5$, thus progressively altering the neighbourhood around the central x–y plane. This results in a reduction of the length of the periodically repeated microstructure in z-direction. Additionally, the limit case of keeping only the ROI layer of $h = 0.01$ (*i.e.* assuming columnar grains due to the periodic boundary conditions) is investigated. No buffer zone is applied, since bulk polycrystal properties are of interest in this case. Figure 3.22 presents exemplary microstructures of heights $h = 0.8, 0.5, 0.3, 0.01$ for all three structures with fixed martensite grain fraction $n_{\mathrm{mart}} = 0.2$ (corresponding to center row in fig. 3.20). As it can be seen from the grain count for all microstructures given in table 3.6, the described procedure results in a subsequent reduction of variety of the periodically repeated VE.

Table 3.6: Grain count of the microstructures with reduced variety.

z	0.9	0.8	0.7	0.6	0.5	0.4	0.3	0.01
A	355	318	284	247	195	157	123	79
B	358	305	263	225	185	153	106	72
C	362	316	276	232	198	158	111	73

Modelling Details

The VEs were subjected to loading in x-direction, *i.e.* the ROI is deformed in-plane, commensurate with the surface of a deformation sample. For the grain orientation variation and grain shape variation a constant true strain rate of $L_{xx} = 10^{-3}\,\mathrm{s}^{-1}$ and $L_{\mathrm{yy}} = -10^{-3}\,\mathrm{s}^{-1}$ was applied. Since the soft layer mimics a free surface, no stress boundary conditions are given and the remaining components of $\boldsymbol{F}$ remain constant. After a loading time of 46.0 s, the final deformation gradient prescribing plane strain is

1 $400\, {r_{\mathrm{vM}}}^3\, 4\,\pi/3 = 1$.
2 $h < 0.3$ resulted in changes of the grain structure slice at $z = 0.5$ and was therefore not considered.

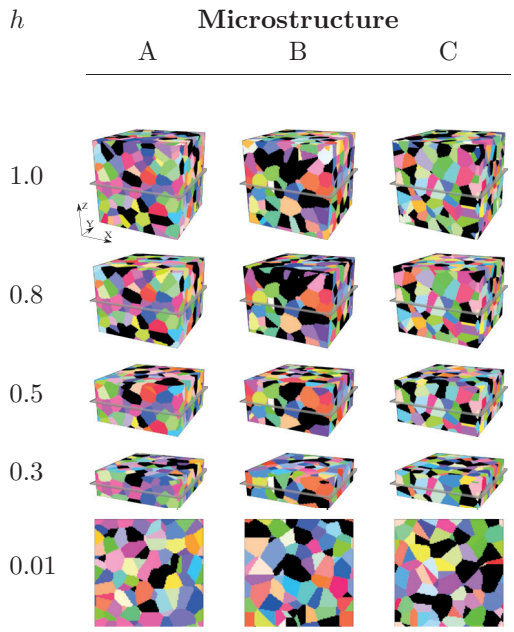

Figure 3.22: Microstructure variety reduction. The height h of the initial microstructures with the central $x-y$ plane as ROI (indicated by the bright grey slice) is gradually reduced while periodicity in z direction is retained. The variant with $n_{\mathrm{mart}} = 0.2$, indicated by black color is shown here. For IPF legend see fig. 3.19.

$$\boldsymbol{F} = \begin{bmatrix} 1.047 & 0.000 & 0.000 \\ 0.000 & 0.955 & 0.000 \\ 0.000 & 0.000 & 1.000 \end{bmatrix}.$$

For the microstructure variety reduction, a constant engineering strain rate of $\dot{F}_{xx} = 10^{-3}\,\mathrm{s}^{-1}$ was applied. The deformation gradient in y- and z-direction was adjusted such that the average Piola–Kirchhoff-stress in these directions vanished. This plane stress boundary condition was applied for 82.0 s, resulting in the deformation gradient

$$\boldsymbol{F} = \begin{bmatrix} 1.082 & * & * \\ 0.000 & * & * \\ 0.000 & 0.000 & * \end{bmatrix},$$

where the asterisk "$*$" indicates a stress free component for $\boldsymbol{P}$.

As discussed in comparison of spectral solver variants, the direct variational formulation was selected as the *de-facto* standard approach in this thesis. However, for the columnar microstructures ($z = 0.01$) used in microstructure variety reduction, only the polarisation field-based scheme was able to converge to the desired strain level.

Results and Discussion

In the following, the results—*i.e.* the stress and strain partitioning—of the grain orientation variation, the grain shape variation, and the microstructure variety reduction are given. For the analysis, the absolute difference Δp is defined as $\Delta p := p - p^{\mathrm{ref}}$ for $p \in \sigma_{\mathrm{vM}}, \varepsilon_{\mathrm{vM}}$ where the reference value is the one obtained from the unaltered microstructure. Additionally, the relative difference is calculated as $\Delta p / p^{\mathrm{ref}}$.

For all three simulation studies, the spatially resolved equivalent VON MISES stress (σ_{vM}) and strain ($\varepsilon_{\mathrm{vM}}$) maps on the ROI of one selected microstructure variant A, B, or C are given together with the relative change of these quantities for the altered microstructures in figs. 3.23, 3.26 and 3.29 To visualize the large difference of stress and strain in the soft ferrite and the hard martensite, a logarithmic scale is used for the results of the unaltered microstructure.

Additionally, the data is averaged over all three microstructures and plotted in "heatmaps" where dark values represent more data points. For a more quantitative analysis of the partitioning, the absolute strain difference is plotted against the absolute stress difference and shown separately for ferrite and martensite (see figs. 3.24 and 3.27). Additionally, the influence of the phase boundary on the strain difference is investigated in figs. 3.25, 3.28 and 3.31. The distance (in pixel, px) of a a material point with martensite behaviour to the next material point with ferrite behaviour in the undeformed configuration is denoted as d_{ferrite}. Similarly, for a ferritic point the distance to the next point with martensitic behaviour is called $d_{\mathrm{martensite}}$.

Stress and strain partitioning of microstructure A at $z = 1.0$ resulting from the grain orientation variation is shown in fig. 3.23. It can clearly be seen that the strain partitioning (see left side of fig. 3.23) is heavily influenced when the microstructure is modified at a distance of $\Delta z = 0.3$ to the surface. Evenly distributed over the ROI, the values of $\varepsilon_{\mathrm{vM}}$ are above or below the values for the initial microstructure, with extreme values of ± 1.0, *i.e.* $\pm 100\,\%$. The stress distribution changes in a locally more concentrated way with lower extreme values ranging from $-60\,\%$ to $60\,\%$ as shown in fig. 3.23 (right side). For both, stress and strain, no significant influence can be seen for the modification of the VE at $\Delta z = 0.5$, and 0.7.

The joint data of all three variants together, given in fig. 3.24, confirms the observations made for microstructure A: The influence of a grain orientation change is spatially confined to a narrow zone below the ROI and largely independent of the content of the hard phase. For distances $\Delta z \geq 0.5$, almost no influence on the ROI can be observed. Since the average diameter size is approximately 0.13, it can be concluded the zone of influence is confined to a zone of three grains. This is slightly deeper than the zone of influence in single phase polycrystals obtained by Zeghadi et al. (2007b).

Inspecting the dependence of $\Delta\varepsilon_{\mathrm{vM}} / \varepsilon_{\mathrm{vM}}^{\mathrm{ref}}$ on the distance to a phase boundary in fig. 3.25 shows that the points close to such a phase change are much stronger affected than the ones located in the phase center. This probably explains why the zone of influence is larger than in the case of polycrystals without a second phase: The strong stress and strain partitioning among the phases has a longer range of interaction than

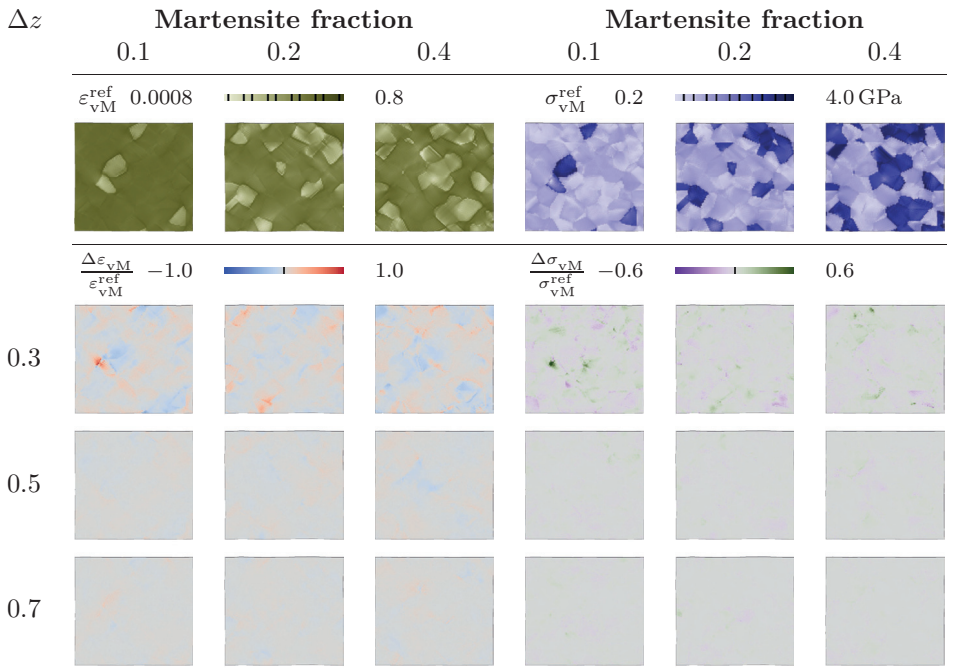

Figure 3.23: ε_{vM}^{ref} (left) and σ_{vM}^{ref} (right) of microstructure A at $z = 1$ shown together with $\Delta\varepsilon_{vM}/\sigma_{vM}^{ref}$ (left) and $\Delta\sigma_{vM}/\sigma_{vM}^{ref}$ (right) at $\Delta z = 0.3, 0.5, 0.7$ for $n_{mart} = 0.1, 0.2, 0.4$ resulting from the grain orientation variation.

the weaker partitioning among differently oriented grains in a single phase material. The left side of fig. 3.25 also reveals that the zone of influence in ferrite is not only confined to the phase boundary, indicating that *e.g.* grain boundaries from ferrite to ferrite are also zones that are influenced above average by a modification of the microstructure.

Stress and strain partitioning resulting from the grain shape variation are shown for the ROI of microstructure B in fig. 3.26. The influence when the microstructure is modified at a distance of $\Delta z = 0.3$ to the surface is—as expected—the strongest. Comparing strain (see left side of fig. 3.26) and stress (see right side of fig. 3.26) shows, like for the grain orientation variation, the relative change in stress is more severe than the one in the strain. Additionally, the influence is more pronounced for higher martensite contents. Looking at fig. 3.27 clearly shows that this is true for the combined results of all microstructure variants.

From a comparison of the results of the grain orientation variation to the grain shape variation, three observations can be made:

1. The effect of the grain orientation variation is weaker than the effect of the grain

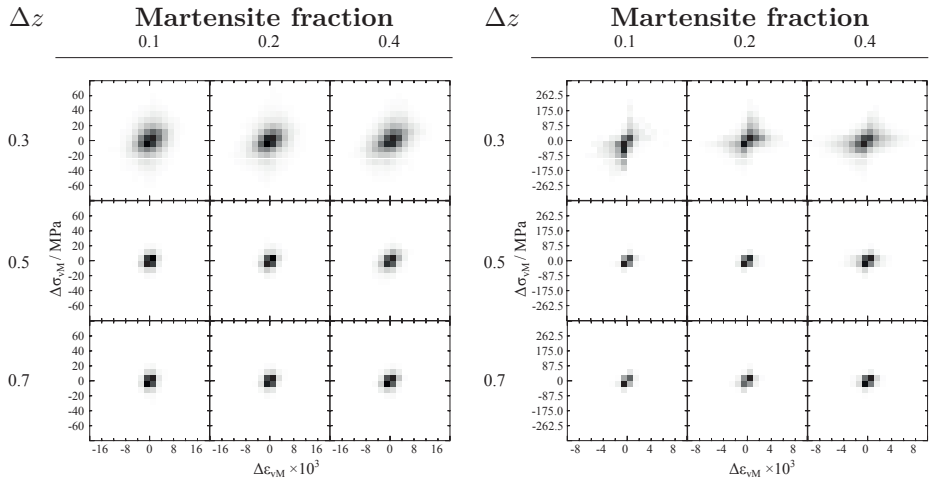

Figure 3.24: $\Delta\sigma_{\mathrm{vM}}$ plotted over $\Delta\varepsilon_{\mathrm{vM}}$ in ferrite (left) and martensite (right) at $\Delta z = 0.3, 0.5, 0.7$ for $n_{\mathrm{mart}} = 0.1, 0.2, 0.4$ resulting from the grain orientation variation.

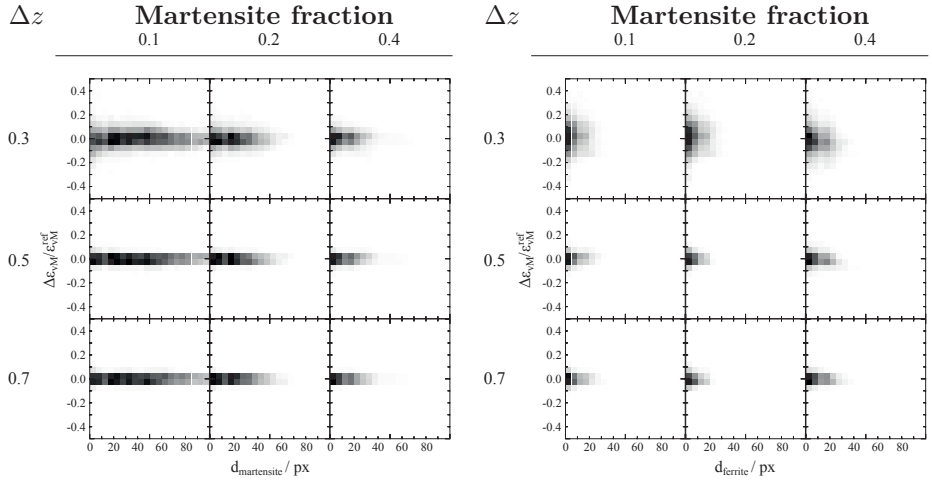

Figure 3.25: $\Delta\varepsilon_{\mathrm{vM}}/\varepsilon_{\mathrm{vM}}^{\mathrm{ref}}$ in ferrite (left) and martensite (right) plotted over $d_{\mathrm{martensite}}$ and d_{ferrite}, respectively, at $\Delta z = 0.3, 0.5, 0.7$ for $n_{\mathrm{mart}} = 0.1, 0.2, 0.4$ resulting from the grain orientation variation.

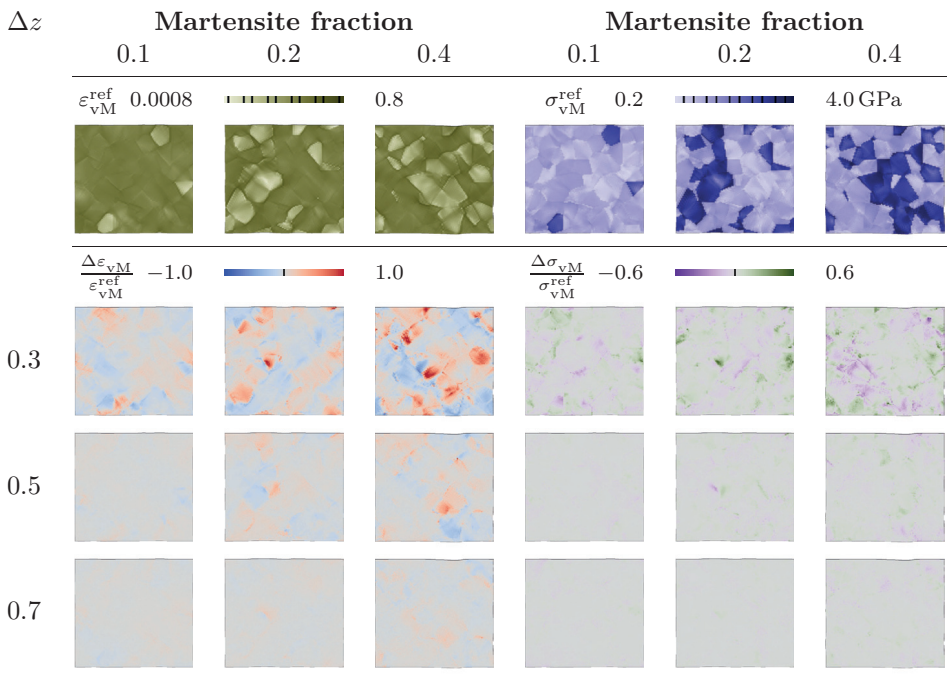

Figure 3.26: ε_{vM}^{ref} (left) and σ_{vM}^{ref} (right) of microstructure C at $z = 1$ shown together with $\Delta\varepsilon_{vM}/\sigma_{vM}^{ref}$ (left) and $\Delta\sigma_{vM}/\sigma_{vM}^{ref}$ (right) at $\Delta z = 0.3, 0.5, 0.7$ for $n_{mart} = 0.1, 0.2, 0.4$ resulting from the grain shape variation.

shape variation at the same distance Δz to the ROI.

2. The effected zone of the grain shape variation is deeper than for the grain orientation variation.

3. The effects of the grain shape variation depend—in contrast to the effects of the grain orientation variation—on the martensite volume fraction. A higher martensite volume fraction correlates with a more pronounced effect on the stress and strain partitioning.

Finally, the results of the microstructure variety reduction are presented. Since they are obtained with a different load case and at a higher strain level, the scale bars differ in comparison to the results of the first two simulation series. Stress and strain partitioning are shown for microstructure A in fig. 3.29 at $z = 0.5$. Relative differences in strain ($\Delta\varepsilon_{vM}/\varepsilon_{vM}^{ref}$) are higher than 250 % (left side of fig. 3.29) and relative differences in stress ($\Delta\sigma_{vM}/\sigma_{vM}^{ref}$) are higher than 100 % (right side of fig. 3.29) for the height reduction to $h = 0.3$. As it can be deducted from the stress and strain partitioning of the unaltered microstructure (top row), very high $\Delta\varepsilon_{vM}/\varepsilon_{vM}^{ref}$ relative

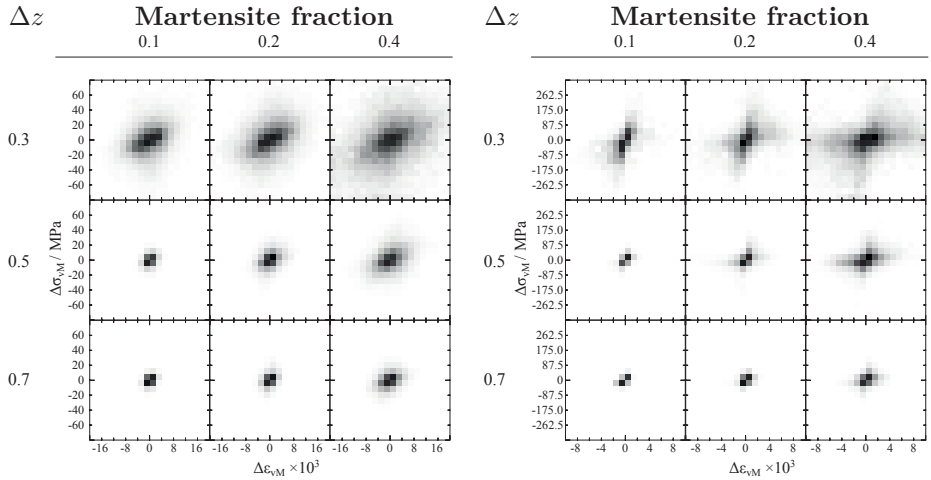

Figure 3.27: $\Delta\sigma_{\mathrm{vM}}$ plotted over $\Delta\varepsilon_{\mathrm{vM}}$ in ferrite (left) and martensite (right) at $\Delta z = 0.3,\ 0.5,\ 0.7$ for $n_{\mathrm{mart}} = 0.1,\ 0.2,\ 0.4$ resulting from the grain shape variation.

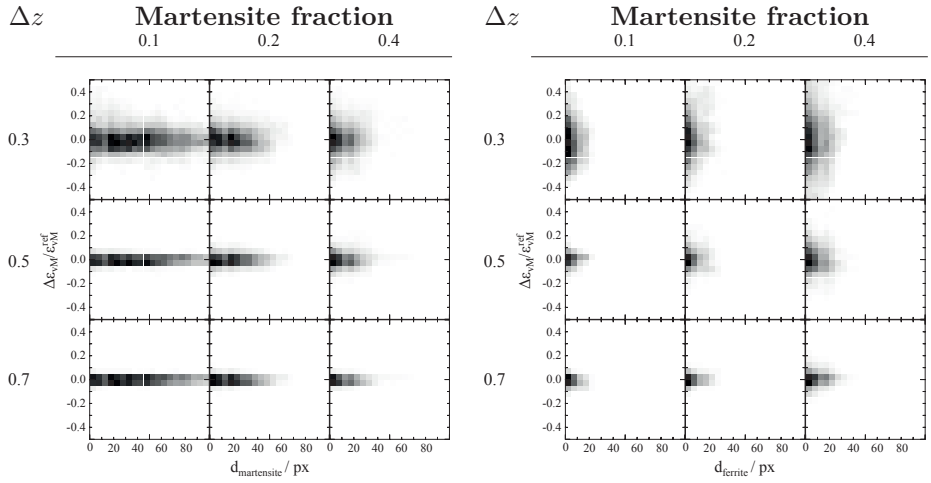

Figure 3.28: $\Delta\varepsilon_{\mathrm{vM}}/\varepsilon_{\mathrm{vM}}^{\mathrm{ref}}$ in ferrite (left) and martensite (right) plotted over $d_{\mathrm{martensite}}$ and d_{ferrite}, respectively, at $\Delta z = 0.3,\ 0.5,\ 0.7$ for $n_{\mathrm{mart}} = 0.1,\ 0.2,\ 0.4$ resulting from the grain shape variation.

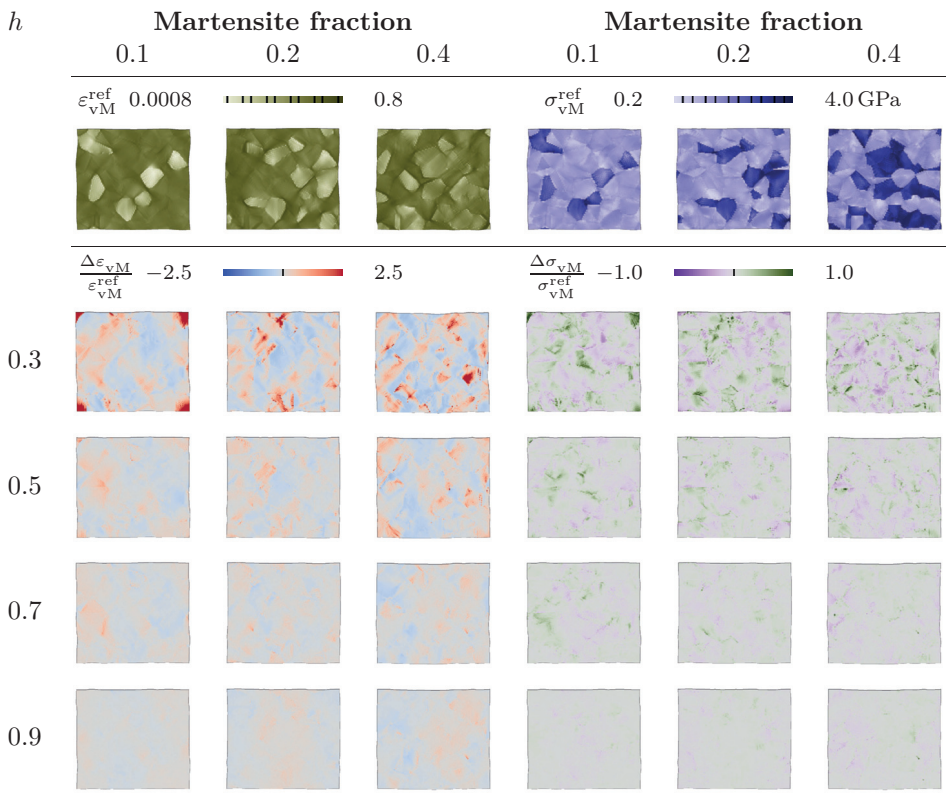

Figure 3.29: ε_{vM}^{ref} (left) and σ_{vM}^{ref} (right) of microstructure B at $z = 0.5$ shown together with $\Delta\varepsilon_{vM}/\sigma_{vM}^{ref}$ (left) and $\Delta\sigma_{vM}/\sigma_{vM}^{ref}$ (right) for $h = 0.3$, 0.5, 0.7 and 0.9 and for $n_{mart} = 0.1$, 0.2, 0.4 resulting the microstructure variety reduction.

strain changes occur mainly in the martensite. Looking at the definition for the absolute change in strain, $\Delta\varepsilon_{vM} := \varepsilon_{vM} - \varepsilon_{vM}^{ref}$, it becomes clear that the division by small small ε_{vM}^{ref} values in martensite causes these extreme values for $\Delta\varepsilon_{vM}/\varepsilon_{vM}^{ref}$. This also explains, why the absolute value of $\Delta\varepsilon_{vM}/\varepsilon_{vM}^{ref}$ for positive $\Delta\varepsilon_{vM}/\varepsilon_{vM}^{ref}$ is much higher than for negative $\Delta\varepsilon_{vM}/\varepsilon_{vM}^{ref}$: Both values, ε_{vM} and ε_{vM}^{ref}, are positive by definition resulting in a lower bound of 1.0 for $\Delta\varepsilon_{vM}/\varepsilon_{vM}^{ref}$. These observations show that expressing the differences in terms of relative changes is meaningless for the resulting extreme differences. Therefore, to visualise the influence of the reduction of the microstructure variability unbiased by the values of ε_{vM}^{ref} and σ_{vM}^{ref}, $\Delta\varepsilon_{vM}$ and $\Delta\sigma_{vM}$ of microstructure A are plotted in fig. 3.30 to avoid the artefacts introduced when calculating their relative counterparts. From the left figure in fig. 3.30 it can be seen that $\Delta\varepsilon_{vM}$ changes significantly in the ferritic regions. Especially for $n_{mart} = 0.4$

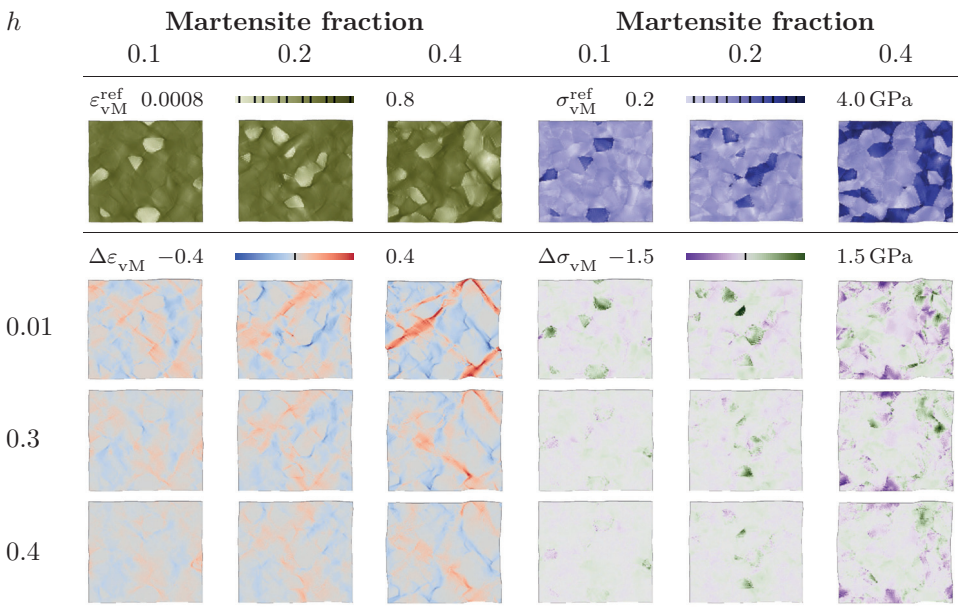

Figure 3.30: ε_{vM}^{ref} (left) and σ_{vM}^{ref} (right) of microstructure A at $z = 0.5$ shown together with $\Delta\varepsilon_{vM}$ (left) and $\Delta\sigma_{vM}$ (right) for $h = 0.01$, 0.3, 0.4 and for $n_{mart} = 0.1$, 0.2, 0.4 resulting the microstructure variety reduction.

and $h = 0.01$, the localised deformation bands in ferrite are obvious. They even lead to a clearly visible distortion of the geometry when compared to higher values of h or lower values of n_{mart}. Most of the martensitic regions that are also in the unmodified microstructures only slightly deformed, change their stain level much less pronounced. However, looking at the right side of fig. 3.30 reveals that the stress level in these grains is often heavily changed.

As it can be seen from the left side of fig. 3.31, in the case of a columnar grain structure and $n_{mart} = 0.4$ the ferrite is strained much more than in the reference set-up. The right side of fig. 3.31 shows that the martensite also shows significantly different deformation behaviour in that case. Interestingly, this effect is much less pronounced for lower n_{mart} and/or even a small surrounding microstructure ($h \geq 0.3$) in the third direction. The dependence on the martensite content is most likely related to the connectivity of the martensitic grains: For small, isolated martensitic grains the influence on the strain partitioning is lower than for connected skeletons that force specific ferritic regions to adopt most of the prescribed strain.

The conducted study underlines—in accordance with the findings of Zeghadi et al. (2007a,b)—the importance of subsurface microstructural features on the observed stress and strain partitioning. Moreover, the presented results show that an increased heterogeneity in the local response also increases the volume that is influenced by a

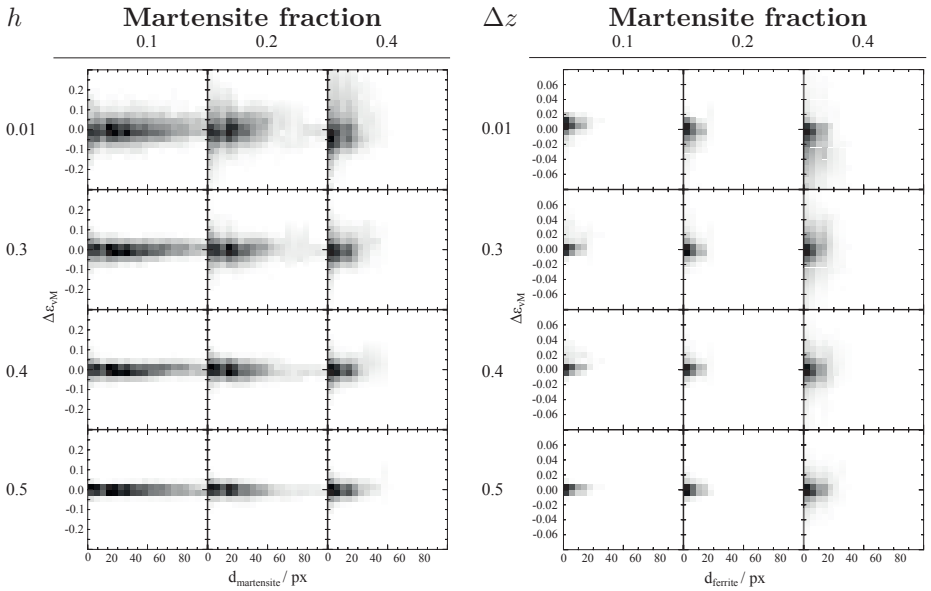

Figure 3.31: $\Delta\varepsilon_{\mathrm{vM}}/\varepsilon_{\mathrm{vM}}^{\mathrm{ref}}$ in ferrite (left) and martensite (right) plotted over $d_{\mathrm{martensite}}$ and d_{ferrite}, respectively, for $h = 0.01$, 0.3, 0.4 0.5 and for $n_{\mathrm{mart}} = 0.1$, 0.2, 0.4 resulting from themicrostructure variety reduction.

microstructural change. Since the stress and strain partitioning is mainly governed by the phase distribution, the crystallographic orientation of the subsurface microstructure is of less importance than the phase distribution. For a phase contrast similar to the ones found in DP steels, as a rule-of-thumb, the microstructure that is more than 3 grains away can be considered to be of minor importance for the observed stress and strain partitioning on a surface. However, the more complex microstructure of real DP steels with connected martensitic skeletons between ferritic grains might result in a larger zone of influence.

The assumption of columnar grain structures introduces a strong bias, as the stress and strain partitioning becomes stronger in the case of a material consisting of a hard and a soft phase. This renders especially the prediction of microstructure damage effects difficult in 2D simulations when a focus is laid on predicting the exact location of a damage incident.

The following procedure to get a *statistically representative* microstructure response is proposed for obtaining microstructure–property relations in multi-phase materials: Starting from a 2D ROI, several 3D microstructures variants having different subsurface microstructure and a thickness of 3 times the grain diameter are created in the spirit of Zeghadi et al. (2007a,b). For a very heterogeneous response (caused by a strong percolation of the phases, *e.g.* for higher martensite content), an even thicker

microstructure might be needed. However, for the additional subsurface microstructure further away, consideration of only the phase distribution and not the orientation of the individual grains introduces sufficient accuracy. This allows using a fast isotropic material model. The results of the stress and strain partitioning averaged over all variants finally allow obtaining a microstructure–property relationship that is statistically representative for regions with similar features like the ROI.

3.2.3 Pattern Formation in Polycrystalline Ice under Cyclic Loading

As discussed in section 3.1.2, collaborative phenomena, *i.e.* strain localisation/shear bands ranging over several grains, are widely observed in polycrystalline materials. The macroscopic behaviour of single-phase polycrystalline aggregates is significantly influenced by these phenomena. It is known that the formation is strongly influenced by the local microstructure and the imposed local stress and strain state. In the case of dynamic loading, *i.e.* when heat distribution is slow compared to the mechanical loading, the zones that—for whatever initial reason—deform slightly more, soften due to the locally generated heat and in turn continue to deform even more (Guduru et al., 2001). In controlled experiments, following Kalthoff et al. (1988), a notch can play the role of the initial strongly deforming zone. The conditions for the formation of the strain localisation in undamaged microstructures and for slow deformation velocities are more difficult to investigate and are subject of the following study. As it will be shown here, significant deformation patterning can also be observed in the case of isothermal, cyclic loading of a polycrystalline material.

The challenges in understanding shear bands are closely related to difficulties in developing well-designed experiments. More precisely, systematic experimental studies where only one parameter, *e.g.* in-grain-scatter, overall texture, loading rate, etc., is varied, are difficult to perform and (semi-)analytical solutions are not able to capture the anisotropy inherent to polycyrstalline materials (Coleman et al., 1985). For this reasons, localisation effects are a common playground for mechanical simulations:

- Li et al. (2000) used a mesh-free method to study the effect of voids on shear localisation with an isotropic material model.
- Jia et al. (2012a,b) performed systematic studies on simplified structures. In addition to CP formulations, a constitutive law originally developed for metallic glasses was used, since shear banding is their primary deformation mechanism.
- Standard CP was used by Sluys et al. (2000).
- Rezvanian et al. (2006) used a dislocation density based model.

All these simulations are using either a simplified material model or a rather small aggregate and hence where not able to capture localisation evolving situations similar to the real, polycrystalline state. This is due to the fact that the performance of the used simulation techniques (*i.e.* usually FEM) does not allow the simulation of large

aggregates in combination with complex material models that are needed. Hence, the capabilities of the spectral method are perfectly suited to perform systematic studies on the evolution of shear bands.

A prominent example of large localisation phenomena is the Jupiter moon Europa. The mechanical loading of the moon's surface is motivation for the presented work.

Surface Structure and Conditions of Jupiter Moon Europa

Europa is one of the several moons of Jupiter. It belongs to the group of the large Galilean moons and with a diameter of 3120 km is of similar size like Earth's moon (Greeley et al., 1998a). Surface temperatures on Europa can fall below 76 K during night and might reach 132 K during day. In the higher albedo[1] areas of ice, only up to 110 K can be expected during day.

Europa's core consists of stone or metal, and is separated by either ice at temperatures above the surface temperature or liquid water (Greeley et al., 1998a) from the outer layer of cold water ice. The stresses acting on this outer shell caused by tides are outlined by Greenberg et al. (1998) and Kattenhorn (2002) and will be used in a simplified form for the simulation that is given later on. These stresses are believed to cause—or at least to contribute to—the development of surface features observed on Europa (see fig. 3.32). The formation of the observed localisation phenomena is discussed by Hoppa et al. (1999). According to Greeley et al. (1998b) and Kattenhorn (2002) cracking or fracture is indicated from pictures taken by the Galileo spacecraft. However, as the mentioned studies show, the reasons for the evolution of the bands are not purely mechanical but also the activity of the core might play a role (Greeley et al., 1998a) (see also Bierhaus et al., 2005 for a discussion on craters on Europa). Thus, CP simulation on the ice shell on Europa can only be a simplification of the real circumstances that, however, might give hints on the development of the observed bands at the level of individual grains. Figure 3.32 shows the focus of this study, *i.e.* it is based on the assumption that the localisation phenomena raise from the scale of several grains to form features that span over the whole moon

Lattice Structure of Water Ice

Extrapolation of fig. 3.33 shows that for the conditions on Europa (0.1 µPa, 76 K to 110 K see McGrath et al., 2009 and Carlson et al., 2009) out of the 15 known solid phases for water ice, the hex I_h and the cubic I_c structure might exist. Experimental results indicate the nucleation of cubic ice in pure water and acidic solutions at low pressures (Murray, 2008; Murray et al., 2006). However, molecular dynamics simulations (Moore et al., 2011) and recent experiments (Malkin et al., 2012) show that the so called cubic ice also contains high fractions of the (stable) hex phase. From the mixture of the two phases Thurmer et al. (2013) conclude that even at temperatures below 170 K I_h is the stable phase—despite the fact that it has never be observed at

1 Albedo is the reflection coefficient or "whitness".

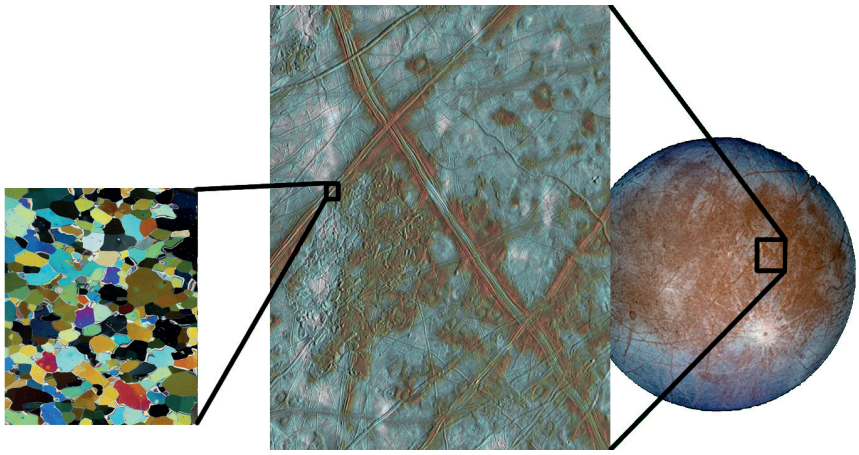

Figure 3.32: Focus of the study in comparison to the Jupiter moon Europa. For copyright information see appendix C.

these conditions—and I_c will eventually transform to I_h. Although some uncertainty remains, following Carlson et al. (2009) the assumption of a hex structure (probably following a phase transformation after some decades) seems to be reasonable for the ice found on Europa's surface[1].

Modelling Details

As outlined before, the ice on Europa is assumed to exist in the hex I_h structure. Values for the elastic constants of hex ice depending on the temperature are given for 133.15 K to 273.15 K by Dantl (1968). More accurate measurements based on Brillouin spectroscopy were done by Gammon et al. (1983) at 257.15 K. Parameswaran (1987) combined the two datasets to derive a formula for temperature dependent moduli which is valid from 77 K to 273.15 K. The c/a ratio of the hex structure is close to the value of 1.633 for a closely packed structure (1.628 according to Montagnat et al., 2013; 1.629 according to Michel, 1978). It should be emphasised, even though I_h ice is not a metallic hex structure but rather consists of Hydrogen and Oxygen, the assumption of a hex structure deforming by slip is frequently used in modelling (Montagnat et al., 2013). According to Montagnat et al. (2013) plastic deformation of ice in the range of possible strain rates ($1 \times 10^{-12}\,\mathrm{s}^{-1}$ to $1 \times 10^{-6}\,\mathrm{s}^{-1}$) is due to ductile dislocation creep. The following slip systems are taken into account: 3 basal $\{0\,0\,0\,1\}\langle 1\,1\,\bar{2}\,0\rangle$, 3 prismatic $\{0\,1\,\bar{1}\,0\}\langle 2\,\bar{1}\,\bar{1}\,0\rangle$, and 6 pyramidal $\{1\,1\,\bar{2}\,2\}\langle 1\,1\,\bar{2}\,\bar{3}\rangle$. Twinning is usually not observed in ice and hence not modelled. The employed parameters for the phenomenological

1 Dropping the idea discussed in NASA Space Science News (1999) that hex ice is an indicator for a past warmer period on Europa.

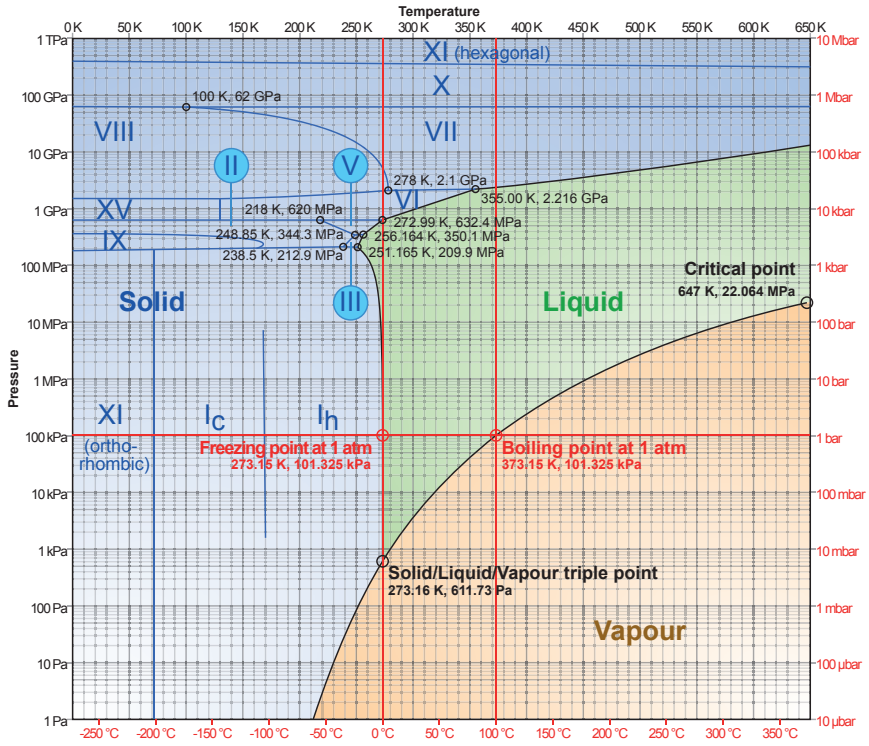

Figure 3.33: Phase diagram of water.

material model are given in table 3.7. The simulation is performed using the LAGRANGE multiplier field-based scheme.

A model microstructures consisting of 400 grains is created using a standard VORONOI tessellation approach on a 1000×1000 pixel 2D VE. The modelling as a 2D microstructure was chosen to reflect the "thin shell" character of the outer ice shell on Europa that is floating on a softer zone as outlined in section 3.2.3. Similar to the basal texture of hex Mg in the study on strain localisation in magnesium, a strong basal texture is assumed. More specific, a fiber-texture with a half-width scatter of 15° is selected. The c-axis is aligned with the third (periodically repeated) dimension of the columnar grains and the rotation around this axis is randomly chosen for each grain, *i.e.* it will undergo severe re-orientation during loading since the c-axis tend to align with the (changing) loading direction. In addition, an in-grain scatter of 3° is added randomly to all points. The IPF of the microstructure is shown in fig. 3.34.

The loading is chosen, such that during one tidal cycle a strain of 10 % is reached. Therefore, a uniaxial strain rate of $6.52 \times 10^{-7}\,\mathrm{s}^{-1}$ was applied for 153 400 s, followed by a change of direction. The applied deformation gradient rates read as:

$$\dot{\boldsymbol{F}}_1 = \begin{bmatrix} 6.52 \times 10^{-7} & 0.00 & 0.00 \\ 0.00 & * & 0.00 \\ 0.00 & 0.00 & 0.00 \end{bmatrix}, \dot{\boldsymbol{F}}_2 = \begin{bmatrix} * & 0.00 & 0.00 \\ 0.00 & 6.52 \times 10^{-7} & 0.00 \\ 0.00 & 0.00 & 0.00 \end{bmatrix}$$

where the asterisk "$*$" indicates a stress free component for $\boldsymbol{P}$. The loading was applied in 8 cycles, *i.e.* the microstructure was deformed to 10 % strain in horizontal direction, followed by a loading in vertical direction that approximately restores the initial quadratic shape eight times.

Results and Discussion

Despite the simple se-tup and the isothermal modelling approach, the cyclic loading results in a strong strain localisation. In fig. 3.35 $\varepsilon_{\mathrm{vM}}$ is shown at maximum strain in initial horizontal loading direction for the 8 simulated cycles. The figures show that with increasing cycle number the strain pattern becomes stronger. The regions of high strains are confined, while areas with low strain form long bands that might be characterised as "negative" shear bands. In connection with the strain patterning, a significant out-of-plane deformation is observed (not visible in the figure). Note that due to the selected BCs, out-of-plane deformation is only prohibited on average, but might exist locally.

In a plot similar to fig. 3.35, fig. 3.36 shows the sum of the slip on all 12 fcc slip systems evolving with the cyclic loading. In contrast to $\varepsilon_{\mathrm{vM}}$, which can go back to zero, this quantity is monotonically increasing over loading in x and y direction by virtue of the chosen plasticity model. A patterning can also be observed in fig. 3.36. However, comparing both figures, fig. 3.35 and fig. 3.36, clearly shows that the regions of high $\varepsilon_{\mathrm{vM}}$ and of high shear in general do not coincide. The different behaviour is investigated in more detail in a region located at the upper left corner of the microstructure shown in fig. 3.37a, where two positions are selected: Position 1, having a high total shear

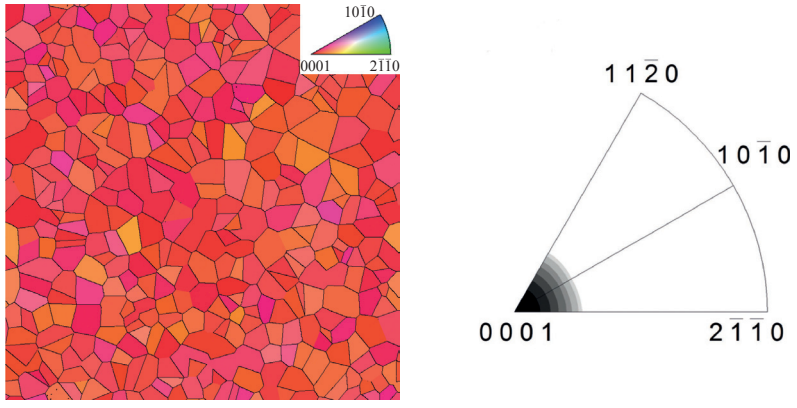

Figure 3.34: IPF of the ice microstructure || to observation plane 3. Initial loading is in horizontal direction 1.

Table 3.7: Material parameters for hexagonal ice.

(a) Elastic properties.

Property	Value	Unit
C_{11}	16.1×10^9	Pa
C_{33}	17.2×10^9	Pa
C_{44}	3.4×10^9	Pa
C_{12}	8.4×10^9	Pa
C_{13}	7.2×10^9	Pa

(b) Dislocation slip.

Property	Value	Unit
$\xi_{0,\mathrm{basal}}$	11.0×10^6	Pa
$\xi_{\infty,\mathrm{basal}}$	13.0×10^6	Pa
$\xi_{0,\mathrm{prism}}$	297.0×10^6	Pa
$\xi_{\infty,\mathrm{prism}}$	310.0×10^6	Pa
$\xi_{0,\mathrm{pyr}}$	429.0×10^6	Pa
$\xi_{\infty,\mathrm{pyr}}$	440.0×10^6	Pa

but low $\varepsilon_{\mathrm{vM}}$, and position 2, showing the opposite behaviour. The evolution of both quantities over the cycles is given in in fig. 3.37b. In this plot it can be seen that the evolution in position 1 follows the cycles, particularly $\varepsilon_{\mathrm{vM}}$ is increasing and decreasing with the cyclic loading and the total shear is growing more or less rapidly with the cycles. Position 2 does not show such a behaviour. Both quantities are growing independent of the loading directing, but $\varepsilon_{\mathrm{vM}}$ faster than in position 1 and the total shear at a lower rate. This indicates that position 1 is in a crystallographic more favorable orientation for in-plane deformation than position 2. As a result, $\varepsilon_{\mathrm{vM}}$ follows the loading back and forth, causing high slip activity. In contrast, position 2 is initially strained to a higher level, and with fewer shear is able to compensate the applied strain and maintain this high level of equivalent shear.

In summary, the results show that even a rather simple, isothermal model can predict complex pattern formation. To see this behaviour, a high resolution, a large number of differently oriented grains, and cyclic loading seem to be beneficial. Since this requires fine spatial and time resolution, the spectral solver is especially well suited to tackle the question of shear band initiation. Future simulations using the presented approach can be used to study in detail the effects of grain shape and size distribution as discussed in section 3.2.1, the initial fiber texture scatter, the initial in-grain orientation scatter, and the loading amplitude on the observed patterning. However, the use of the simple phenomenological material model for cyclic loading should be critically scrutinised. Specifically, the assumption of monotonous hardening is physically not justified and its influence on the pattern formation is not clear yet. After selecting a constitutive description with proven suitability, the planned implementation of thermo-mechanical coupling into DAMASK will enable investigating the differences between adiabatic shear bands and the pattern formation observed here.

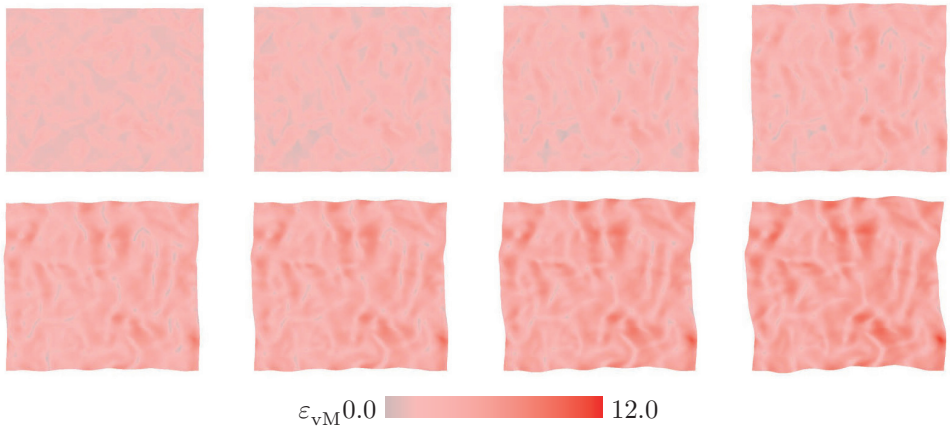

Figure 3.35: $\varepsilon_{\mathrm{vM}}$ at 10 % strain in horizontal direction for cycle 1…8 from upper left to lower right.

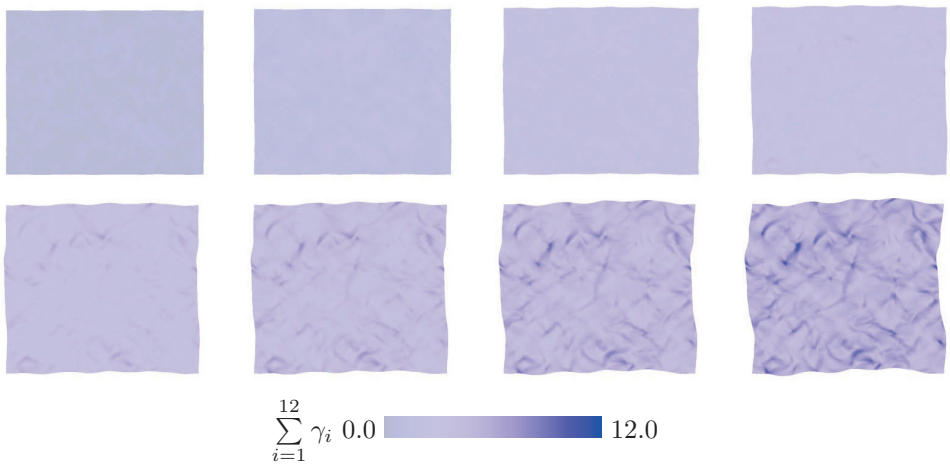

Figure 3.36: Sum of the total shear at 10 % strain in horizontal direction for cycle 1…8 from upper left to lower right.

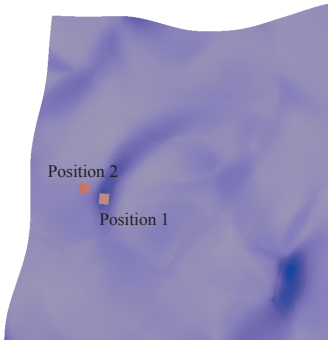

(a) ROIs, showing $\varepsilon_{\mathrm{vM}}$. The surrounding is colored according to the sum of the total shear. For color interpretation see figs. 3.35 and 3.36.

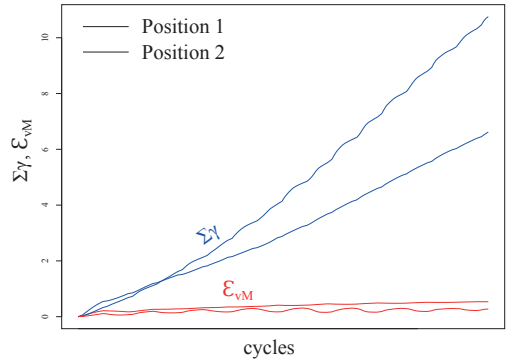

(b) Sum of the total shear and $\varepsilon_{\mathrm{vM}}$ shown for both positions.

Figure 3.37: Selected ROIs on the ice microstructure.

4 Summary and Outlook

In this thesis it is outlined on several examples, how the application of crystal plasticity (CP) simulations helps to understand the micro-mechanical behaviour of crystalline materials. Special focus is laid on exploiting the capabilities of the CP approach when applied to highly resolved microstructures, which is enabled by a fast and efficient spectral solver (see section 2.3). The improved performance of this numerical approach when using alternatives to the original fixed-point solution scheme allows increasing the resolution of the microstructures beyond typical values (see, *e.g.*, Herrera-Solaz et al., 2014) to gain a more detailed view on grain level mechanics. It also enables the spectral approach to handle heterogeneous materials with large contrast in stiffness (or strength) and gives the opportunity to tackle the simulation of, *e.g.*, dual phase (DP) steels. In the following, the outcomes of the presented simulations are briefly summarised, followed by an outlook on future work that allows enlarging the possibilities of CP simulations further.

The coupled experimental–numerical analyses of DP steels and Magnesium (Mg) show that for highly resolved microstructure discretisations even the comparably simple phenomenological material model is able to predict a behaviour in good agreement with experimental observations. As shown in section 3.1 "*Real Microstructures*", a well-designed simulation series can complement experimental investigations to achieve a better understanding of the experimental results. In subsection 3.1.2 "*Strain Localisation in Magnesium*", the experimentally unobtainable data was the exact loading condition of the region of interest (ROI). The simulated results allows deducting the global and local stress state of the ROI, which finally enables to interpret the experimental observations on the shear band formation. The simulation of realistic DP steel microstructures in subsection 3.1.1 "*Strain and Stress Partitioning* in *Dual Phase Steel*" recall the complex interplay between crystallographic orientation, grain shape and phase distribution. As a result of these observations it can be concluded that a rather big volume element (VE) is required to serve as a representative volume element (RVE). The statistical analysis of the obtained data confirms, in agreement to the experimental observations that the spatial strain distribution is rather insensitive to the strain level but strongly depends on the neighbourhood. The investigation also reveals that the mechanical behaviour of the ferritic grains that depends on grain size, shape and orientation as well as on chemical composition and heat treatment, is more complex than expected and might be the key factor to tailor DP steel properties. In contrast, the sensitivity analysis regarding the influences of the strength of martensite reports its less pronounced influence on the stress and strain partitioning.

In subsection 3.2.2 "*Subsurface Effects in Simplified Dual Phase Steel*", the influence of the subsurface microstructure on the observed local stress and strain values on a

2D observation plane is investigated. The dependence of the region of influence on the strain heterogeneity that is coming from the mechanical contrast between ferrite and martensite is quantified. Comparing the differences in the observed behaviour when changing the underlying microstructure to the differences when using a significantly modified constitutive behaviour—as it was done for the martensitic phase in section 3.1.1—clearly shows that the details of the constitutive model have a weaker influence. This justifies the use of the fast phenomenological material model, although more physical correct CP formulations are available in the Düsseldorf advanced material simulation kit (DAMASK). An additional advantage of the phenomenological material model is the possibility to obtain the exact material parameters directly on the material of interest. As shown in section 3.1.1, this process is challenging even for a plain material point model and would require much more effort for complex models with a higher number of parameters.

The investigation in subsection 3.2.1 "*Comparison of Microstructure Generation Approaches*" proves that the use of the fast standard VORONOI tessellation does not introduce a strong bias on the observed stress and strain partitioning in single phase materials at the continuum level. Since the micro-mechanics of DP steels strongly depend on the phase distribution, it can be assumed that the standard VORONOI tessellation can also be used without restriction for CP simulations of DP steels. In combination with the good agreement of experimentally observed and simulated behaviour, this motivates to use artificial DP microstructures to predict the average response of different DP grades when an RVE is three dimensional and microstructure of sufficient size is used. The fast spectral solver is finally the key factor in exploiting these findings to set up a virtual laboratory to predict macroscopic properties—either of existing microstructures to replace time-consuming and expensive experimental investigation or of artificially designed microstructures to investigate guidelines for the design of improved alloys.

The investigation on surface structure and conditions of Jupiter moon Europa in section 3.2.3 shows that the phenomenological material model is even capable of predicting complex patterning phenomena. However, in the case of strain-path reversion, the results might be strongly biased by the unrealistic assumption of monotonous hardening and the soundness of the observed partitioning needs a closer inspection. This example outlines also that the successful interpretation of simulation results requires taking carefully into account the simplifications made in the simulation set-up to realistically estimate the prediction ability of the performed simulation. In this context, it is of big importance to realise that usually the weakest point in the simulation set-up determines its prediction quality. As an example, investigation of strain partitioning in complex materials using a 2D model on the one hand gives deep insight into the mechanisms leading to its macroscopic behaviour. On the other hand, the "weakest link" is the 2D assumption, which cannot be overcome by *e.g.*, using a better material point model.

A primary point of future work on improving DAMASK is the elimination of such "weakest links" by the incorporation of additional physical effects besides plasticity into the framework of CP. This includes temperature, damage and fracture, recrystallisation,

and phase transformation. The importance of these additional effects becomes clear when looking at the limitations of the DP modelling presented in subsection 3.1.1 "*Strain and Stress Partitioning* i*n Dual Phase Steel*". Initially, some grains have an austenitic lattice structure that is currently treated as martensite with good reason. The experimental observations also show early damage incidents that—even though they do not lead to fracture—strongly re-partition the strain. It can be assumed that these effects have a much higher impact on the predicted micro-mechanical behaviour than the use of improved material point models, like a dislocation density based model or the incorporation of non-SCHMID effects. Hence, the "weakest link" is not the description of plasticity, but rather the omission of the above mentioned further effects.

Since damage and/or the initialisation of recrystallisation is happening at the scale of—or even below—the material point level, it is outmost importance to prevent the simulation technique from introducing artefacts even at single computation points. In the context of the spectral solver, the current implementation needs to be improved by effectively filtering the artefacts associated with the GIBBS phenomenon for the successful implementation of such effects.

Altogether, the results show that DAMASK and especially the spectral solver enable to perform high-resolution CP simulations that help to understand micro-mechanics of crystalline materials. The direct takeover of data coming from measurements on regular grids allows an easy coupling from experimentally obtained microstructures. This renders the presented simulation approach perfectly suited for the simulation of highly resolved three dimensional data sets obtained with the help of advanced neutron diffraction devices or by serial sectioning analysis with a scanning electron microscope.

A Scheme of Notation

The scheme of notation mostly in accordance with Roters et al. (2010a) and here reproduced from this book. As a general scheme of notation, vectors are written as boldface lowercase letters (*e.g.* $\boldsymbol{a}$, $\boldsymbol{b}$), second-order tensors as boldface capital letters (*e.g.* $\boldsymbol{A}$, $\boldsymbol{B}$), and fourth-order tensors as blackboard-bold capital letters (*e.g.* $\mathbb{A}$, $\mathbb{B}$). For vectors and tensors, Cartesian components are denoted as, respectively, a_i, A_{ij} and A_{ijkl}. The action of a second-order tensor upon a vector is denoted as $\boldsymbol{A}\boldsymbol{b}$ (in components $A_{ij}b_j$, implicit summation over repeated indices is used unless specified otherwise) and that of a fourth-order tensor upon a second order tensor is designated as $\mathbb{A}\boldsymbol{B}$ ($A_{ijkl}B_{kl}$). The composition of two second-order tensors is denoted as $\boldsymbol{A}\boldsymbol{B}$ ($A_{ik}B_{kj}$). The tensor (or dyadic) product between two vectors is denoted as $\boldsymbol{a} \otimes \boldsymbol{b}$ ($a_i b_j$). All inner products are indicated by a single dot between the tensorial quantities of the same order, *e.g.*, $\boldsymbol{a} \cdot \boldsymbol{b}$ ($a_i b_i$) for vectors and $\boldsymbol{A} \cdot \boldsymbol{B}$ ($A_{ij}B_{ij}$) for second-order tensors. The cross-product of a second-order tensor $\boldsymbol{A}$ with a vector $\boldsymbol{a}$, denoted by $\boldsymbol{A} \times \boldsymbol{a}$, is a second-order tensor defined in components as $(\boldsymbol{A} \times \boldsymbol{a})_{ij} = A_{ik}\, a_l\, \epsilon_{lkj}$, where ϵ is the Levita–Civita permutation matrix. The transpose, $\boldsymbol{A}^{\mathrm{T}}$, of a tensor $\boldsymbol{A}$ is denoted by a superscript "T", and the inverse, $\boldsymbol{A}^{-1}$, by a superscript "-1". $||\boldsymbol{A}||_2$ and $||\boldsymbol{A}||_{\mathrm{F}}$ designate the spectral norm and Frobenius norm of matrix $\boldsymbol{A}$, respectively. Additional notation is introduced where required.

B DAMASK Performance

The performance of the DAMASK is presented here for a selected set of revisions, starting from revision 1439 (Apr. 17 2012) and ending with 3990 (Mar. 12. 2015). The total runtime (wall time) employing 1 or 2 threads and the memory consumption when running the polycrystal example provided with DAMASK at a resolution of 32 $\times$ 32 $\times$ 32 pixel is measured with the help of the Linux *time* command. Bechmarks are performed on an Intel Xeon E5-2687W processor with 3.10 GHz, running Ubuntu 14.0.2. Using the *taskset*, CPU cores with ID 1 or 1 and 3 are selected, for the 1 or 2 thread simulations, respectively. The sample consists of 20 grains with aluminium properties for the phenomenological material model. It is loaded in uniaxial tension at a rate of $1.0 \times 10^{-3}\,\mathrm{s}^{-1}$ for 70 s following the example load case provided with DAMASK. In contrast to the example load case, no results are written out to minimize the influence of storage device performance on the measured run time.

The compilers used are GNU fortran in version 4.9.2 and Intel Fortran 14.0.2. The fastest Fourier transform in the west (FFTW) is used in version 3.3.4. The portable, extensible toolkit for scientific computation (PETSc) is used in versions 3.3-p7, 3.4.5 (starting with DAMASK revision 2797), and 3.5.3 (starting with DAMASK revision 3477), respectively. Standard compiler optimisation and the GNU fortran compiler are used for all revisions but the last two, where the strongest optimisation was used for both compilers.

In order to compile DAMASK using GNU fortran in version 4.9.2, code of several revisions needed a slight modification to confirm with the standard checks imposed by the compiler. Additionally, the calculation of the convolution operator $\mathbb{\Gamma}$ was corrected in revisions before 1975.

The following configure options have been used:

- FFTW for PETSc version 3.3-p7 and 3.4.5:
  `--enable-shared --enable-threads --disable-fortran CC=gcc`
- PETSc version 3.3-p7 and 3.4.5:
  `--with-fc=gfortran --with-cc=gcc --with-cxx=g++ --with-mpi=0`
  `--with-c2html=0 --with-x=0 --with-ssl=0 --with-debugging=0`
  `COPTFLAGS=-O2 CXXOPTFLAGS=-O2 FOPTFLAGS=-O2`
- PETSc version 3.5.3 standard set-up:
  `--with-fc=gfortran --with-cc=gcc --with-cxx=g++`
  `--with-c2html=0 --with-x=0 --with-ssl=0 --with-debugging=0`

```
COPTFLAGS=-O2 CXXOPTFLAGS=-O2 FOPTFLAGS=-O2
--download-fftw --download-openmpi
```

- PETSc version 3.5.3 fast set-up GNU fortran:
```
--with-fc=gfortran --with-cc=gcc --with-cxx=g++
--with-c2html=0 --with-x=0 --with-ssl=0 --with-debugging=0
COPTFLAGS=-O3 CXXOPTFLAGS=-O3 FOPTFLAGS=-O3
--download-fftw --download-openmpi
```

- PETSc version 3.5.3 fast set-up Intel fortran:
```
--with-fc=ifort --with-cc=icc --with-cxx=icpc
--with-c2html=0 --with-x=0 --with-ssl=0 --with-debugging=0
COPTFLAGS=-O3 CXXOPTFLAGS=-O3 FOPTFLAGS=-O3
--download-fftw --download-openmpi
```

Table B.1: DAMASK revision history of selected changes with expected increase (+,++,+++) or decrease (-,--,---) of runtime performance.

revision	change	expected runtime influence
3961	changed intermediate configuration kinematics	-
3886	introduced intermediate configuration kinematics to jacobian	-
3869	introduced intermediate configuration	--
3709	switched integration order of $\boldsymbol{F}_\mathrm{e}\boldsymbol{F}_\mathrm{p}\boldsymbol{F}_\mathrm{i}$	+
3654	new decomposition $\boldsymbol{F}_\mathrm{e}\boldsymbol{F}_\mathrm{p}\boldsymbol{F}_\mathrm{i}$	-
3640	cleaner damage interface	+
3612	introduced intermediate configuration	-
3576	helper functions for multiphysics	+
3568	removed old temperature handling	+
3534	analytic tangent introduced	+++
3496	multipysics introduced	-
3484	new homogenization state	+
3460	changed to PETSc 3.5.x	
3436	stable new state	
3313	no Cauchy stress calculation (pullback)	+
3250	introduced new state structure	+
3020	introduced dummy homogenisation for direct CP simulations	+
3018	reduced function calling overhead for non-local models	+

continued ...

. . . continued

rev	change	expected influence
2890	wrong indices in tangents	- - -
2888	convergence check simplified	
2887	convergence settings in IP wise calculation	
2865	tangent of $\boldsymbol{L}_\mathrm{p}$ corrected	+
2802	"enums" in homogenisation	+
2799	changed to PETSc 3.4.x	
2753	introduced enumerators	+ +
2691	removed temperature integration	+
2682	removed dummy functions	+
2577	dynamic simulations introduced	
2366	isostrain homogenisation more complex	-
2283	added "public", "private", and "protected" statements	+
2223	min-max average instead of volume average for $\mathbb{D}$	
2215	reorganised CPFEM calculation modes	
2190	"p-intvec"	-
2144	more involved reading from files	
2136	corrected IP coordinate calculation	+
2127	hardening behaviour of phenomenological material model corrected	
2099	bypassing calls to CPFEM module	+
2093	added some "pure" statements	+
2088	non-SCHMID-behaviour	-
2085	introduced lattice structures (keyword comparison)	- - -
1916	improved handling of IP coordinate calculation	+
1871	introduced some "forall" statements	+
1862	simplified stress integration	+
1855	direct solver instead of doing matrix inversion	+ + +
1834	modified saturation behaviour of phenomenological material model	
1823	use of compressed geometry files	
1809	improved SCHMID matrix calculation	
1776	marked some variables as "protected"	+
1723	employing LAPACK for matrix inversion	+

continued . . .

. . . continued

rev	change	expected influence
1668	changed array order to be fast in Fortran	+
1643	modularisation of spectral solver	--
1540	further modularisation of elasticity	-
1534	using preprocessor to avoid dummy functions	+
1518	introduced state jump function	-
1490	introduced delta state functions	-

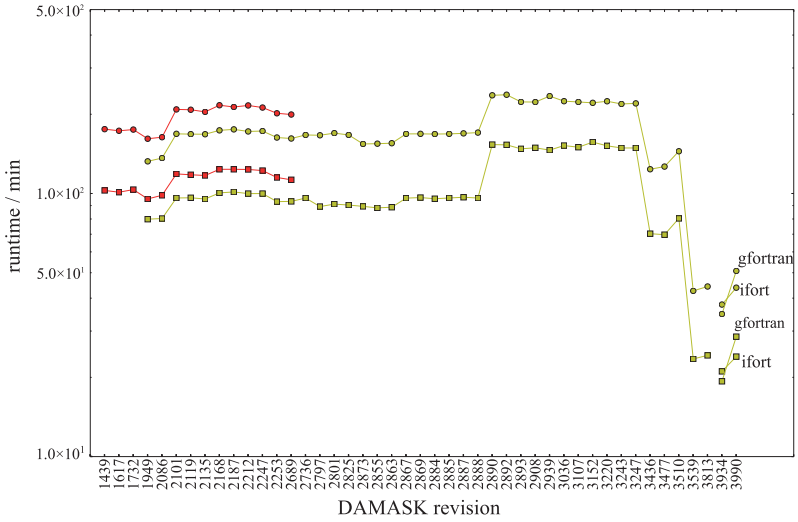

(a) Total runtime (Wall time) in minutes.

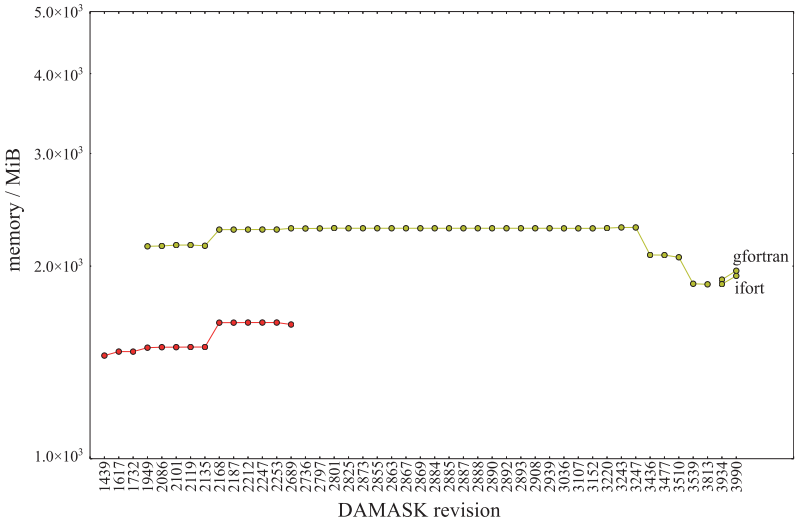

(b) Memory consumption in mebibyte.

Figure B.1: Performance of the direct variational formulation. Circles indicate one CPU, cubes two CPUs. Red color indicates the fixed-point without PETSc, green color the non-linear GMRES provided by PETSc. The two rightmost measurements are performed with heavily optimized code and comparing the Intel and the GNU fortran compiler.

C Copyright Information

Figure 2.1: Image uploaded by NICOGUARO to https://commons.wikimedia.org/wiki/File:Displacement_of_a_continuum.svg and licensed according to Creative Commons ShareAlike 3.0 Unported (http://creativecommons.org/licenses/by-sa/3.0). Modified to fit to variable convention.
Figure 3.33: Image uploaded by HOKANOMONO to https://en.wikipedia.org/wiki/Ice#mediaviewer/File:Phase_diagram_of_water.svg and licensed according to Creative Commons ShareAlike 3.0 Unported (http://creativecommons.org/licenses/by-sa/3.0).

Figure 3.32: Left: Courtesy of the CENTRE FOR ICE AND CLIMATE, NIELS BOHR INSTITUTE, UNIVERSITY OF COPENHAGEN. Right: "PIA03002: Blocks in the Europan Crust Provide More Evidence of Subterranean Ocean". Courtesy of the JET PROPULSION LABORATORY (JPL)/CALIFORNIA INSTITUTE OF TECHNOLOGY (Caltech).

Figure 2.2: In collaboration with the authors of Roters et al. (2010a) and published in similar form therein.

Figures 2.3, 2.8 and 2.10: In collaboration with the authors of Shanthraj et al. (2015) and published in similar form therein.

Figures 2.4 to 2.6: In collaboration with the authors of Eisenlohr et al. (2013) and published in similar form therein.

Figures 3.1, 3.3, 3.5 and 3.9 to 3.11: In collaboration with the authors of Tasan et al. (2014a) and published in similar form therein.

Figures 3.12 to 3.14: In collaboration with the authors of Wang et al. (2014) and published in similar form therein.

Figures 3.19 to 3.31: In collaboration with the authors of Diehl et al. (2015) and published in similar form therein.

Figures 2.7, 2.9, 3.2, 3.4, 3.6, 3.7, 3.15 to 3.18 and 3.34 to 3.36: First time published in this thesis.

D Abstract

Microstructures of metallic structural materials have become increasingly complex, incorporating typically more than one microstructural feature to adjust the material properties according to specific needs. To predict the behaviour of such complex materials, the underlying effects like interaction of different phases, hardening of slip systems, twinning, etc. have to be considered in order to produce applicable results. Usually, this is done with crystal plasticity simulations.

In this thesis the possibilities and capabilities of high-resolution crystal plasticity simulations are presented and discussed. Giving several examples, it is shown how the application of crystal plasticity simulations helps to understand the micro-mechanical behaviour of crystalline materials.

To avoid the high computational costs associated with crystal plasticity simulations that arise from (i) the evaluation of the selected constitutive law, and (ii) the solution of the associated mechanical boundary value problem, both contributions to the runtime have to be kept small. This is done by (i) employing a rather simple—and therefore fast—constitutive model, and by (ii) using an effective spectral method employing fast Fourier transforms for solving the partial differential equations describing the mechanical behaviour. While the spectral method based solvers show exponential convergence, their application is limited to volume elements with periodic boundary conditions. Here, an improved spectral solver incorporated into the Düsseldorf advanced material simulation kit (DAMASK) is used. The performance of this solver is critically discussed and the results are compared to results obtained with a commercial finite element solver. It is shown that the performance of the presented numerical approach allows increasing the resolution of the microstructures beyond typical values to gain a more detailed view on grain level mechanics. In contrast to simple, fixed-point based spectral solvers, the presented scheme is also able to handle heterogeneous materials with large contrast in stiffness (or strength) which gives the opportunity to tackle the simulation of, *e.g.*, dual phase steels.

Coupled experimental–numerical analyses performed on dual phase steel and magnesium microstructures prove that for highly resolved microstructure discretisations even a comparably simple phenomenological crystal plasticity model is able to predict behaviour in good agreement with experimental observations. Both simulation series complement the experimental investigations to achieve a better understanding of the experimental results. For the investigation on strain localisation in magnesium, the experimentally unobtainable data was the exact loading condition of the region of interest. The simulated results allow deducting the global and local stress state of the region of interest, which finally enables to interpret the experimental observations on the shear band formation. The simulation of realistic dual phase steel microstructures

recall the complex interplay between crystallographic orientation, grain shape and phase distribution. As a result of these observations it can be concluded that a rather big volume element is required to serve as a representative volume element. The investigation also reveals that the mechanical behaviour of the ferritic grains, which depends on grain size, shape and orientation as well as on chemical composition and heat treatment, is more complex than expected and might be the key factor to tailor dual phase steel properties. In contrast, the sensitivity analysis regarding the influences of the strength of martensite reports its less pronounced influence on the stress and strain partitioning.

The influence of the subsurface microstructure on the observed local stress and strain values on a 2D observation plane is investigated with the help of synthetic microstructures. The dependence of the region of influence on the strain heterogeneity coming from the mechanical contrast between ferrite and martensite is quantified. Comparing the differences in the observed behaviour when changing the underlying microstructure to the differences when using a significantly modified constitutive behaviour clearly shows that the details of the constitutive model have a weaker influence. This justifies the use of the fast phenomenological material point model, although physically more correct crystal plasticity formulations are available in DAMASK. A comparison of microstructure generation approaches proves that the use of the fast standard Voronoi tessellation does not introduce a strong bias on the observed stress and strain partitioning in single phase materials at the continuum level. It can be assumed that the standard Voronoi tessellation can also be used without restriction for crystal plasticity simulations. This motivates to use artificial microstructures to predict the average response of different material grades. The fast spectral solver is the key factor in exploiting these findings to set up a virtual laboratory to predict macroscopic properties—either of existing microstructures to replace time-consuming and expensive experimental investigation or of artificially designed microstructures to investigate guidelines for the design of improved alloys. The investigation on strain pattern formation in hexagonal water ice shows that the phenomenological material point model is even capable of predicting complex patterning phenomena. However, from a critical examination of the pattern formation it is deducted that the employed crystal plasticity model introduces artefacts when it is used in cyclic loading.

Altogether, in this thesis the possibilities and capabilities of high-resolution crystal plasticity simulations are presented and discussed. The simulations have been enabled by an advanced spectral method based solver. Using real and synthetic microstructures, a vast amount of micro-mechanical data is obtained that help to understand the mechanics of different crystalline materials.

E Zusammenfassung

Moderne metallische Strukturmaterialien haben komplexe Mikrostrukturen, da typischerweise eine Kombination verschiedener Mikrostrukturmechanismen dafür genutzt wird, um die gewünschten mechanischen Eigenschaften zu erreichen. Um das Verhalten solcher Materialien vorherzusagen, müssen daher Effekte wie die Interaktion verschiedener Phasen, das Verfestigen von einzelnen Gleitsystemen, mechanische Zwillingsbildung, usw. berücksichtigt werden um valide Vorhersagen treffen zu können. Dies geschieht üblicherweise mit der Hilfe von Kristallplastitzitätssimulationen.

In dieser Arbeit werden die Möglichkeiten und das Potential von hochaufgelösten Kristallplastizitätssimulationen präsentiert und diskutiert. An verschiedenen Beispielen wird gezeigt, wie die Anwendung von Kristallplastitizätsberechnungen zu einem verbesserten Verständnis der Mikromechanik von kristallinen Werkstoffen beitragen kann.

Um die Laufzeiten von Kristallplastizitätssimulationen, die von (i) der Auswertung des gewählten konstitutiven Gesetzes und (ii) der Lösung des dazugehörigen mechanischen Randwertproblems stammen, klein zu halten, werden beide Beiträge minimiert. Dies wird erreicht durch (i) das Verwenden eines relativ einfachen und schnellen Materialmodells und (ii) durch die Verwendung eine effizienten, auf schneller Fouriertransformation basierenden Spektralmethode zur Lösung der Gleichungen die das mechanische Verhalten beschreiben. Diese Methode zeigt ein exponentielles Konvergenzverhalten, ihre Anwendung ist aber auf Volumenelemente mit periodischen Randbedingungen beschränkt. Für die Simulationen wird eine Löser verwendet, der auf einer verbesserten Version dieser Methode basiert und in DAMASK (the Düsseldorf advanced material simulation kit) implementiert ist. Die Performance des Löser wird kritisch untersucht und die Ergebnisse werden mit denen eines kommerziellen Finite Elemente Methode Codes verglichen. Es wird gezeigt, wie die Fähigkeiten des verwendeten Ansatzes dazu benutzt werden können, Mikrostrukturen höher aufzulösen als es typischerweise üblich ist, was einen besseren Einblick in die Mikrostrukturmechanik erlaubt. Im Gegensatz zum einfachen, fixpunktbasierten Verfahren erlaubt es das präsentierte Verfahren außerdem, heterogene Materialien mit einem hohen mechanischen Kontrast in Steifigkeit oder Festigkeit zu simulieren und es kann daher genutzt werden, um z.B. Dualphasenstähle zu untersuchen.

Gekoppelte experimentell–numerische Untersuchungen von Dualphasenstahl- und Magnesium-Mikrostrukturen zeigen, dass für hochaufgelöste Mikrostrukturdiskretisierungen auch eine relative einfache, phenomenologische Kristallplastitzitätsbeschreibung in der Lage ist, die experimentellen Ergebnisse zu reproduzieren. Die Simulationsstudien ergänzen die experimentellen Untersuchungen und führen zu einem besseren Verständnis der experimentellen Ergebnisse. In der Untersuchung der Dehnungslokalisa-

tion in Magnesium ist es experimentell nicht möglich, den genauen Belastungszustand der untersuchten Region zu bestimmen. Die Simulation erlaubt es, auf die globale und lokale Spannung zu schließen, was es ermöglicht die experimentell beobachtete Entstehung eines Scherbandes zu verstehen. Simulationen von realen Dualphasenstahl-Mikrostrukturen zeigen, wie komplex die Interaktionen zwischen kristallographischer Orientierung, Korngestalt und Phasenverteilung ist. Aus den Beobachtungen kann geschlossen werden, dass ein relativ großes Volumen benötigt wird, um eine repräsentative Struktur abbilden zu können. Die Untersuchungen zeigen außerdem, dass das mechanische Verhalten der Ferrit-Körner, welche von Korngröße- und form, kristallographischer Orientierung ebenso wie von der chemischen Zusammensetzung und der Wärmebehandlung abhängt, komplexer ist als zuvor angenommen und möglicherweise ein großes Optimierungspotential bildet. Im Gegensatz dazu, zeigt eine Sensitivitätsanalyse bezüglich der Festigkeit des Martensits, dass dessen Verhalten einen relativ schwachen Einfluss auf die beobachtete Spannungs- und Dehnungsverteilung hat.

Der Einfluss der unterliegenden Mikrostruktur auf die Spannungs- und Dehnungsverteilung in einer 2D Beobachtungsebene ist mit Hilfe von künstlichen Mikrostrukturen untersucht. Aus dem Vergleich der Unterschiede in dem beobachteten Verhalten beim Verändern der darunterliegenden Mikrostruktur zu dem Verhalten bei einem geänderten konstitutiven Verhalten wird klar, dass eine Veränderung des Materialverhaltens einen deutlich geringen Einfluss auf das beobachtete Verhalten hat. Dies rechtfertigt die Benutzung des einfachen, aber schnellen phenomenologischen Modells anstatt der besseren, physikalisch korrekteren Modelle die ebenfalls in DAMASK implementiert sind. Der Vergleich zweier Methoden zur Mikrostrukturerzeugung zeigt, dass die schnelle und einfache Voronoi Tesselierung keinen entscheidenden Einfluss auf die berechnete Spannungs- und Dehnungsverteilung in einphasigen Materialien hat wenn eine Kontinuumsbeschreibung verwendet wird. Es kann angenommen werden, dass die Voronoi Tesselierung ohne Einschränkung für Kristallplastizitätssimulationen verwendet werden kann. Der schnelle Spektrallöser ist daher perfekt geeignet, um in einem virtuellen Labor die makroskopischen Eigenschaften von Materialien vorherzusagen, sei es als Ersatz für aufwändige mechanische Tests an bestehenden Mikrostrukturen oder um anhand von künstlichen Mikrostrukturen Richtlinien für verbesserte Legierungen zu entwickeln. Die Untersuchung von Dehnungsmustern in hexagonalem Wassereis zeigen, dass das phenomenologische Materialmodell sogar in der Lage ist, komplexe Musterbildung vorherzusagen. Allerdings zeigt eine kritische Diskussion der Ergebnisse, dass dieses Modell möglicherweise im Falle zyklischer Beanspruchung unphysikalische Vorhersagen macht.

In dieser Arbeit gezeigt welche Fähigkeiten und Möglichkeiten Kristallplastizitätssimulationen haben. Hochaufgelösten Simulationen werden durch einen schnellen Löser ermöglicht. Eine Unmenge mikromechanischer Daten, erzeugt an realen und synthetischen Mikrostrukturen ist dabei behilflich, das mechanische Verhalten kristalliner Werkstoffe zu verstehen.

Bibliography

Agnew, S. R., Yoo, M. H., and Tomé, C. N. (2001). 'Application of texture simulation to understanding mechanical behavior of Mg and solid solution alloys containing Li or Y'. In: *Acta Materialia* 49.20, pp. 4277–4289. ISSN: 1359-6454. DOI: 10.1016/S1359-6454(01)00297-X (cit. on p. 54).

Agnew, S. R., Brown, D., and Tomé, C. N. (2006). 'Validating a polycrystal model for the elastoplastic response of magnesium alloy AZ31 using in situ neutron diffraction'. In: *Acta Materialia* 54.18, pp. 4841–4852. ISSN: 1359-6454. DOI: 10.1016/j.actamat.2006.06.020 (cit. on pp. 56, 57).

Akhtar, A. and Teghtsoonian, E. (1969). 'Solid solution strengthening of magnesium single crystals – 1: alloying behaviour in basal slip'. In: *Acta Metallurgica* 17.11, pp. 1339–1349. ISSN: 0001-6160. DOI: 10.1016/0001-6160(69)90151-5 (cit. on p. 54).

Balay, S., Brown, J., Buschelman, K., Eijkhout, V., Gropp, W. D., Kaushik, D., Knepley, M. G., McInnes, L. C., Smith, B. F., et al. (2013). *PETSc Users Manual*. Tech. rep. (cit. on p. 23).

Barnett, M. R., Nave, M. D., and Bettles, C. J. (2004). 'Deformation microstructures and textures of some cold rolled Mg alloys'. In: *Materials Science and Engineering: A* 386.1-2, pp. 205–211. ISSN: 0921-5093. DOI: 10.1016/j.msea.2004.07.030 (cit. on p. 54).

Bathe, K-J (2002). *Finite-Elemente-Methoden*. 2nd ed. Berlin: Springer. ISBN: 3-540-66806-3 (cit. on p. 1).

Bierhaus, E. B., Chapman, C. R., and Merline, W. J. (2005). 'Secondary craters on Europa and implications for cratered surfaces'. In: *Nature* 437.7062, pp. 1125–1127. ISSN: 0028-0836. DOI: 10.1038/nature04069 (cit. on p. 81).

Bishop, J. F. W. and Hill, R. (1951). 'A theory of the plastic distortion of a polycrystalline aggregate under combined stresses'. In: *Philosophical Magazine* 42.327, pp. 414–427. ISSN: 1478-6435. DOI: 10.1080/14786445108561065 (cit. on p. 54).

Brisard, S. and Dormieux, L. (2010). 'FFT-based methods for the mechanics of composites: A general variational framework'. In: *Computational Materials Science* 49.3, pp. 663–671. ISSN: 0927-0256. DOI: 10.1016/j.commatsci.2010.06.009 (cit. on p. 16).

Cailletaud, G., Diard, O., Feyel, F., and Forest, S. (2003). 'Computational Crystal Plasticity: From Single Crystal to Homogenized Polycrystals'. In: *Technische Mechanik* 23.2-4, pp. 130–145. ISSN: 2199-9244 (cit. on p. 1).

Calcagnotto, M., Adachi, Y., Ponge, D., and Raabe, D. (2011). 'Deformation and fracture mechanisms in fine- and ultrafine-grained ferrite/martensite dual-phase

steels and the effect of aging'. In: *Acta Materialia* 59.2, pp. 658–670. ISSN: 1359-6454. DOI: 10.1016/j.actamat.2010.10.002 (cit. on pp. 51, 53).

Carlson, R. W., Calvin, W. M., Dalton, J. B., Hansen, G. B., Hudson, R. L., Johnson, R. E., McCord, T. B., and Moore, M. H. (2009). In: ed. by R. T. Pappalardo, W. B. McKinnon, and K. Khurana. Tucson: The University of Arizona Press. Chap. Europa's Surface Composition (cit. on pp. 81, 82).

Chen, L-Q (2002). 'Phase-field models for microstructure evolution'. In: *Annual Review of Materials Research* 32.1, pp. 113–140. ISSN: 1531-7331. DOI: 10.1146/annurev.matsci.32.112001.132041 (cit. on p. 62).

Chen, P., Ghassemi-Armaki, H., Kumar, S., Bower, A., Bhat, S., and Sadagopan, S. (2014). 'Microscale-calibrated modeling of the deformation response of dual-phase steels'. In: *Acta Materialia* 65, pp. 133–149. ISSN: 1359-6454. DOI: 10.1016/j.actamat.2013.11.036 (cit. on pp. 39, 67).

Chen, Y. and Shen, C. (2006). 'A Jacobian-Free Newton-GMRES(m) Method with Adaptive Preconditioner and Its Application for Power Flow Calculations'. In: *IEEE Transactions on Power Systems* 21.3, pp. 1096–1103. ISSN: 0885-8950. DOI: 10.1109/TPWRS.2006.876696 (cit. on p. 23).

Chun, Y. B. and Davies, C. H. J. (2012). 'Texture effects on development of shear bands in rolled AZ31 alloy'. In: *Materials Science and Engineering: A* 556, pp. 253–259. ISSN: 0921-5093. DOI: 10.1016/j.msea.2012.06.083 (cit. on p. 54).

Coleman, B. D. and Hodgdon, M. L. (1985). 'On shear bands in ductile materials'. In: *Archive for Rational Mechanics and Analysis* 90.3, pp. 219–247. ISSN: 0003-9527. DOI: 10.1007/BF00251732 (cit. on p. 80).

Dalla Torre, F., Van Swygenhoven, H., and Victoria, M. (2002). 'Nanocrystalline electrodeposited Ni: microstructure and tensile properties'. In: *Acta Materialia* 50.15, pp. 3957–3970. ISSN: 1359-6454. DOI: 10.1016/S1359-6454(02)00198-2 (cit. on p. 64).

Dantl, G. (1968). 'Die elastischen Moduln von Eis-Einkristallen'. In: *Physik der Kondensierten Materie* 7.5, pp. 390–397. ISSN: 1434-6028. DOI: 10.1007/BF02422784 (cit. on p. 82).

Diehl, M. (2010). 'A spectral method using fast Fourier transform to solve elasto-viscoplastic mechanical boundary value problems'. Diplom Thesis. München. DOI: 10.13140/2.1.3234.3840 (cit. on p. 4).

Diehl, M., Shanthraj, P., Eisenlohr, P., and Roters, F. (2015). 'Neighborhood influences on stress and strain partitioning in dual phase microstructures. An investigation on synthetic polycrystals with a robust spectral-based numerical method'. In: *Meccanica* (accepted). DOI: 10.1007/s11012-015-0281-2 (cit. on pp. 48, 50, 68, 101).

Eisenlohr, P., Diehl, M., Lebensohn, R. A., and Roters, F. (2013). 'A spectral method solution to crystal elasto-viscoplasticity at finite strains'. In: *International Journal of Plasticity* 46, pp. 37–53. ISSN: 0749-6419. DOI: 10.1016/j.ijplas.2012.09.012 (cit. on pp. 16, 17, 24, 27–29, 101).

Eisenstat, S. C. and Walker, H. F. (1996). 'Choosing the Forcing Terms in an Inexact Newton Method'. In: *SIAM Journal on Scientific Computing* 17.1, pp. 16–32. ISSN: 1095-7197. DOI: 10.1137/0917003 (cit. on p. 25).

Eyre, D. J. and Milton, G. W. (1999). 'A fast numerical scheme for computing the response of composites using grid refinement'. In: *European Physical Journal-Applied Physics* 6.1, pp. 41–47. ISSN: 1286-0042. DOI: 10.1051/epjap:1999150 (cit. on p. 16).

Fortin, M. and Glowinski, R., eds. (1983). *Augmented Lagrangian Methods: Applications to the Numerical Solution of Boundary-Value Problems*. ISBN: 9780444866806 (cit. on p. 20).

Frigo, M. and Johnson, S. G. (2005). 'The Design and Implementation of FFTW3'. In: *Proceedings of the IEEE* 93.2, pp. 216–231. ISSN: 0018-9219. DOI: 10.1109/JPROC.2004.840301 (cit. on p. 22).

Frigo, M. and Johnson, S. G. (2014). *FFTW*. URL: http://www.fftw.org (visited on 10/21/2014) (cit. on p. 22).

Gammon, P. H., Kiefte, H., Clouter, M. J., and Denner, W. W. (1983). 'Elastic constants of artificial and natural ice samples by Brillouin spectroscopy'. In: *Journal of Glaciology* 29, pp. 433–460. ISSN: 0022-1430 (cit. on p. 82).

Ghassemi-Armaki, H., Chen, P., Bhat, S., Sadagopan, S., Kumar, S., and Bower, A. (2013). 'Microscale-calibrated modeling of the deformation response of low-carbon martensite'. In: *Acta Materialia* 61.10, pp. 3640–3652. ISSN: 1359-6454. DOI: 10.1016/j.actamat.2013.02.051 (cit. on p. 52).

Ghassemi-Armaki, H., Maaß, R., Bhat, S. P., Sriram, S., Greer, J. R., and Kumar, K. S. (2014). 'Deformation response of ferrite and martensite in a dual-phase steel'. In: *Acta Materialia*, pp. 197–211. ISSN: 1359-6454. DOI: 10.1016/j.actamat.2013.10.001 (cit. on p. 39).

Gottstein, G. (2004). *Physical Foundations of Material Science*. Berlin: Springer. ISBN: 3-540-40139-3 (cit. on pp. 11, 15).

Gottstein, G. and Al-Samman, T. (2005). 'Texture Development in Pure Mg and Mg Alloy AZ31'. In: *Materials Science Forum* 495-497, pp. 623–632. ISSN: 1662-9752. DOI: 10.4028/www.scientific.net/MSF.495-497.623 (cit. on pp. 54, 57).

Greeley, R., Sullivan, R., Klemaszewski, J., Homan, K., J.W., Head, Pappalardo, R. T., Veverka, J., Clark, B. E., Johnson, T. V., et al. (1998a). 'Europa: Initial Galileo Geological Observations'. In: *Icarus* 135.1, pp. 4–24. ISSN: 0019-1035. DOI: 10.1006/icar.1998.5969 (cit. on p. 81).

Greeley, R., Sullivan, R., Coon, M. D., Geissler, P. E., Tufts, B. R., J.W., Head., Pappalardo, R. T., and Moore, J. M. (1998b). 'Terrestrial Sea Ice Morphology: Considerations for Europa'. In: *Icarus* 135.1, pp. 25–40. ISSN: 0019-1035. DOI: 10.1006/icar.1998.5977 (cit. on p. 81).

Greenberg, R., Geissler, P. E., Hoppa, G. V., Tufts, B. R., Durda, D. D., Pappalardo, R. T., Head, J. W., Greeley, R., Sullivan, R., et al. (1998). 'Tectonic Processes on Europa: Tidal Stresses, Mechanical Response, and Visible Features'. In: *Icarus* 135.1, pp. 64–78. ISSN: 0019-1035. DOI: 10.1006/icar.1998.5986 (cit. on p. 81).

Grennerat, F., Montagnat, M., Castelnau, O., Vacher, P., Moulinec, H., Suquet, P., and Duval, P. (2012). 'Experimental characterization of the intragranular strain field in columnar ice during transient creep'. In: *Acta Materialia* 60.8, pp. 3655–3666. ISSN: 1359-6454. DOI: 10.1016/j.actamat.2012.03.025 (cit. on p. 16).

Guduru, P. R., Rosakis, A. J., and Ravichandran, G. (2001). In: *Mechanics of Materials* 33, pp. 371–402. ISSN: 0167-6636 (cit. on p. 80).

Gutierrez-Urrutia, I., Zaefferer, S., and Raabe, D. (2013). 'Coupling of electron channeling with EBSD: Toward the quantitative characterization of deformation structures in the SEM'. In: *JOM* 65.9, pp. 1229–1236. ISSN: 1047-4838. DOI: 10.1007/s11837-013-0678-0 (cit. on p. 57).

Hazeli, K., Cuadra, J., Vanniamparambil, P. A., and Kontsos, A. (2013). 'In situ identification of twin-related bands near yielding in a magnesium alloy'. In: *Scripta Materialia* 68.1, pp. 83–86. ISSN: 1359-6462. DOI: 10.1016/j.scriptamat.2012.09.009 (cit. on p. 54).

Herrera-Solaz, V., LLorca, J., Dogan, E., Karaman, I., and Segurado, J. (2014). 'An inverse optimization strategy to determine single crystal mechanical behavior from polycrystal tests: Application to AZ31 Mg alloy'. In: *International Journal of Plasticity* 57, pp. 1–15. ISSN: 0749-6419. DOI: 10.1016/j.ijplas.2014.02.001 (cit. on p. 89).

Hoppa, G. V., Tufts, B. R., Greenberg, R., and Geissler, P. E. (1999). 'Formation of Cycloidal Features on Europa'. In: *Science* 285.5435, pp. 1899–1902. ISSN: 0036-8075. DOI: 10.1126/science.285.5435.1899 (cit. on p. 81).

Humphreys, F. J. and Hatherly, M. (2004). *Recrystallization and Related Annealing Phenomena*. Elsevier. ISBN: 978-0-08-044164-1 (cit. on pp. 54, 57).

Hutchinson, J. W. (1976). 'Bounds and Self-Consistent Estimates for Creep of Polycrystalline Materials'. In: *Proceedings of the Royal Society A* 348, pp. 101–127. ISSN: 1364-5021. DOI: 10.1098/rspa.1976.0027 (cit. on p. 15).

Ion, S. E., Humphreys, F. J., and White, S. H. (1982). 'Dynamic recrystallisation and the development of microstructure during the high temperature deformation of magnesium'. In: *Acta Metallurgica* 30.10, pp. 1909–1919. ISSN: 0001-6160. DOI: 10.1016/0001-6160(82)90031-1 (cit. on p. 54).

Jia, N., Roters, F., Eisenlohr, P., Kords, C., and Raabe, D. (2012a). 'Non-crystallographic shear banding in crystal plasticity FEM simulations: Example of texture evolution in α-brass'. In: *Acta Materialia* 60.3, pp. 1099–1115. ISSN: 1359-6454. DOI: 10.1016/j.actamat.2011.10.047 (cit. on p. 80).

Jia, N., Eisenlohr, P., Roters, F., Raabe, D., and Zhao, X. (2012b). 'Orientation dependence of shear banding in face-centered-cubic single crystals'. In: *Acta Materialia* 60.8, pp. 3415–3434. ISSN: 1359-6454. DOI: 10.1016/j.actamat.2012.03.005 (cit. on p. 80).

Kalidindi, S. R. (1998). 'Incorporation of deformation twinning in crystal plasticity models'. In: *Journal of the Mechanics and Physics of Solids* 46.2, pp. 267–271. ISSN: 0022-5096. DOI: 10.1016/S0022-5096(97)00051-3 (cit. on p. 55).

Kalthoff, J. F. and Winkler, S. (1988). 'Impact Loading and Dynamic Behaviour of Materials'. In: ed. by C. Y. Chiem, Kunze H.-D., and Meyer L.W. Ir Pubns Ltd. Chap. Failure mode transition at high rates of shear loading. ISBN: 978-0318379463 (cit. on p. 80).

Kanjarla, A. K., Lebensohn, R. A., Balogh, L., and Tomé, C. N. (2012). 'Study of internal lattice strain distributions in stainless steel using a full-field elasto-

viscoplastic formulation based on fast Fourier transforms'. In: *Acta Materialia* 60.6-7, pp. 3094–3106. ISSN: 1359-6454. DOI: 10.1016/j.actamat.2012.02.014 (cit. on p. 16).

Karlsson, B. and Sundström, B. O. (1974). 'Inhomogeneity in plastic deformation of two-phase steels'. In: *Materials Science and Engineering* 16.1-2, pp. 161–168. ISSN: 0025-5416. DOI: 10.1016/0025-5416(74)90150-5 (cit. on p. 37).

Kattenhorn, S. A. (2002). 'Nonsynchronous Rotation Evidence and Fracture History in the Bright Plains Region, Europa'. In: *Icarus* 157.2, pp. 490–506. ISSN: 0019-1035. DOI: 10.1006/icar.2002.6825 (cit. on p. 81).

Kelley, C. T. (1995). *Iterative Methods for Linear and Nonlinear Equations*. Vol. 16. Frontiers in Applied Mathematics. Philadelphia, PA, USA: Society for Industrial and Applied Mathematics. ISBN: 978-0-898713-52-7. URL: www.siam.org/books/textbooks/fr16_book.pdf (cit. on pp. 23, 33).

Kennel, M. B. (2004). 'KDTREE 2: Fortran 95 and C++ software to efficiently search for near neighbors in a multi-dimensional Euclidean space'. In: *arXiv*. URL: http://arxiv.org/abs/physics/0408067v2 (cit. on p. 61).

Kim, H. L., Lee, J-H, Lee, C. S., Bang, W., Ahn, S. H., and Chang, Y. W. (2012). 'Shear band formation during hot compression of AZ31 Mg alloy sheets'. In: *Materials Science and Engineering: A* 558, pp. 431–438. ISSN: 0921-5093. DOI: 10.1016/j.msea.2012.08.023 (cit. on p. 54).

Kords, C. (2013). 'On the role of dislocation transport in the constitutive description of crystal plasticity'. PhD thesis. Berlin: epubli GmbH. ISBN: 978-3-8442-7741-8. URL: http://darwin.bth.rwth-aachen.de/opus3/volltexte/2014/4862/ (cit. on p. 13).

Krill III, C. E. and Chen, L-Q (2002). 'Computer simulation of 3-D grain growth using a phase-field model'. In: *Acta Materialia* 50.12, pp. 3059–3075. ISSN: 1359-6454. DOI: 10.1016/S1359-6454(02)00084-8 (cit. on p. 62).

Kumar, S., Kurtz, S. K., Banavar, J. R., and Sharma, M. G. (1992). 'Properties of a three-dimensional Poisson-Voronoi tesselation: A Monte Carlo study'. In: *Journal of Statistical Physics* 67.3-4, pp. 523–551. ISSN: 0022-4715. DOI: 10.1007/BF01049719 (cit. on p. 64).

Lahellec, N., Michel, J. C., Moulinec, H., and Suquet, P. (2001). 'Analysis of inhomogeneous materials at large strains using fast Fourier transforms'. In: *IUTAM Symposium on Computational Mechanics of Solid Materials at Large Strains*. Ed. by C. Miehe. Vol. 108. Solid Mechanics and its Applications. Dordrecht, The Netherlands: Kluwer Academic Publishers, pp. 247–258. ISBN: 978-90-481-6239-0. DOI: 10.1007/978-94-017-0297-3_22 (cit. on pp. 16, 17, 24).

Landron, C., Bouaziz, O., Maire, E., and Adrien, J. (2013). 'Experimental investigation of void coalescence in a dual phase steel using X-ray tomography'. In: *Acta Materialia* 61.18, pp. 6821–6829. ISSN: 1359-6454. DOI: 10.1016/j.actamat.2013.07.058 (cit. on p. 67).

Lebensohn, R. A. (2001). 'N-site modeling of a 3D viscoplastic polycrystal using Fast Fourier Transform'. In: *Acta Materialia* 49.14, pp. 2723–2737. ISSN: 1359-6454. DOI: 10.1016/S1359-6454(01)00172-0 (cit. on p. 16).

Lebensohn, R. A., Castelnau, O., Brenner, R., and Gilormini, P. (2005). 'Study of the antiplane deformation of linear 2-D polycrystals with different microstructures'. In: *International Journal of Solids and Structures* 42.20, pp. 5441–5459. ISSN: 0020-7683. DOI: 10.1016/j.ijsolstr.2005.02.051 (cit. on p. 16).

Lebensohn, R. A., Idiart, M. I., Castañeda, P. P., and Vincent, P-G (2011). 'Dilatational viscoplasticity of polycrystalline solids with intergranular cavities'. In: *Philosophical Magazine* 91.22, pp. 3038–3067. ISSN: 1478-6435. DOI: 10.1080/14786435.2011.561811 (cit. on p. 16).

Lebensohn, R. A., Kanjarla, A. K., and Eisenlohr, P. (2012). 'An elasto-viscoplastic formulation based on fast Fourier transforms for the prediction of micromechanical fields in polycrystalline materials'. In: *International Journal of Plasticity* 32-33, pp. 59–69. ISSN: 0749-6419. DOI: 10.1016/j.ijplas.2011.12.005 (cit. on p. 16).

Lee, S-B, Lebensohn, R. A., and Rollett, A. D. (2011). 'Modeling the viscoplastic micromechanical response of two-phase materials using Fast Fourier Transforms'. In: *International Journal of Plasticity* 27.5, pp. 707–727. ISSN: 0749-6419. DOI: 10.1016/j.ijplas.2010.09.002 (cit. on p. 16).

Lefebvre, G., Sinclair, C. W., Lebensohn, R. A., and Mithieux, J-D (2012). 'Accounting for local interactions in the prediction of roping of ferritic stainless steel sheets'. In: *Modelling and Simulation in Materials Science and Engineering* 20.2, p. 024008. ISSN: 0965-0393. DOI: 10.1088/0965-0393/20/2/024008 (cit. on p. 16).

Li, S., Hao, W., and Liu, W. K. (2000). 'Mesh-free simulations of shear banding in large deformation'. In: *International Journal of Solids and Structures* 37.48-50, pp. 7185–7206. ISSN: 0020-7683. DOI: 10.1016/S0020-7683(00)00195-5 (cit. on p. 80).

Lyckegaard, A., Lauridsen, E. M., Ludwig, W., Fonda, R. W., and Poulsen, H. F. (2011). 'On the Use of Laguerre Tessellations for Representations of 3D Grain Structures'. In: *Advanced Engineering Materials* 13.3, pp. 165–170. ISSN: 1438-1656. DOI: 10.1002/adem.201000258 (cit. on p. 62).

Malkin, T. L., Murray, B. J., Brukhno, A. V., Anwar, J., and Salzmann, C. G. (2012). 'Structure of ice crystallized from supercooled water'. In: *Proceedings of the National Academy of Sciences* 109.4, pp. 1041–1045. ISSN: 0027-8424. DOI: 10.1073/pnas.1113059109 (cit. on p. 81).

Maresca, F., Kouznetsova, V. G., and Geers, M. G. D. (2014). 'Subgrain lath martensite mechanics: A numerical–experimental analysis'. In: *Journal of the Mechanics and Physics of Solids* 73, pp. 69–83. ISSN: 0022-5096. DOI: 10.1016/j.jmps.2014.09.002 (cit. on p. 37).

McGinty, B. (2015). *Continuum Mechanics*. URL: http://www.continuummechanics.org (visited on 01/15/2015) (cit. on pp. 4, 6).

McGrath, M. A., Hansen, C. J., and Hendrix, A. R. (2009). In: ed. by R. T. Pappalardo, W. B. McKinnon, and K. Khurana. The University of Arizona Press. Chap. Observations of Europa's Atmosphere, pp. 485–506 (cit. on p. 81).

Meijering, J. L. (1953). 'Interface area, edge length, and number of vertices in crystal aggregates with random nucleation'. In: *Philips Research Reports* 8, pp. 270–290 (cit. on p. 64).

Michel, B. (1978). *Ice Mechanics*. Quebec: Les Presse de l'Universite Laval. ISBN: 0-7746-6876-8 (cit. on p. 82).

Michel, J. C., Moulinec, H., and Suquet, P. (2000). 'A computational method based on augmented Lagrangians and fast Fourier Transforms for composites with high contrast'. In: *Computer Modeling in Engineering & Sciences* 1.2, pp. 79–88. ISSN: 1526-1492. DOI: 10.3970/cmes.2000.001.239 (cit. on p. 19).

Michel, J. C., Moulinec, H., and Suquet, P. (2001). 'A computational scheme for linear and non-linear composites with arbitrary phase contrast'. In: *International Journal for Numerical Methods in Engineering* 52.12, pp. 139–160. ISSN: 0029-5981. DOI: 10.1002/nme.275 (cit. on pp. 16, 22, 32, 33).

Monchiet, V. and Bonnet, G. (2012). 'A polarization-based FFT iterative scheme for computing the effective properties of elastic composites with arbitrary contrast'. In: *International Journal for Numerical Methods in Engineering* 89.11, pp. 1419–1436. ISSN: 0029-5981. DOI: 10.1002/nme.3295 (cit. on pp. 16, 20, 24, 32).

Montagnat, M., Castelnau, O., Bons, P. D., Faria, S. H., Gagliardini, O., Gillet-Chaulet, F., Grennerat, F., Griera, A., Lebensohn, R. A., et al. (2013). 'Multiscale modeling of ice deformation behavior'. In: *Journal of Structural Geology*. ISSN: 0191-8141. DOI: 10.1016/j.jsg.2013.05.002 (cit. on p. 82).

Moore, E. B. and Molinero, V. (2011). 'Is it cubic? Ice crystallization from deeply supercooled water'. In: *Physical Chemistry Chemical Physics* 13.44, pp. 20008–20016. ISSN: 1463-9076. DOI: 10.1039/C1CP22022E (cit. on p. 81).

Morito, S., Tanaka, H., Konishi, R., Furuhara, T., and Maki, T. (2003). 'The morphology and crystallography of lath martensite in Fe-C alloys'. In: *Acta Materialia* 51.6, pp. 1789–1799. ISSN: 1359-6454. DOI: 10.1016/S1359-6454(02)00577-3 (cit. on p. 49).

Moulinec, H. and Suquet, P. (1994). 'A fast numerical method for computing the linear and nonlinear properties of composites'. In: *Comptes rendus de l'Académie des sciences. Série II, Mécanique, physique, chimie, astronomie* 318, pp. 1417–1423. ISSN: 1251-8069 (cit. on pp. 1, 16, 17).

Moulinec, H. and Suquet, P. (1998). 'A numerical method for computing the overall response of nonlinear composites with complex microstructure'. In: *Computer Methods in Applied Mechanics and Engineering* 157.1-2, pp. 69–94. ISSN: 0045-7825. DOI: 10.1016/S0045-7825(97)00218-1 (cit. on pp. 1, 16, 24).

Moulinec, H. and Silva, F. (2014). 'Comparison of three accelerated FFT-based schemes for computing the mechanical response of composite materials'. In: *International Journal for Numerical Methods in Engineering* 97.13, pp. 960–985. ISSN: 0029-5981. DOI: 10.1002/nme.4614 (cit. on p. 21).

Mura, T. (1987). *Micromechanics of Defects in Solids*. 2nd. Dordrecht: Martinus Nijhoff Publishers. ISBN: 90-247-3256-5 (cit. on p. 18).

Murray, B. J. (2008). 'Enhanced formation of cubic ice in aqueous organic acid droplets'. In: *Environmental Research Letters* 3.2, p. 025008. ISSN: 1748-9326. DOI: 10.1088/1748-9326/3/2/025008 (cit. on p. 81).

Murray, B. J. and Bertram, A. K. (2006). 'Formation and stability of cubic ice in water droplets'. In: *Physical Chemistry Chemical Physics* 8.1, pp. 186–192. ISSN: 1463-9076. DOI: 10.1039/b513480c (cit. on p. 81).

NASA Space Science News (1999). *Space Daily*. URL: http://www.spacedaily.com/news/life-99c.html (visited on 02/03/2015) (cit. on p. 82).

Oosterlee, C. W. and Washio, T. (2000). 'Krylov Subspace Acceleration of Nonlinear Multigrid with Application to Recirculating Flows'. In: *SIAM Journal on Scientific Computing* 21.5, pp. 1670–1690. ISSN: 1095-7197. DOI: 10.1137/S1064827598338093 (cit. on pp. 23, 24).

Parameswaran, V. R. (1987). 'Orientation dependence of elastic constants for ice'. In: *Defence Science Journal* 37.3, pp. 367–375. ISSN: 0011-748X. URL: http://publications.drdo.gov.in/ojs/index.php/dsj/article/view/5924 (cit. on p. 82).

Peranio, N., Roters, F., and Raabe, D. (2012). 'Microstructure Evolution during Recrystallization in Dual-Phase Steels'. In: *Materials Science Forum* 715-716, pp. 13–22. ISSN: 1662-9752. DOI: 10.4028/www.scientific.net/MSF.715-716.13 (cit. on p. 47).

PETSc Team (2015). *PETSc*. URL: http://www.mcs.anl.gov/petsc (visited on 02/03/2015) (cit. on p. 23).

Raabe, D., Sachtleber, M., Zhao, Z., Roters, F., and Zaefferer, S. (2001). 'Micromechanical and macromechanical effects in grain scale polycrystal plasticity experimentation and simulation'. In: *Acta Materialia* 49.17, pp. 3433–3441. ISSN: 1359-6454. DOI: 10.1016/S1359-6454(01)00242-7 (cit. on pp. 37, 54, 57).

Ramazani, A., Ebrahimi, Z., and Prahl, U. (2014). 'Study the effect of martensite banding on the failure initiation in dual-phase steel'. In: *Computational Materials Science* 87, pp. 241–247. ISSN: 0927-0256. DOI: 10.1016/j.commatsci.2014.01.051 (cit. on pp. 39, 67).

Reina, C. and Conti, S. (2014). 'Kinematic description of crystal plasticity in the finite kinematic framework: A micromechanical understanding of F=FeFp'. In: *Journal of the Mechanics and Physics of Solids* 67, pp. 40–61. ISSN: 0022-5096. DOI: 10.1016/j.jmps.2014.01.014 (cit. on p. 12).

Reuber, C., Eisenlohr, P., Roters, F., and Raabe, D. (2014). 'Dislocation density distribution around an indent in single-crystalline nickel: Comparing nonlocal crystal plasticity finite element predictions with experiments'. In: *Acta Materialia* 71, pp. 333–348. ISSN: 1359-6454. DOI: 10.1016/j.actamat.2014.03.012 (cit. on pp. 12, 37).

Rezvanian, O., Zikry, M. A., and Rajendran, A. M. (2006). 'Microstructural modeling of grain subdivision and large strain inhomogeneous deformation modes in f.c.c. crystalline materials'. In: *Mechanics of Materials* 38.12, pp. 1159–1169. ISSN: 0167-6636. DOI: 10.1016/j.mechmat.2005.12.006 (cit. on p. 80).

Roters, F. (2011). 'Advanced Material Models for the Crystal Plasticity Finite Element Method – Development of a general CPFEM framework'. English. Habilitation Thesis. Aachen: RWTH Aachen. URL: http://darwin.bth.rwth-aachen.de/opus3/volltexte/2011/3874/ (cit. on p. 3).

Roters, F., Eisenlohr, P., Bieler, T. R., and Raabe, D. (2010a). *Crystal Plasticity Finite Element Methods in Materials Science and Engineering*. Weinheim: Wiley-VCH. ISBN: 978-3527324477 (cit. on pp. 1, 12, 93, 101).

Roters, F., Eisenlohr, P., Hantcherli, L., Tjahjanto, D. D., Bieler, T. R., and Raabe, D. (2010b). 'Overview of constitutive laws, kinematics, homogenization, and multiscale methods in crystal plasticity finite element modeling: Theory, experiments, applications'. In: *Acta Materialia* 58, pp. 1152–1211. ISSN: 3094–3106. DOI: 10.1016/j.actamat.2009.10.058 (cit. on p. 1).

Roters, F., Eisenlohr, P., Kords, C., Tjahjanto, D. D., Diehl, M., and Raabe, D. (2012). 'DAMASK: the Düsseldorf Advanced MAterial Simulation Kit for studying crystal plasticity using an FE based or a spectral numerical solver'. In: *Procedia IUTAM: IUTAM Symposium on Linking Scales in Computation: From Microstructure to Macroscale Properties*. Ed. by O. Cazacu. Vol. 3. Amsterdam: Elsevier, pp. 3–10. DOI: 10.1016/j.piutam.2012.03.001 (cit. on pp. 3, 45).

Roters, F., Diehl, M., Eisenlohr, P., and Raabe, D. (2013). 'Microstructural Design of Advanced Engineering Materials'. In: ed. by D. A. Molodov. 1st ed. Wiley-VCH. Chap. Crystal Plasticity Modeling, pp. 41–67. ISBN: 978-3-527-33269-4. DOI: 10.1002/9783527652815.ch03 (cit. on p. 1).

Schey, Harry Moritz (1973). *Div, Grad, Curl, and all that*. New York: W W Norton & Company. ISBN: 0-393-09367-0 (cit. on p. 5).

Scott, J., Miles, M., Fullwood, D., Adams, B., Khosravani, A., and Mishra, R. K. (2013). 'Room Temperature Shear Band Development in Highly Twinned Wrought Magnesium AZ31B Sheet'. In: *Metallurgical and Materials Transactions A* 44.1, pp. 512–516. ISSN: 1073-5623. DOI: 10.1007/s11661-012-1405-0 (cit. on p. 54).

Sedláček, R. (2009). 'Finite Elemente in der Werkstoffmechanik'. Habilitation Thesis. München. ISBN: 978-3-86853-027-8 (cit. on p. 13).

Shanthraj, P., Eisenlohr, P., Diehl, M., and Roters, F. (2015). 'Numerically robust spectral methods for crystal plasticity simulations of heterogeneous materials'. In: *International Journal of Plasticity* 66, pp. 31–45. ISSN: 0749-6419. DOI: 10.1016/j.ijplas.2014.02.006 (cit. on pp. 16, 17, 19, 23, 35, 101).

Sluys, L. J. and Estrin, Y. (2000). 'The analysis of shear banding with a dislocation based gradient plasticity model'. In: *International Journal of Solids and Structures* 37.46-47, pp. 7127–7142. ISSN: 0022-5096. DOI: 10.1016/S0020-7683(99)00331-5 (cit. on p. 80).

Steinmetz, D. R., Jäpel, T., Wietbrock, B., Eisenlohr, P., Gutierrez-Urrutia, I., Saeed-Akbari, A., Hickel, T., Roters, F., and Raabe, D. (2013). 'Revealing the strain-hardening behavior of twinning-induced plasticity steels: Theory, simulations, experiments'. In: *Acta Materialia* 61.2, pp. 494–510. ISSN: 3094–3106. DOI: 10.1016/j.actamat.2012.09.064 (cit. on p. 12).

Suquet, P., Moulinec, H., Castelnau, O., Montagnat, M., Lahellec, N., Grennerat, F., Duval, P., and Brenner, R. (2012). 'Multi-scale modeling of the mechanical behavior of polycrystalline ice under transient creep'. In: *Procedia IUTAM: IUTAM Symposium on Linking Scales in Computation: From Microstructure to Macroscale*

Properties 3. Ed. by O. Cazacu, pp. 64–78. ISSN: 2210-9838. DOI: 10.1016/j.piutam.2012.03.006 (cit. on p. 16).

Tasan, C. C., Hoefnagels, J. P. M., and Geers, M. G. D. (2010). 'Microstructural banding effects clarified through micrographic digital image correlation'. In: *Scripta Materialia* 62.11, pp. 835–838. ISSN: 1359-6462. DOI: 10.1016/j.scriptamat.2010.02.014 (cit. on p. 52).

Tasan, C. C., Diehl, M., Yan, D., Zambaldi, C., Shanthraj, P., Roters, F., and Raabe, D. (2014a). 'Integrated experimental-numerical analysis of stress and strain partitioning in multi-phase alloys'. In: *Acta Materialia* 81, pp. 386–400. ISSN: 3094–3106. DOI: doi:10.1016/j.actamat.2014.07.071 (cit. on pp. 39, 50–52, 67, 101).

Tasan, C. C., Hoefnagels, J. P. M., Diehl, M., Yan, D., Roters, F., and Raabe, D. (2014b). 'Strain localization and damage in dual phase steels investigated by coupled in-situ deformation experiments-crystal plasticity simulations'. In: *International Journal of Plasticity* 63, pp. 198–210. ISSN: 0749-6419. DOI: 10.1016/j.ijplas.2014.06.004 (cit. on pp. 39, 43, 48).

Tasan, C. C., Diehl, M., Yan, D., Bechtold, M., Roters, F., Schemmann, L., Zheng, C., Peranio, N., Ponge, D., et al. (2015). 'Advances in understanding process-microstructure-property relationships and micro-mechanically-guided design of dual-phase steels'. In: *Annual Review of Materials Research* 45.1. ISSN: 1531-7331 (cit. on pp. 1, 38, 41).

Thurmer, K. and Nie, S. (2013). 'Formation of hexagonal and cubic ice during low-temperature growth'. In: *Proceedings of the National Academy of Sciences* 110.29, pp. 11757–11762. ISSN: 0027-8424. DOI: 10.1073/pnas.1303001110 (cit. on p. 81).

Tjahjanto, D. D., Turteltaub, S., and Suiker, A. S. J. (2008). 'Crystallographically based model for transformation-induced plasticity in multiphase carbon steels'. In: *Continuum Mechanics and Thermodynamics* 19.7, pp. 399–422. ISSN: 0935-1175. DOI: 10.1007/s00161-007-0061-x (cit. on p. 45).

Tromans, D. (2011). 'Elastic anisotropy of hcp metal crystals and polycrystals'. In: *International Journal of Research and Reviews in Applied Sciences* 6.4, pp. 462–483. ISSN: 2076-734X. URL: http://www.arpapress.com/volumes/vol6issue4/ijrras_6_4_14.pdf (cit. on pp. 56, 57).

Volokh, K. Y. (2007). 'Lagrangian Equilibrium Equations in Cylindrical and Spherical Coordinates'. In: *Computers, Materials, & Continua* 5.1, pp. 37–42. ISSN: 1546-2218. DOI: 10.3970/cmc.2007.003.037 (cit. on p. 10).

Wang, F., Sandlöbes, S., Diehl, M., Sharma, L., Roters, F., and Raabe, D. (2014). 'In situ observation of collective grain-scale mechanics in Mg and Mg–rare earth alloys'. In: *Acta Materialia* 80, pp. 77–93. ISSN: 1359-6454. DOI: 10.1016/j.actamat.2014.07.048 (cit. on pp. 54, 55, 58–61, 101).

Xu, T. and Li, M. (2009). 'Topological and statistical properties of a constrained Voronoi tessellation'. In: *Philosophical Magazine* 89.4, pp. 349–374. DOI: 10.1080/14786430802647065 (cit. on pp. 62, 64).

Yan, D., Tasan, C. C., and Raabe, D. (2015). 'High resolution in-situ mapping of microstrain and microstructure evolution reveals damage resistance criteria in dual

phase steels'. In: *Acta Materialia* 96, pp. 399–409. DOI: 10.1016/j.actamat.2015.05.038 (cit. on p. 41).

Yang, Y., Wang, L., Zambaldi, C., Eisenlohr, P., Barabash, R., Liu, W., Stoudt, M. R., Crimp, M. A., and Bieler, T. R. (2011). 'Characterization and modeling of heterogeneous deformation in commercial purity titanium'. In: *JOM* 63.9, pp. 66–73. ISSN: 1047-4838. DOI: 10.1007/s11837-011-0161-8 (cit. on p. 43).

Yoo, M. H. (1981). 'Slip, twinning, and fracture in hexagonal close-packed metals'. In: *Metallurgical Transactions A* 12A, pp. 409–415. ISSN: 0360-2133. DOI: 10.1007/BF02648537 (cit. on p. 54).

Zambaldi, C. and Raabe, D. (2010). 'Plastic anisotropy of γ-TiAl revealed by axisymmetric indentation'. In: *Acta Materialia* 58.9, pp. 3516–3530. ISSN: 1359-6454. DOI: 10.1016/j.actamat.2010.02.025 (cit. on p. 43).

Zambaldi, C., Yang, Y., Bieler, T. R., and Raabe, D. (2012). 'Orientation informed nanoindentation of α-titanium: Indentation pileup in hexagonal metals deforming by prismatic slip'. In: *Journal of Materials Research* 27.1, pp. 356–367. ISSN: 0884-2914. DOI: 10.1557/jmr.2011.334 (cit. on pp. 43, 44).

Zeghadi, A., N'guyen, F., Forest, S., Gourgues, A-F, and Bouaziz, O. (2007a). 'Ensemble averaging stress–strain fields in polycrystalline aggregates with a constrained surface microstructure – Part 1: anisotropic elastic behaviour'. In: *Philosophical Magazine* 87.8-9, pp. 1401–1424. DOI: 10.1080/14786430601009509 (cit. on pp. 68, 78, 79).

Zeghadi, A., Forest, S., Gourgues, A-F, and Bouaziz, O. (2007b). 'Ensemble averaging stress–strain fields in polycrystalline aggregates with a constrained surface microstructure – Part 2: crystal plasticity'. In: *Philosophical Magazine* 87.8-9, pp. 1425–1446. DOI: 10.1080/14786430601009517 (cit. on pp. 68, 72, 78, 79).

Zeman, J., Vondřejc, J., Novák, J., and Marek, I. (2010). 'Accelerating a FFT-based solver for numerical homogenization of periodic media by conjugate gradients'. In: *Journal of Computational Physics* 229.21, pp. 8065–8071. ISSN: 0021-9991. DOI: 10.1016/j.jcp.2010.07.010 (cit. on p. 16).

Zhao, Z., Ramesh, M., Raabe, D., Cuitiño, A. M., and Radovitzky, R. (2008). 'Investigation of three-dimensional aspects of grain-scale plastic surface deformation of an aluminum oligocrystal'. In: *International Journal of Plasticity* 24, pp. 2278–2297. ISSN: 0749-6419. DOI: 10.1016/j.ijplas.2008.01.002 (cit. on p. 54).

Acronyms

AFM atomic force microscopy

Ar Argon

BC boundary condition

bcc body-centered cubic

BSE backscatter electron

BVP boundary value problem

CP crystal plasticity

CRSS critical resolved shear stress

DAMASK Düsseldorf advanced material simulation kit

DFT discrete Fourier transform

DIC digital image correlation

DP dual phase

EBSD electronic backscatter diffraction

ECCI electron channelling contrast imaging

fcc face-centered cubic

FEM finite element method

FFT fast Fourier transform

FFTW fastest Fourier transform in the west

FIB focused ion beam

GMRES generalised minimal residual method

GND geometrically necessary dislocation

hcp hexagonal close-packed

hex hexagonal

IPF inverse pole figure

IQ image quality

M2i Materials Innovation Institute

Mg Magnesium

MPIE Max-Planck-Institut für Eisenforschung GmbH

PDE partial differential equation

PETSc portable, extensible toolkit for scientific computation

RMS root mean square

ROI region of interest

RVE representative volume element

SE secondary electron

SEM scanning electron microscopy

VE volume element

Nomenclature

Latin Letters

Symbol	*Description*	*Unit*
a	fitting parameter	
$\boldsymbol{A}$	acoustic tensor	
$\mathcal{B}$	body	
$\boldsymbol{b}$	BURGER's vector	m
$\boldsymbol{B}$	left CAUCHY–GREEN deformation tensor	-
$\boldsymbol{C}$	right CAUCHY–GREEN deformation tensor	-
$\mathbb{C}$	stiffness tensor	Pa
$\mathbb{D}$	reference stiffness tensor	Pa
E	YOUNG's modulus	Pa
$\boldsymbol{E}_0$	GREEN–LAGRANGE strain tensor	-
$\boldsymbol{E}_\mathrm{t}$	EULER–ALMANSI strain tensor	-
$\mathcal{F}$	FOURIER transform	
$\mathscr{F}$	non-linear operator	
$\boldsymbol{F}$	deformation gradient	-
$\mathcal{H}$	HEAVISIDE function	
$\boldsymbol{H}_0$	displacement gradient	-
$\boldsymbol{H}_\mathrm{t}$	inverse displacement gradient	-
i	imaginary unit	
$\boldsymbol{I}$	identity, unit matrix	
J	JACOBIAN determinant of the deformation gradient	-
J_2	2^{nd} invariant of the deviatoric part of the CAUCHY stress	Pa^2
k	angular frequency	1/s
$\mathcal{L}$	LAGRANGE funtional	
l	side length	m
$\boldsymbol{L}$	velocity gradient	m/s
M	TAYLOR factor	
$\boldsymbol{n}$	normal vector	
N	number of sampling points	
n	rate sensitivity parameter	
$\mathscr{P}$	preconditioning operation	
$\boldsymbol{P}$	1^{st} PIOLA–KIRCHHOFF stress tensor	Pa
$\boldsymbol{R}$	rotation tensor	-
$\boldsymbol{t}$	traction	N

$\mathbb{S}$	compliance tensor	Pa^{-1}
$\boldsymbol{S}$	2nd Piola–Kirchhoff stress tensor	Pa
$\boldsymbol{s}$	line direction	m
$\boldsymbol{u}$	displacement	m
$\boldsymbol{U}$	right stretch tensor	-
$\boldsymbol{V}$	left stretch tensor	-
$\boldsymbol{v}$	material velocity	m/s
$\boldsymbol{x}$	coordinates in reference configuration	m
$\boldsymbol{y}$	coordinates in current configuration	m

Greek Letters

Symbol	*Description*	*Unit*
α	weight for equilibrium	-
δ	unit impulse function	
β	weight for compatibility	-
Δ	deviation	
$\boldsymbol{\varepsilon}$	Cauchy strain tensor	-
γ	shear strain	-
$\mathbb{\Gamma}$	Γ-operator for Green's function	
κ	frequency	Hz
λ	stretch ratio	-
$\boldsymbol{\Lambda}$	Lagrange multiplier	
$\boldsymbol{\xi}$	microstructural state	
$\boldsymbol{\sigma}$	Cauchy stress tensor, infinitesimal stress tensor	Pa
$\boldsymbol{\tau}$	polarisation field	Pa
τ	shear stress	Pa
$\boldsymbol{\omega}$	rotation	-
$\boldsymbol{\chi}$	deformation map	

Superscripts

Symbol	*Description*
$'$	deviatoric part of a tensor
$\cdot$	derivative with respect to time
$\sim$	fluctuating part of a quantity
$-$	average quantity, negative quantity for Miller indices
k	index
m	index

Subscripts

Symbol	*Description*

0	quantity in reference configuration/initial value
e	elastic part
p	plastic part
ref	reference value
t	quantity in current configuration
vM	VON MISES equivalent of a tensorial quantity

Index

List of Figures

List of Tables